OPTICAL TRANSFECTION AND INJECTION TECHNIQUES APPLIED TO MAMMALIAN AND EMBRYONIC CELLS

Maria Leilani Torres

A Thesis Submitted for the Degree of PhD
at the
University of St. Andrews

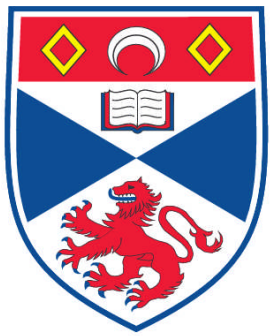

2011

University of St. Andrews

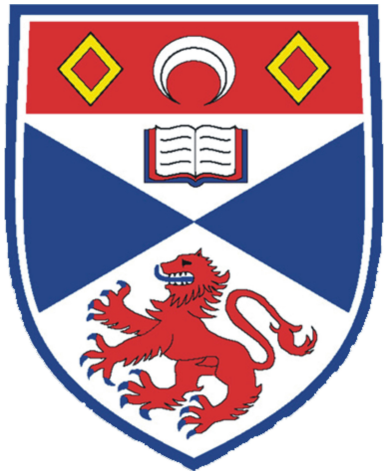

Optical Transfection and Injection Techniques Applied to Mammalian and Embryonic cells

Maria Leilani Torres

A thesis submitted to the University of St. Andrews in application for the degree of Doctor of Philosophy

August 2011

Declaration

I, Maria Leilani Torres, hereby certify that this thesis, which is approximately 45,000 words in length, has been written by me, that it is the record of work carried out by me and that it has not been submitted in any previous application for a higher degree. I was admitted as a research student in April 2007 and as a candidate for the degree of Doctor of Philosophy in October 2007; the higher study for which this is a record was carried out in the University of St Andrews between 2007 and 2011.

Signature of Candidate: ..... Date: .....

I hereby certify that the candidate has fulfilled the conditions of the Resolution and Regulations appropriate for the degree of Doctor of Philosophy in the University of St Andrews and that the candidate is qualified to submit this thesis in application for that degree.

Signature of Supervisor: ..... Date: .....

Signature of Supervisor: ..... Date: .....

In submitting this thesis to the University of St Andrews we understand that we are giving permission for it to be made available for use in accordance with the regulations of the University Library for the time being in force, subject to any copyright vested in the work not being affected thereby. I also understand that the title and abstract will be published, and that a copy of the work may be made and supplied to any bona fide library or research worker, that my thesis will be electronically accessible for personal or research use unless exempt by award of an embargo as requested below, and that the library has the right to migrate my thesis into new electronic forms as required to ensure continued access to the thesis. We have obtained any third-party copyright permissions that may be required in order to allow such access and migration, or have requested the appropriate embargo below. The following is an agreed request by candidate and supervisor regarding the electronic publication of this thesis: Access to Printed copy and electronic publication of thesis through the University of St Andrews.

Signature of Candidate: ..... Signature of Supervisor: .....

Signature of Supervisor: ..... Date: .....

Abstract

The delivery of biomolecules into living cells is an important methodology in cell and molecular biology. Optical methods using lasers are attractive tools for such application. However, the interaction of the laser with the cell depends on the laser type and the parameters used. Hence, in this thesis, optical transfection and injection of both mammalian and embryonic cells is demonstrated using a variety of laser sources. Furthermore, some key issues are addressed by demonstrating alternative configurations of optoinjection and transfection systems to develop a robust, user-friendly device with potential for commercialisation.

Most optical methods for the delivery of molecules rely on complex and expensive laser systems that occupy a large footprint. In order for the system to be accessible to end-users, transient transfection of plasmid DNA into mammalian cells using an inexpensive continuous wave 405 nm diode laser is demonstrated. In this work, the laser parameters are varied in order to optimise the transfection efficiency. By calculating the temperature change upon irradiation of the focused violet light, the mechanism of violet diode laser transfection is elucidated. Furthermore, the system is used to deliver small interfering RNA molecules to specifically knock down a particular protein within the cell. This work is a major step towards an inexpensive and portable optical transfection system.

The critical issue of accurate targeting of the cell membrane is also addressed in conventional near-infrared femtosecond optical transfection systems. A near-infrared femtosecond holographic system is built utilising a spatial light modulator in order to provide fast three dimensional beam translation. Computer control of dosage and targeting allows us to explore the potential of different targeting modalities. An enhanced optoinjection and transfection on mammalian cells is demonstrated. Furthermore, the system is applied to optically manipulate a developing *Pomatoceros lamarckii* embryo. The holographic system can be employed to optoinject a variety of macromolecules into the embryo, as well as orient and position the embryo by switching to the continuous wave mode of the laser. Such development of optical techniques to deliver biomolecules and orient embryos will benefit the field of developmental biology.

Lastly, to achieve controlled cavitation, limiting the mechanical effects of a nanosecond laser source, an optically trapped microsphere undergoes laser induced breakdown in the presence of a cell monolayer. Laser induced breakdown of a trapped microsphere allows control over several parameters, such as the microsphere material, position of the breakdown from the monolayer and the size of the microsphere. Optimising these parameters provide limited mechanical effects, particularly suited for cell transfection. This technique is an excellent tool for plasmid-DNA trans-

fection of multiples of cells with both reduced energy requirements and cell lysis compared to previously reported approaches.

Demonstrating optimised and successful delivery of macromolecules with the variety of laser sources used in this thesis will advance the applicability of optical injection and transfection and allow more potential users to access the technique. This thesis advances optical injection and transfection for optimised delivery of macromolecules to both mammalian cells and a developing embryo.

Contents

Abbreviations

bp	base pair
CALI	chromophore assisted light inactivation
CCD	charge coupled device
C. elegans	Caenorhabditis elegans
CHO-K1	chinese hamster ovary
CW	continuous wave
Da	Dalton
DNA	Deoxyribonucleic acid
E.coli	Escherichia coli
Elk 1	E-26-like protein
EMCCD	Electron multiplying charge coupled device
FITC	fluorescein isothiocyanate
fs	femtosecond
GFP	green fluorescent protein
HEK293	human embryonic kidney cells
iRNA	interfering RNA
LASIK	laser-assisted in situ keratomileusis
LC	liquid crystal
LIB	laser induced breakdown

LISW	laser induced stress wave
Mito-DsRed	mitochondrial targeted Discosoma sp. red fluorescent protein
mRNA	messenger RNA
MW	molecular weight
NA	numerical aperture
ND:YAG	neodymium-doped yttrium aluminium garnet ($Nd:Y_3Al_5O_{12}$)
NIR	near infrared
ns	nanosecond
P. lamarckii	Pomatoceros lamarckii
PAL	parallel aligned
PtK2	rat kangaroo kidney epithelial cells
ROS	reactive oxygen species
siRNA	small interfering RNA
SLM	spatial light modulator
Ti:sapphire	titanium sapphire ($Ti:Al_2O_3$)
TK	Herpes simplex thymidine kinase
TRex-willin-GFP-HEK	tetracycline inducible willin-GFP protein expressing HEK293 cell line
TRITC	tetramethylrhodamine isothiocyanate
USM	ultrasound contrast microagents
US	ultrasound
UV	ultraviolet light
VIS	visible

Symbols

α	absorption coefficient
α_p	polarisability of the sphere
$\mathbf{Ca}^{2+}$	Calcium ion
$\mathbf{c}$	speed of light
Δ	band gap energy
$\tilde{\Delta}$	ionisation potential
$\Delta\mathbf{T}_p$	change in temperature
$\mathbf{D}$	distance of particle from substrate
$\mathbf{D}_f$	diffusion coefficient
$\mathbf{E}$	energy
$\mathbf{E}_B$	energy of bubble
$\mathbf{e}$	electron charge
ϵ_o	vacuum dielectric permitivitty
η_v	viscosity of the medium
$\mathbf{f}$	focal length
γ	stand-off distance
$\mathbf{H_2O_2}$	Hydrogen peroxide
$\mathbf{I}$	intensity
$\mathbf{j}$	heat flow

$\mathbf{k}_B$	Boltzmann constant
κ	Thermal diffusion time
$\mathbf{k}_o$	thermal conductivity
$\lambda/\mathbf{2}$	half-wave plate
λ	wavelength
$\mathbf{m}_c$ **and** $\mathbf{m}_v$	mass of free electrons where subscript c and v represent electrons in conduction band and valence band respectively
$\mathbf{m}$	ratio of index of refraction of medium and particle ($\mathrm{n}_m/\mathrm{n}_p$)
$\mathbf{n}$	index of refraction where subscript m and p represent medium and particle respectively
$\mathbf{N}_{crit}$	critical density
$\mathbf{N}$	number of base pairs
ν	frequency
$\mathbf{O_2}^-$	Oxygen ion
$\mathbf{OH}^-$	hydroxide ion
$\mathbf{P}$	laser power
$\mathbf{P}_\infty$	static pressure of liquid
$\mathbf{P}_v$	vapour pressure
$\mathbf{T}$	laser exposure time
$\mathbf{T}_p$	temperature
$\mathbf{T}_c$	bubble collapse time
$\mathbf{R}_B$	maximum bubble radius
$\mathbf{R}_G$	radius of gyration
ρ	density of liquid

$\mathbf{p}$	momentum of light
σ_k	multiphoton absorption coefficient with k number of photons absorbed
σ	scattering cross-section of sphere
ζ,η	transverse coordinates
$\boldsymbol{x,y,z}$	spatial coordinates

1 Introduction

"... the one thing that I think is extremely important, is that anyone can do it, if given a chance, if given the opportunity."—Mario Capecchi, interview with the Nobel prize committee

1.1 Laser applications in the biomedical field

Light allows one to see and understand the physical world. With light, things of varying sizes and distances can be appreciated, from a tiny living creature to the very far stars in the galaxy. With the invention of light microscopes, the field of biology and medicine progressed very rapidly. Robert Hooke first reported his illustrations of diverse biological objects in his book, *Micrografia*, using a compound microscope. He was followed by Anton Van Leuwenhoek, who built a simple inverted microscope and examined a variety of substances including muscles, insects and detailed structures of plants. During the first part of the 19th century, major advancements in microscopy occured which involved the development of high numerical aperture (NA) objectives. Ernst Abbe and Carl Zeiss contributed immensely improving the theory of lens design. Armed with innovations in optics and well crafted lenses, light has become a powerful tool which allows us to see from the astronomical to the microscopic. With a powerful laser source, one can alter the biological, chemical and mechanistic processes of transparent and non-transparent materials.

The use of lasers as surgical instruments with microscopes gave birth to the progessive field termed as **laser scissors** or **laser nanosurgery**. Laser nanosurgery is defined as the use of lasers to microscopically alter subcellular, cellular or tissue samples by ablation. Although nowadays the process of microscopic dissection is attributed to lasers, the idea of laser nanosurgery started almost 50 years before the invention of the laser. Russian born Sergej Tschachotin first built an ultraviolet (UV) light microscope, which used a magnesium spark to generate a wavelength (λ) of 280 nm focused by a quartz objective [1]. A standard microscope objective was used to view the sample from above and the UV beam was utilised as a probe to study the functions of a variety of subcellular organelles from the eggs of sea urchins, protozoans, paramecium and euglena.

The advent of the ruby laser in 1960 paved the way for applications of lasers in studying both mammalian and plant cells. Amy *et al.* observed changes on a single cell's mitochondria using a focused pulsed ruby laser [2]. Ruby lasers were replaced by the more versatile argon-ion lasers, which have several laser lines spanning the blue spectral region. Due to the high absorbance of cellular and tissue substances at these wavelengths, argon-ion lasers were adopted as the workhorse for cellular microdissections. Michael Berns spear-headed a series of successful nanosurgery experiments using an argon-ion laser demonstrating selective DNA deletion on homologous chromosomes in living cells [3].

In laser nanosurgery, the laser is incident to a powerful objective (high NA) that allows light to be focused very tightly. In this configuration, light can have enough intensity to ablate microscopic materials with a precision of less than a micron. This is an exciting prospect in cell biology since the functionalities of a particular cellular organelle can be investigated in a specific event in a cell's life while retaining its normal mechanistic processes. Such a powerful technique has led to the understanding of specific aspects of fundamental cell biology. For example, by laser ablation of the centrosome, the microtubule organising centre in a mammalian cell, it was found that a neuronal axon extension is independent of the presence of the centrosome nucleation [4]. On the other hand, following the ablation of the centrosome *via* laser nanosurgery, a cell loses its ability to maintain its polarisation during cell migration [5].

Hence, the field of cell biology has benefited from the employment of lasers. Single mammalian cells can now be probed, analysed, dissected, sorted and manipulated using laser light. Cells can be optically trapped and passively sorted using laser light with sculptured wavefronts [6]. Calcium waves within a cell can be generated in a controlled fashion using a femtosecond (fs) laser by inducing the production of reactive oxygen species (ROS) [7]. Fast cell lysis for immediate analysis of intracel-

lular contents has also been demonstrated [8]. Imaging has been revolutionised with the development of laser-based microscopy systems such as confocal, multiphoton and single-molecule fluorescence, allowing long-term imaging of *in vitro* and *in vivo* samples but as well as resolving structures beyond the diffraction limit [9].

With the development of a variety of laser sources, laser light is utilised to explore other possible therapeutic treatments for certain medical conditions. Lasers have been extensively employed in applications such as laser-assisted in situ keratomileusis (LASIK), a procedure wherein, a flap on top of the cornea is created and the stroma tissue is remodeled by vaporising tissue material using a laser [10]. With the topical application or injection of a photosensitiser, laser light can effectively target and destroy cancer cells with minimal effects on the surrounding tissues [11]. Kidney stones can be ablated and fragmented using focused laser light in a procedure called laser lithotripsy [12]. Furthermore, dental carries can be removed using laser sources [13]. From these examples, it is clear that lasers have had a huge impact on both basic and applied biological research.

The applications of lasers in the biomedical field continue to grow. Collaborations in laser engineering, physics, biology and medicine must be fostered in order to push advances in laser application. Currently, the challenge in laser engineering remains to be producing reliable, portable, yet inexpensive laser systems. Biologists and medical practitioners must be open to testing new laser devices and seeking out solutions using advanced technologies for their investigations. Physicists are encouraged to understand the phenomenon occurring and determine optimised parameters for each application. This interdisciplinary approach will lead to more breakthroughs in the biomedical field and so bring about useful technologies to aid the diagnosis and treatment of diseases.

1.2 Optical delivery methods for cell transfection

In contrast to previously mentioned laser nanosurgery applications which lead to cutting and ablation of cells or subcellular organelles, this thesis utilises laser nanosurgery to introduce a transient wound in the plasma membrane for the introduction of foreign membrane impermeable macromolecules into living cells. The technique has been described in many names, however, I will specify two nomenclatures for laser-mediated delivery technique based on the type of molecules delivered. The following terms will be used extensively throughout this thesis,

- **Optical injection (Optoinjection)** - an overall general term describing the introduction macromolecules such as fluorescently labelled dextrans and dyes

into cells and an embryo using a tightly focused laser beam [14, 15]. The delivery is mediated by the formation of short-lived transient pore, with lifetime in the order of ms, and confirmed visually by the presence of residual bubbles on the membrane. Individual cells or each subcellular component of the cell has to be individually targeted.

- **Optical transfection** - describes a technique particular for the purpose of delivery of genetic materials such as DNA, messenger RNA (mRNA) and small interfering RNA (siRNA) into cells [16]. It has a configuration similar to optoinjection and the two terms are sometimes use interchangeably. But in this thesis, the results on transfection of cells will be described strictly using this term. Also popularly known as phototransfection [17, 18], the technique has been used for genetic modification of cells and protein expression in specific subcellular location within a cell.

Transfection is the general term referring to the procedure of delivering genetic material into living cells. Mainly, it is employed as a means to transform a cell by manipulating its genetic properties. In order to provide a direct read-out, a protein encoding for the gene of interest can be tagged with a fluorescent protein (e.g. green fluorescent protein (GFP)). Genetic modification *via* transfection is a ubiquitous and indispensible technology with applications stemming from basic science research to applied and industrial developments. To name a few such applications, recombinant DNA, mRNA or interference RNA (iRNA) technologies can greatly advance agricultural biotechnology, biopharmaceuticals, genetic therapy and cell biology [16].

Several methodologies have been developed in order to perform transfection. Cationic mediated transfection is a procedure that encloses a genetic material in hydrophobic liposome to ease the passage of the genetic material into the cell membrane. Viral methods using adenovirus, retrovirus and lentivirus have been used to enclosed the genetic material to infect the cell. Electrical pulses have been also utilised to introduce small **electropores** on the plasma membrane. Another technique called **sonoporation** employs ultrasound in order to induce cavitation for membrane permeabilisation. These procedures are non-selective and affect all cells in an *in vitro* sample. However, these technologies are not applicable for single cell manipulation, wherein a single cell within a population is transfected. In order to perform single cell manipulation, microinjection has previously been employed, which requires a mechanical probe such as a capillary glass tube in order to pierce through the cell membane and inject minuscule amounts of genetic material into the cellular cytosol. However, this technique is invasive and laborious, leading to inconsistencies in success rates and viable injection.

Armed with the concept that a laser can perform nanosurgery on a cell and ablate its subcellular components, the concept of optoinjection for the purposes of transfection has evolved. Although currently still in its infancy as a robust method of transfection, the first published work on optical transfection was reported more than 25 years ago. In 1984, Tsukakoshi *et al.*, demonstrated DNA transfection using an UV light from an Nd:YAG laser on normal rat kidney cells [19]. Similarly, Tao *et al*, reportedly used the same laser to successfully transfected human fibrosarcoma cells [20]. They reported that the method can be performed faster and can achieve ten-fold higher efficiency than microinjection [19].

But what are the advantages of this optical delivery technique over other methodologies of transfection? The key advantage of using optical transfection is its flexibility, allowing single cell or multi-cell manipulation. Also, as lasers require no physical contact with cells, the technique is aseptic, reducing the possibility of contamination in an *in vitro* sample. Optical transfection is relatively easy to use, since an end-user with a working knowledge of microscopy can perform the experiment in an existing system. Furthermore, the technology is flexible and can be used in conjunction with other lab-on-a-chip platforms, such as microfluidic chips [15] for non-adherent transfection or adherent patterned culture. By toggling between continuous wave (CW) and a mode-locked fs pulsed mode, a single cell can be optically trapped and transfected, allowing a pure optical methodology for single cell manipulation [21].

In recent years, various laser based systems have been used for optical transfection. Wavelengths in the UV [19, 20], visible (VIS) [22, 23, 24] and near-infrared (NIR) [25, 26, 17, 27, 18] in both pulsed (nanosecond (ns) or femtosecond (fs)) and CW mode, have all been used for cell transfection. Pulsed laser systems seemed to be the obvious choice for both optoinjection and optical transfection as these systems can achieve high peak power at a very short duration, minimising the energy deposited to the sample. To date, fs optical transfection has emerged as the most consistent method, but this system requires the use of expensive lasers with a typically large footprint (e.g. the Ti:sapphire fs laser oscillator). On the other hand, pulsed ns systems were demonstrated to target multiple cells *via* a mechanism called laser induced breakdown (LIB) to create shock waves and cavitation bubbles [28, 29, 30]. In terms of CW lasers in the visible light region, the first laser used for cell transfection was the 488 nm output line of an argon-ion laser, which again has a large footprint [23]. However, in 2005, Paterson *et al.* used a low-cost CW violet diode laser for cell transfection, which was the simplest and most inexpensive method of laser-mediated transfection to date [31].

In order to push the technology towards wider usage and commercialisation, there is a need to optimise the delivery efficiency by optoinjection and the transfection

efficiency of each laser system. It is important to note that the mechanism for poration is dependent upon the type of laser used and its pulse duration [16]. Hence, the mechanism of laser-cell interaction for each laser system needs to be understood and the parameters and conditions require systematic investigation in order for the technique to be optimised. Also, optical injection and transfection can be further applied to many biological problems by coupling it to other modalities of imaging, such as fluorescence and time-lapse imaging. Thus, these techniques should be developed in tandem with other existing imaging approaches.

1.3 Objectives of this thesis

This thesis involves interdisciplinary work with several aspects focusing on cell biology, optics and physics. It aims to build up methodologies and optimise the techniques of optoinjection and transfection using a variety of laser devices in different pulsed regimes from a CW and pulsed laser sources (ns and fs). Although, these laser systems have been demonstrated for delivery of biomolecules into cells, each laser device has a specific disadvantage that limits the number of viably treated cells. Specifically, several key issues will be addressed in this thesis such as, the novelty of performing transient transfection using a violet diode laser, precise targeting enhancement with NIR fs lasers and controlled cavitation and limited lysis zone using ns laser devices. This work improves the current methodologies in optical transfection by testing alternative configurations of the laser devices and developing the technology in order to achieve a user-friendly optical transfection system with potential for commercialisation.

The first part of this thesis details the foundations of the concept of cellular permeabilisation using lasers. Chapter 2 discusses the different biological barriers that prevent successful transfection. Two types of transfection are distinguished - stable and transient transfection. Furthermore, the different methodologies of transfection are discussed. Finally, the concepts of cell resealing and wound healing are explained based on studies in mammalian cells and sea urchin oocytes. Chapter 3 presents a discussion on the probable mechanism of optical nanosurgery and poration. The two mechanism between CW laser nanosurgery *via* heating and a photochemical effect and pulsed laser mechanisms such as multiphoton ionisation and electron avalanche or cascade process will be discussed. This chapter sets the basic foundations for experimental results presented in Chapters 4–7.

The second part of this thesis presents the experimental aspects of the work. The thesis presents three different techniques for optical transfection. Chapter 4 demonstrates the use of a 405 nm CW laser for optical transfection. In this chapter, a

protocol is developed to allow transient expression of a plasmid expressing the Mito-DsRed protein in both Chinese hamster ovary (CHO-K1) cells and human embryonic kidney (HEK293) cells. The system and the parameters used for the experiments are reported. A discussion is also dedicated on the viability study performed using a trypan blue dye-exclusion assay as a function of power and exposure time of the laser on the cells. Furthermore, to elucidate the mechanism of the procedure, calculations on the temperature increase during optical transfection using a violet diode laser is presented.

Chapter 5 and 6 detail the experimental device built in order to demonstrate enhanced optoinjection and transfection of mammalian and embryonic cells using a fs NIR laser. In Chapter 5, a fs holographic system is described employing a fs laser in tandem with a spatial light modulator (SLM). It has an incorporated fluorescence module that enables targeted two-step selective optical transfection. Different modalities of targeting are reported by changing the computer generated hologram encoded in the SLM. With a piezo-driven mirror, the field of view is enlarged for wider field of view cell targeting. The system is assembled with the aim towards a more consistent, robust and user-friendly "point and shoot" device for optical transfection. In Chapter 6, the system is utilised for optoinjection of variety of biomolecules in a newly emerging evolutionary model, *Pomatoceros lamarckii*. The chapter details the experimental parameters employed to successfully optoinject individual blastomeres of the embryo at various stages in its development. In addition, the same system is employed for optical manipulation of single-celled embryos. The work presents a step towards an all-optical approach for the manipulation of living and developing embryos.

Meanwhile, in Chapter 7, a new methodology to control the mechanical side effects of LIB is presented in a pulsed ns laser mediated permeabilisation. By optically tweezing a polymer microsphere, the energy deposited to the sample is much lower compared to inducing LIB in water or on glass coverslips as previously described [32, 30, 28]. This controls the mechanical effects due to LIB, such as shockwave and cavitation bubble expansion and collapse, thereby limiting the affected region to 3–6 cells. The events during LIB of a single trapped microsphere are discussed in detail. This work is a step towards a more controlled LIB with regional cell selectivity using ns laser devices.

Finally, Chapter 8 summarises the results obtained in the experimental chapters. The merits of the work are discussed and its contribution to the ongoing research in this field is highlighted. Specifically, the chapter highlights some of the key future work in optical transfection and the next steps required to translate the technology to biologists and medics as potential end-users.

2

Crossing the membrane barrier - mechanical techniques for cell transfection

In this chapter, a description is given on the different mechanical techniques for cell transfection. Aside from the membrane barrier, the intracellular obstacles for protein expression to occur is described. Furthermore, an explanation of the two different types of transfection assay is provided.

2.1 Introduction

Therapeutic approaches in medical treatment are leading towards the use of molecular biology to create or modify genetic makeup in order to cure disease. However, the plasma membrane, which is considered a protective barrier, hinders the spontaneous transport of large molecules into the cell cytoplasm. This thin phospholipid bilayer is semiporous in nature allowing only the transport of small hydrophobic molecules (non polar) (e.g. oxygen, carbon dioxide and hydrocarbons) without the aid of membrane proteins and permits only certain exchanges of materials with the extracellular environment [33]. Transport proteins embedded in the lipid bilayer permits specific molecules or ions only to translocate through the membrane. Hence,

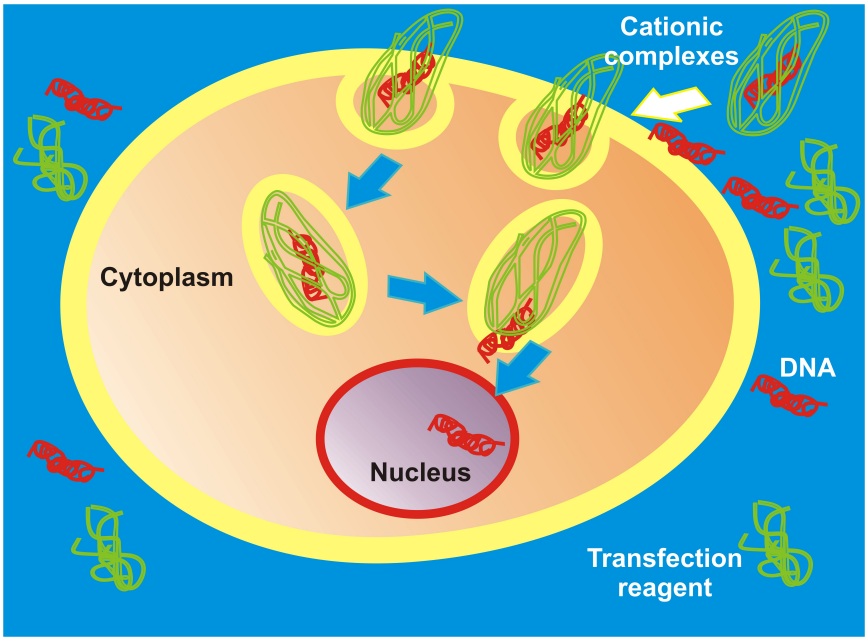

Figure 2.1: A schematic illustration of the mechanism of DNA chemical transfection in eukaryotic cells. See text for details.

it becomes challenging to deliver effectively therapeutic agents inside the cell. Up until now, there remains a need to develop a safe, consistent and reliable technology to bypass the membrane barrier of the cell.

Since the plasma membrane is made up of a hydrophobic phospholipid bilayer, several approaches have been developed in order to deliver the genetic material *via* a carrier vehicle. A carrier vehicle can be in the form of a lipid or a virus. Chemical means of transfection is performed by mixing plasmid DNA with polycations or cationic lipids. A schematic illustration of the mechanism of chemical transfection is shown in Fig. 2.1. In commercially available chemical transfection systems, DNA is enclosed in cationic lipids, forming a lipid-DNA complex which fuses into the membrane and intaken by the cells *via* endocytosis [34]. However, the efficiency of transfection and viability of transfected cells remains relatively low especially for primary cells and expression levels of protein vary with cell type. Viral means of transfection using a retrovirus or adenovirus have been a method of choice for many researchers due to their high transfection efficiencies and expression levels. However, this technique has an inherent toxicity and high probability of host immunotoxicity, making it difficult to translate this technology into humans. An additional drawback of both chemical and viral technique is that they have little or no specificity, treating all cells in a sample globally.

Mechanical methods are a promising avenue towards the introduction of naked genetic material into a living cell. At therapeutic dosages, they can have low toxicity, and are generally non-immunogenic and non-pathogenic. These methods are based on the concepts of wounding and resealing. The cell membrane can be wounded, leading to "pore formation" that allows passive uptake of exogenous materials into the intracellular environment. Due to the fluidity of the membrane and other biochemical processes which will be discussed later on, the cell has the ability to reseal itself and maintain its membrane retain its integrity. The means to generate this pore include applying electrical pulses, ultrasonic waves in conjunction with bubbles, particle bombardment using gene gun, direct injection using capillary needles and laser-mediated cell permeabilisation.

2.2 Mechanical methods in cell transfection

In this section, I will discuss several mechanical methods in which a physical perturbation to the membrane of a cell is performed to achieve cell transfection. Over the years, different mechanical methods have been investigated to provide a means of transiently permeabilising the cell membrane and allowing therapeutic agents to be taken up by the cells. The following subsections describe such techniques.

2.2.1 Microinjection

The first physical method employed to inject a material into a cell is akin to using a needle to inject or remove blood in a person. A fine glass capillary needle with the genetic material, controlled with a micromanipulator, is inserted into a cell. After puncture, the membrane rapidly creates a seal enclosing the capillary needle, preventing loss of intracellular material. Picolitre amounts of concentrated material (50–100 ng/μL) are delivered inside the cell or animal by hydrostatic pressure, after which the needle is pulled out and the cell or embryo carries on its normal physiological processes. The schematic diagram of the procedure is shown in Fig. 2.2(A). Mario Capecchi first demonstrated microinjection by injecting the Herpes simplex virus thymidine kinase (TK) gene into cultured mammalian cells with very high efficiency [36]. Injection directly into the nucleus, increases the transfection efficiency of the technique as it bypasses the endonucleases present in the cytoplasm [37]. In 1980, Gordon *et al.* demonstrated genetic transformation of mouse embryo [38], which led on to the production of the first transgenic mouse [39]. Since then, the technique has been employed to deliver a variety of DNA constructs into single cells and embryos. It has been extensively employed for iRNA technologies in *C.*

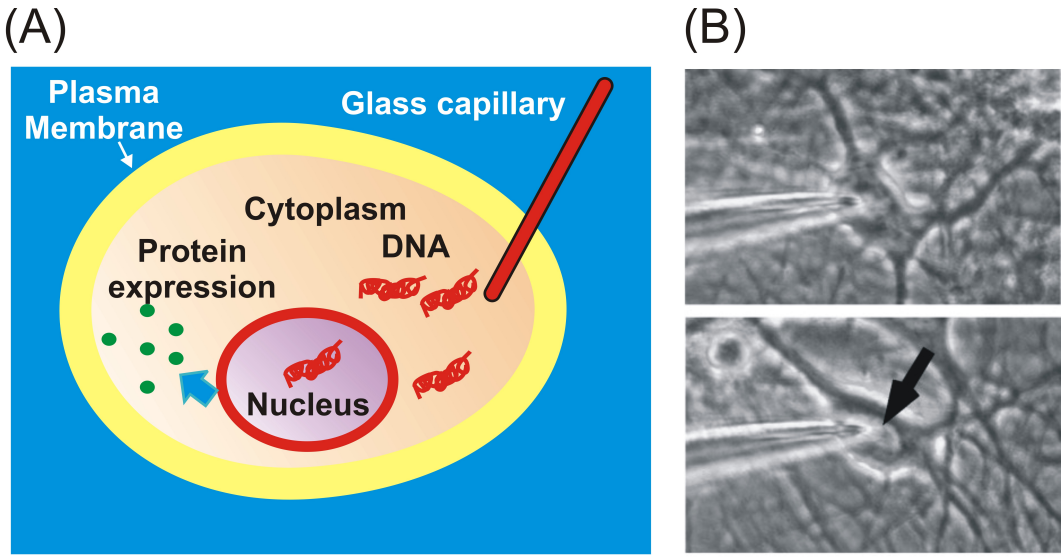

Figure 2.2: (A) Schematic diagram of DNA transfection by microinjection. A needle made up of glass capillary filled with the material to be injected is pushed through the plasma membrane of the cell. Picolitre volumes of solution are injected into the cytoplasm by applying pressure. (B) Top image shows a cultured primary hippocampal neurons under phase contrast showing the tip of the needle above the cell layer. At the bottom image, the tip of the needle slightly touches the cell surface.- *Reprinted from Journal of Neuroscience Methods with permission from Elsevier* [35].

elegans, delivery of dyes (dextrans) for the purposes of cell lineage mapping and gap junctional communication studies.

Although microinjection is the simplest technique to inject biomolecules into living cells or embryos, it is considered to be the most difficult to implement. The technique requires months of training and experience to perform a successful injection. This makes the efficiency of the technique variable from one researcher to another. Several approaches had been performed in order to automatise the procedure. For example, automated [40] and robotic systems [41] or microelectromechanical based devices [42] have been implemented to provide high throughput microinjection. However, the technique is still an invasive procedure as the injection of capillary needles is a direct physical insult to a cell, which may lead to loss of cell viability. The success of injection largely depends as well on the size and the properties of the sample. In addition, with small embryos, the injection procedure may lead to bursting and loss of fluid material after injection.

2.2.2 Biolistic particle delivery system

Biolistic particle delivery is a technique in which high-speed small tungsten microparticles, called microprojectiles, coated with biomolecules penetrate through cell walls and membranes [43]. Propelling these microprojectiles is performed using a device called a **gene gun**, whereby high pressure helium is used to accelerate the microprojectiles to a high speed. It was first developed to perform plant cell transformation by coating the microprojectiles with a plasmid encoding for the gene of interest to allow transient expression of the gene. The microprojectiles were used to bombard sections of intact *A. cepa* epidermal tissue [43]. Although this technique has been used for both plant and animal tissue, the penetration of larger size microparticles may exhibit adverse effects. Recently, Lian *et al.*, developed a technique in which biomolecules of interest are bombarded into the samples without conjugating them to a microparticle [44]. They demonstrated delivery of macromolecules of varying sizes such as Hoechst with molecular weight (MW): 623.96, Lucifer yellow (MW: 491.57), dextrans (MW: 70 kDa and 500 kDa) into CHO-K1 cells. Successful DNA transfection of CHO with the GFP-tubulin encoding gene and proteins was achieved but efficiency was found to be a function of the size of the molecule and its concentration. The achievable DNA transfection efficiency ranged from 9% to 70%.

Meanwhile, the group of Groisman developed a smaller biolistic delivery device using a pneumatic capillary gun [45]. Compared to the commercially available gene gun called *helios* (BioRad), the device provides a larger penetration depth and can selectively target smaller sample areas. Using this device, localised delivery of iRNA was performed on live embryos of the leech, *Hirudo medicinalis* [46]. Also, specific

iRNA-mediated silencing of the expression of axon guidance factor, netrin, was achieved in leech in a localised manner. Furthermore, they demonstrated delivery of two or more biomolecules to specific tissue regions, allowing multiple expression of different genes.

2.2.3 Electroporation

Electroporation is a technique that uses an externally applied electric field in order to increase significantly the permeability, conductivity and in some cases mechanical rupture of the negatively charged plasma membrane. Hydrophilic molecules, which are normally membrane impermeant, gain access to the cytosol. Neumann *et al.*, first demonstrated using intense electric pulses (8 KV/cm, 5 μs) to create stable transformant mouse cell lines expressing TK gene. They proposed that a structural change on the lipid bilayer occurred which allowed the opening of a pore providing a means for DNA to enter into the cell [47]. Subsequently, several reports have shown reliable transformation of plant cells such as maize [48], carrot protoplasts and tobacco [49], showing the ability of the technique to permeabilize the hard cell wall of plant cells. Electroporation has been applied to a wide variety of biological samples such as postmitotic neuronal cells [50], gametes of zebrafish, channel catfish and common carp [51], as well as mouse [52] and chick embryos [53]. *In vivo* targeting of mouse tibialis interior muscles using electroporation was also demonstrated [54].

Electroporation instruments are commercially available. Its common configuration includes a cuvette with aluminum electrodes on either side which contains the sample suspension. Electrodes are attached to the holder and connected to a pulse generator to control the amplitude voltage and its pulse characteristics. This technology has several strong features, such as high expression of fluorescent reporter genes and its ability to transfect multiple cells at a time. All cells in the sample are treated with the electric field. This multiple-cell transfection procedure is particularly useful for large scale genomic screenings.

Currently, there is rapidly developing research on designing single cell electroporation. Single cell electroporation in a micropipette tip has been demonstrated on a single rat hippocampal neurons [55]. Recently, a novel injection based device for electroporation for animal tissue has been developed [56]. Due to the nature of electroporation, wherein, only the regions of the cell facing the electrodes experiences transmembrane potential beyond a threshold value, the efficiency of the technique can be limited. Hence, in order to enhance the efficiency without the need to increase the voltage amplitude, a spiral type microfluidic channel, taking advantage of the hydrodynamic focusing allows the cells to swirl around the channel in between the cathode and anode electrodes [57].

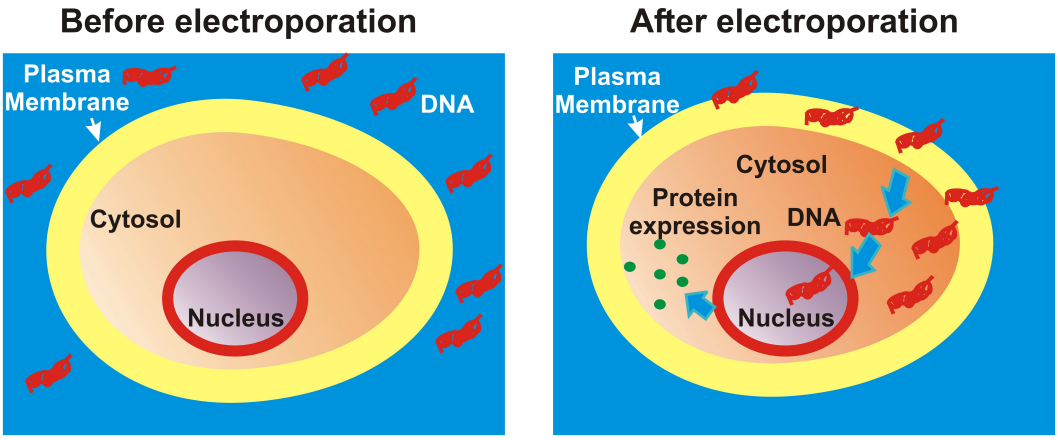

Figure 2.3: Schematic diagram of mechanics of electroporation transfection. Plasmid DNA is normally impermeable to the plasma membrane of the cell. After application of the electric field, a binding event occurs wherein the plasmid DNA binds to the surface of the plasma membrane [60]. After several minutes, the DNA translocates to the cytoplasm and to the nucleus.

The resulting transport of the plasmid DNA across the membrane is primarily attributed to the formation of electropores, which allow the plasmid to tunnel across the membrane [47, 58]. Volcano crater like structures on the membrane surface of red blood cells with pore diameters ranging from 20–120 nm were observed post electroporation by rapid freezing followed by electron microscopy [59]. The mechanism of electroporation has been a subject of many studies but recent experiments have confirmed that a binding step occurs at the cell membrane surface [60] as illustrated in Fig. 2.3. Golzio *et al.* confirmed by single-molecule fluorescence studies that DNA plasmids tagged with nucleic acid fluorescent stain, TOTO, bind to the surface of the cell membrane observed 10 min post electroporation. After 30 min, some of the fluorescence still remains in the membrane but are mostly expressed in the cytoplasm.

There are various parameters that play a role in viable electroporation and successful transfection of cells. The voltage amplitude, which controls the strength of the field and the duration of applied electric field to the cells are the main parameters controlling the efficiency of uptake of molecules. Different combinations of electric field amplitude and duration of exposure have been implemented inorder to optimise the parameters for transfection by electroporation. Direct current of high electric fields in the order of KV/cm with short μs exposure has been implemented [47]. Similarly, low AC voltages with peak to peak amplitude of 50–200 V/cm, frequency range of 0.1 Hz–1 MHz and longer duration of exposure (1–100 s) in different wave-

forms (square wave, triangle wave and sine wave) has also been shown to successfully transfect *E. coli* [61]. It has been proposed that at lower amplitudes and longer exposure, the dielectric breakdown of the membrane is not achieved and the cells recover quicker after treatment leading to higher rates of survival.

In transfection, several biological factors are key aspects to consider in achieving high transfection rates. The concentration of plasmid DNA in the solution and the cell type greatly affects the transfection efficiency. Particularly, primary cells are known to be sensitive to any physical disturbance and may yield low transfection rates. Optimal electric field strength and pulse durations may also vary as a function of the biomolecule size to be delivered. In addition, only the side of the cells facing the cathodes binds to the plasmid DNA leading to transfection [60]. It was hypothesised that the electrophoretic force, propels the DNA plasmid towards the membrane leading to enhanced transport of the DNA plasmid across the cellular membrane [62, 63]. Hence, the geometry of the system and the orientation of cells with respect to the electrode is an important parameter in optimising transfection for each cell type.

2.2.4 Sonoporation

Sound waves at certain frequencies beyond human hearing can be used to permeabilise cells. Sonoporation is such a technique and employs MHz frequency ultrasound (US) to enhance or permit the uptake of macromolecules into cells. Loading of macromolecules such as dextrans [37] and DNA [64] had been demonstrated using this technique. During US propagation, the main biological effects are heating and cavitation. Heating is important to consider, particularly at MHz frequency, as the rapid heating of cells and tissues can cause cell lysis. *In vivo* studies show that sonoporation operated beyond clinical parameters can cause capillary rupture and hemorrhaging [65].

Initial studies on sonoporation used pure US for cell permeabilisation [64]. More recently, its efficiency for gene delivery was observed to be enhanced by the presence of ultrasound contrast microagents (USCM), gas-filled microbubbles that oscillate with the exposure of ultrasound [66]. Delivery of biomolecules to cells using USCM can be achieved by the destruction of microbubbles, which leads to the release of its contents to surrounding cells or *via* cavitation effects leading to pore formation and the uptake of exogenous materials. The latter is more relevant to DNA transfection for *in vitro* applications, wherein cells are incubated with USCM and the DNA is present in the surrounding medium. Above a certain threshold frequency, the application of US can cause microbubble disruption. The sudden and violent collapse of microbubbles can also produce cavitation effects such as high-velocity fluid

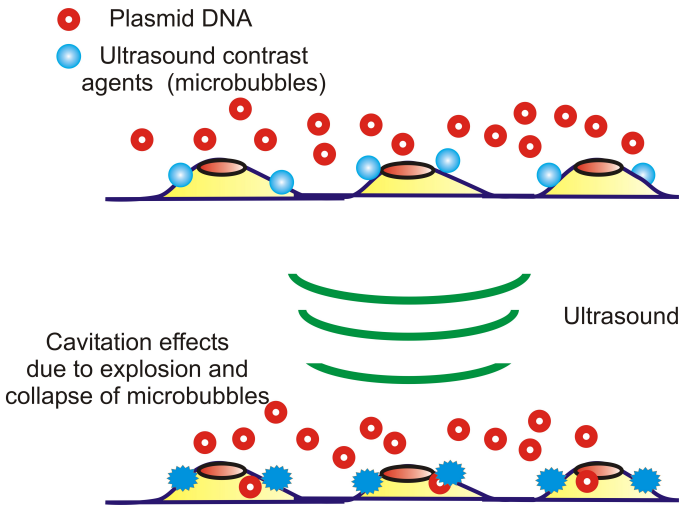

Figure 2.4: Schematic diagram of sonoporation with USCM (microbubbles). During the application of ultrasound at certain amplitude and frequency, the microbubbles are destroyed leading to cavitation effects that induces pore formation on cells and allow intake of plasmid DNA.

microjets that may produce pores on the cell membrane [67, 68]. An illustration of this phenomenon is shown in Fig. 2.4. Electron microscopy images show that the exposure of microbubbles to US leading to their destruction causes transient membrane pores on surrounding cells [69], which may facilitate the uptake of DNA. Furthermore, secondary effects such as shear stress [70] or shockwaves [71] may also play a role in membrane permeabilisation by US.

DNA delivery by sonoporation has been an active research area due to its compatibility with animal and human gene therapies. Ultrasound machines are readily available in hospitals and clinics. Furthermore, the technique has been extensively applied to *in vivo* applications. For example, Shimamura *et al.* demonstated a 10-fold increase in luciferase expression with microbubble enhanced-US on male Wistar rats central nervous system [72]. Microbubbles with naked plasmid DNA were injected into the rat's cisterna magna and bioluminescence was detected in its cerebellum and brainstem. Application of US to microbubble injected rats showed an increase in luciferase activity compared to rats without US but injected with microbubbles and also with US but in the absence of microbubbles. Meanwhile, Taniyama *et al.* performed sonoporation on cultured human vascular smooth muscle cells, endothelial cells and the rat artery [73]. Sonoporation with microbubbles was performed on a rat carotid artery with wild-type p53 encoding plasmid, an oncogene, without any apparent inflammation and toxicity on the blood vessels. In this

work, they showed that using mechanical methods for transfection, such as sonoporation, could provide an alternative safe clinical gene therapy without requiring a potentially toxic viral vector system.

2.3 Membrane repair

Generally, the mechanical techniques presented in this chapter involve a physical disruption in the cell membrane in the form of structural defects on the membrane where exogenous biomolecules can be injected, endocytosed by the cell or diffused through. However, without the capacity of the cell membrane to reseal or heal itself, it would lead to loss of intracellular material and cell death. Hence, membrane resealing is an important issue in transfection methodologies to allow cells to survive after the physical injury.

In nature, it is a common event that the plasma membrane is disrupted and then rapidly reseals in order to maintain cellular or a tissue's physiological state. The capacity to reseal has been demonstrated particularly in sea urchin eggs, wherein a physical wound can be healed and restored within 5 s, maintaining the eggs viability. The egg can then be further fertilised and developed into an embryo [74, 75]. The rapid resealing process has been found to limit the influx of potential toxins. Heilbrunn presented a model of cell repair for wounds of less than a micron in size in which the presence of extracellular Ca^{2+} is necessary in order to allow membrane resealing and prevent loss of cytosolic material [76]. Furthermore, Steinhardt *et al.* showed that extracellular Ca^{2+} is necessary to induce a lysosome mediated dependent exocytotic response [77].

Exocytotic delivery of cytosolic material is necessary in pore healing [74]. At local disruption sites, exocytosis is stimulated and its amount is correlated to the wound size [78, 79]. The hypothesis is that the rapid flow of extracellular Ca^{2+} into the disrupted site causes vesicle-plasma membrane fusion events *via* exocytosis of intracellular lysosome particles. For small disruption sites, exocytosis enables lipid flow over the wounded region lessening the tension due to the damage in the surface of the plasma membrane [80, 81]. Meanwhile, for larger disruptions, resealing can occur by vesicle-vesicle and vesicle-plasma membrane fusion events, more commonly known as the patch hypothesis [74, 75]. By these fusion events, the wound gets patched by intracellular material.

In the context of gene delivery and cell transfection, there must be a balance with the influx of material and the time scale of membrane resealing. The amount of material entering into the cytoplasm should be enough for successful transfection but the outflow of the intracellular material should be low in order to maintain cell

viability. Interestingly, the extracellular concentration of Ca^{2+} seems to be a key component in membrane resealing. This is particularly important in mechanical methods for transfection such as electroporation, sonoporation and optical transfection, wherein the cells are bathed in a buffer medium containing the genetic material. Ca^{2+} in the buffer medium should be at a concentation that it allows membrane resealing. For example, in sonoporation of *Xenopus* oocytes, complete resealing occurs at concentrations above 0.54 mM. Furthermore, the rate of resealing was found to be a function of extracellular Ca^{2+} concentration. A lower concentration of Ca^{2+} has a slower rate of resealing and vice versa [82]. However, at present, there are no systematic studies correlating extracellular Ca^{2+} with transfection efficiency.

2.4 Other biological barriers: cytosol and the nuclear envelope

Using the discussed mechanical methods for cell transfection allows direct delivery of genetic material into the cell's cytoplasm. After bypassing the membrane barrier, there are still several biological barriers that genetic material (*i.e.* plasmid DNA, mRNA or siRNA) has to overcome. Enclosed within the membrane is the cytoplasm which is made up of compartmentalised organelles separated from other cellular components. Also, within the cytoplasm is the cytosol, which is the space filled with cytoskeletal filaments such as actin, microtubules and intermediate filaments as well as nutrients and other molecules essential for cell survival. Although, the cytosol is mainly comprised of water, which makes up more than half the cellular volume, it is considered more like a gel made up of a fiber network [83]. This complex array of macromolecules and cytoskeletal filaments may impose restrictions on the diffusion of extracellular molecules such as dextrans or plasmid DNA into the cytoplasm. Previously, it was found that macromolecule solutes of < 500 kDa can rapidly diffuse into the cytoplasm, but mobility is greatly impeded for larger molecules [83]. Similarly, due to molecular crowding and binding of nucleic acids to cytoplasmic proteins, the mobility of DNA in the cytoplasm drastically decreases with increasing DNA size > 100 base pairs (bp) [84]. Slower diffusion of DNA fragments was observed in the cytoplasm compared to their diffusion in water [84, 85]. Furthermore, after microinjection of plasmid DNA in the cytoplasm, cytosolic nucleases can cause rapid degradation of plasmid DNA [86]. Hence, naked plasmid DNA is more metabolically unstable in the cytosol as compared to lipid enclosed DNA endocytosed during chemical transfection [86].

However, the cytosol is not the last barrier to effective gene expression by injection of plasmid DNA. Plasmid DNA needs to travel to the nucleus and bypass the

nuclear envelope. It was observed that up to only 0.1% of cytosolic injected DNA could be transcribed [36]. In an attempt to enhance translocation of the plasmid DNA through the nuclear envelope, nuclear localisation peptides have been created in order to efficiently transport the plasmid DNA into the nucleus [87]. The nuclear envelope is clearly a factor in successful gene expression as the expression levels of transfected cells were found to be dependent on the cell cycle phase and particularly the mitotic activity of the cell [88]. For example, dividing cells can be transfected at higher rates compared to quiescent or postmitotic cells which suggests that plasmid DNA enters the nucleus upon disassembly of the nuclear envelope during mitotic cell division [88, 89]. Furthermore, initially synchronised cells in mitotic and synthesis phase resulted in enhanced transfection rates compared to cells that were unsynchronised [18].

2.5 Stable vs. transient transfection

There are two approaches to perform transfection analysis: stable and transient transfection. Stable transfection refers to the generation of a cell population that has integrated the transfected gene into the host DNA and allowed the expression of the protein several generations after cell division. A schematic diagram of creating stable cell lines is shown in Fig. 2.5. In order to perform this procedure, cells that have integrated the DNA into its host genome are isolated by the addition of a selective marker. Current plasmids have an incorporated gene for resistance to certain antibitotics. With this resistance, cells that have integrated the plasmid DNA into their genome survive in the presence of the antibiotic, allowing individual cell with antibiotic resistance and hence the gene of interest to multiply and create stable colonies. Stable transfection is a useful approach as cells with a gene of interest can be repeatedly used for several experiments. However, it is a time consuming process which may take weeks to create a pure stable cell line expressing the protein.

Transient transfection relies on the introduction of DNA and its immediate protein expression within 24–72 hours. The advantage of this approach is that it is a relatively fast assay to check for protein activity in transfected cells. However, its disadvantages are its inconsistency in the levels of protein expression and the transfection efficiency, which is affected by cell culture preparation. However, in contrast to stable transfection, wherein, the cells are required to be cultured for several weeks, transient transfection does not require this lengthy procedure. Hence, the technique is particularly useful for cells that cannot last in culture for long periods of time, such as post-mitotic or primary cell lines.

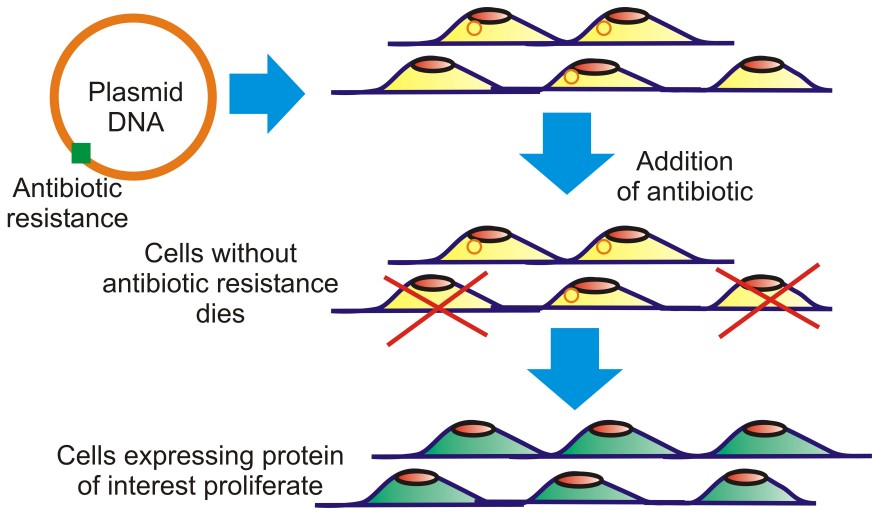

Figure 2.5: Schematic diagram of stable DNA transfection. Plasmid DNA is a circular double stranded DNA which incorporates an antibiotic resistance gene in addition to the gene of interest. After transfection of the plasmid DNA into cells, an antibiotic (selection pressure) is added to the transfected cells. Cells that have been successfully transfected and expressed the gene of interest also have the antibiotic resistance. Hence, cells which have not been transfected will die and only cells transfected will proliferate, creating stable colonies. With continuous cell culture with the selection pressure, the culture will only be comprised of cells with the gene of interest.

2.6 Conclusion

In this chapter, the different methods of mechanical means for transfection were discussed. Each method has its own merits and disadvantages. The mechanical techniques for cell transfection such as microinjection, biolistics, electroporation and sonoporation were discussed in detail. Furthermore, we detailed how the membrane reseals after injury and the other biological barriers that may impede translocation of plasmid DNA into the nucleus. Finally, the two types of transfection, stable and transient, were differentiated.

Aside from the plasma membrane, DNA plasmid still has to bypass the endonucleases in the cytoplasm and the nuclear envelope before finally reaching the nucleus. For iRNA and mRNA wherein its translation occurs in the cytoplasm, the restrictions in successful expression maybe solely due to the degradation of these materials by the endonucleases. In general, macromolecular solutes such as dextrans up to a certain size are generally mobile within the cytoplasm. In contrast, rapid degradation of microinjected DNA in the cytoplasm has been observed [86]. Compared to dextran molecules, the mobility of DNA fragments drastically decreases at sizes around 250 bp and only a small amount of genetic materials reach the nucleus [84]. This is an interesting aspect as this implies that there is a biochemical limit in the achievable transfection efficiency of these mechanical methods. It also shows the differing mechanism between transporting macromolecules such as dextrans or dyes as opposed to transfection with plasmid DNA. In addition, successful delivery into the cytoplasm does not necessarily imply successful transfection leading to expression of protein of interest.

Developing mechanical techniques for cell transfection are important as they do not require any viral vector system that may impose toxic effects on the host cells. Microinjection, which is the simplest technique to date, requires skills and manual dexterity in order to inject successfully genetic material without compromising cellular viability. Compared to other techniques such as electroporation and sonoporation, only a small number of cells (≈ 100) can be injected at a time, which limits its application for large *in vitro* assays. Hence, developing automated microinjection for rapid implementation of delivery of biomolecules is still in progress.

The biolistic method that evolved from utilising tungsten particles to bombardment of the aerosolised genetic particles were both found to be an effective means to deliver genetic materials into mammalian cells. Both application of electric fields for electroporation and ultrasound for sonoporation are capable of membrane permeabilisation. Although, electroporation is being re-engineered to generate electropores to single mammalian cells among the techniques discussed in this chapter, at present, only microinjection is being routinely utilised for single cell or embryo in-

jection of genetic material. Notably, sonoporation and biolistic delivery systems do not have the cell selectivity which is important for single-cell genetic manipulation studies or injecting genetic material into a specific blastomere of a developing embryo. As such, there is still a niche for developing mechanical methods for effective transfection allowing single-cell manipulation.

Having discussed the variety of mechanical techniques available for transfection, the probable mechanisms of membrane wounding using lasers will be discussed in the following chapter. The mechanism of pore formation in optical injection and transfection rely on the mode of laser operation as well as the parameters (*i.e.* power and exposure time) employed for an application. Furthermore, I will discuss the current state of the art in this field, using laser sources such as CW, NIR fs and ns laser systems and how the technique has been applied to target both single and multiple cells as well as a living embryo.

3

Optical transfection and injection - review and mechanism

The mechanism of pore formation in optical injection and transfection is dependent on the type of laser and parameters employed. In this chapter, the different mechanisms of laser nanosurgery in cells and tissues will be explained. A review of the current state-of-the-art laser-based cell transfection techniques will be discussed, providing an overview of the differences between laser sources used for optical injection and transfection.

3.1 Mechanisms of laser nanosurgery in cells and tissues

The interaction of a laser light with a biological material is a complex phenomenon often leading to chain of events that may induce physical, thermal, chemical and mechanical effects [90]. When a laser is incident to a biological sample, it can be absorbed, reflected, refracted, transmitted or scattered depending on the properties of the material. The parameters controlled by laser irradiation are equally important and determine the type of interaction occurring during the irradiation. The dependence of laser-induced processes on the laser wavelength, spot size, pulse duration, exposure time and repetition rate are important parameters to understand as

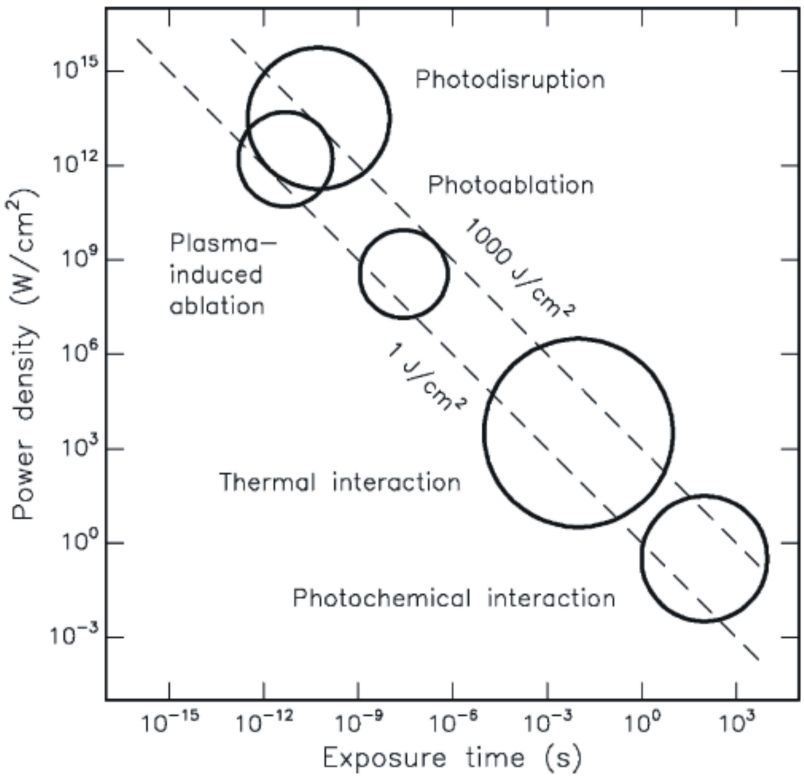

Figure 3.1: An illustration of laser-tissue interactions against power density and exposure time. The circles provide the approximate range of laser irradiation parameters at which each process occur.- *With kind permission from Springer Science+Business Media* [91].

these control the effects on the biological sample. A summary of the laser-induced processes occurring with cells and tissues is shown in Fig. 3.1. A log-log plot is shown of power density and exposure time, with dashed lines corresponding to 1 and 10^3 J/cm^2. From this chart, several processes are shown to result from the interaction of lasers with cells and tissues. These processes include photochemical, photothermal, photoablation, plasma-induced ablation and photodisruption.

3.1.1 Linear laser-tissue interaction

For long irradiation exposure, ranging from seconds to minutes, and relatively low power density, ≈ 1 W/cm^2, the interaction between laser and the biological material is mainly attributed to photochemical effect. A photochemical mechanism occurs when light incident to a macromolecule within the cell or tissue is irradiated leading to an excited state reaction. In biophotonics, this interaction is mainly used in pho-

todynamic therapy, wherein photosensitisers which specifically absorb at a certain wavelength are excited by light and release highly reactive free radicals. Tissue oxygen interacts with the free radicals, leading to cell death [92]. Similarly, a technique called chromophore assisted light inactivation (CALI) inactivates a specific protein by introducing a dye within a cell, conjugated to an antibody against the protein of interest. In CALI, a short-pulsed laser is irradiated in a specific area within the cell leading to generation of reactive oxygen species (ROS), which inactivate the specific proteins. Due to the short-lived nature of ROS, the damage is localised to the adjacent protein of the irradiated chromophore [93, 94].

A significant increase in temperature leads to thermal effects. Thermal effects in tissues are characterised either as coagulation, vaporisation, carbonisation or melting, depending on the tissue structure, peak temperature and the length of exposure of the laser [91, 90]. Cell hyperthermia was found to occur for temperatures exceeding 44 ^{o}C [95]. Importantly, for single cell studies, membrane phase transitions were found at temperatures between 42–45 ^{o}C, leading to changes in membrane permeability [96]. Interestingly, within the range of 42–45 ^{o}C, the percentage of surviving and recovering cells depends on the length of exposure in that temperature [95]. Beyond 50 ^{o}C, enzymatic activities decrease, leading to further reduction in the proportion of surviving cells. Irreversible necrosis occurs at 60 ^{o}C for several seconds. Vaporisation of water occurs at 100 ^{o}C, forming microbubbles and mechanical ruptures on cells and tissues. In CW laser based optical transfection, thermal effect is conjectured to be the primary mechanism for membrane permeability, leading to uptake of molecules [23, 22]. However, there is limited study of the actual cellular perturbation necessary to achieve successful transfection.

3.1.2 Nonlinear laser-tissue interaction

Photoablation is the removal or etching of tissue material. Often pulsed UV lasers are used to perform photoablation. A single UV photon is enough to reach the molecule's excited state and exceed its bond energy [91]. A certain threshold intensity must be achieved in order to perform ablation. The process involves absorption of photons, leading to excitation to a repulsive state wherein the kinetic energy gain is sufficient to dissociate molecules. Photoablated tissues are ejected or vaporised from the irradiated site leaving a clean etched surface with minimal cell necrosis and minimum collateral damage wherein the etch depth is proportional to the number of pulses applied to the tissue [91].

The latter two laser-tissue processes, plasma-mediated ablation and photodisruption, are best discussed in the context of multiphoton absorption and cascade ionisation. Both processes result from a phenomenon called optical breakdown or

laser induced breakdown (LIB). Plasma-mediated ablation and photodisruption occur at very high power density around 10^{11} W/cm^2, and an exposure duration from ns to fs. Of the two processes, plasma-mediated ablation is more precise, leading to a well defined and localised ablation without mechanical effects on the surrounding tissue. Photodisruption, on the other hand, is associated with mechanical side effects such as shockwave propagation, cavitation bubble expansion and jet formation. Plasma-mediated ablation mostly occurs when using ultra-short pulses from ps to fs, due to the very high peak power achieved with minimum energy deposited to the material. The operation of a tissue using ns lasers often lead to photodisruption, as the pulse energies are high even at threshold intensity.

Among the laser processes described in this section, photochemical and thermal operate in linear absorption regime often using CW lasers. This implies that the absorption characteristics of tissue or dye (in the case of photodynamic therapy and CALI) are important in determining the range of laser parameters to achieve such processes. Photoablation, plasma-mediated ablation and photodisruption occur *via* nonlinear absorption, requiring intense pulsed lasers in order to achieve such effects. However, photochemical and thermal also occur in nonlinear regimes. Individual fs pulses may not induce significant heating of cells and tissues, but the successive application of pulses, especially with high repetition rate laser, leads to a cumulative effect which achieves significant heating [97]. Furthermore, photochemical effects such as generation of free radicals forming ROS are also observed in NIR fs nanosurgery [98].

3.2 Laser induced breakdown

Nonlinear modification of material using a laser can result from LIB of the material by applying highly intense pulses. LIB has been demonstrated in a variety of samples including solids, such as glass or silica, in liquid or tissue/cells and in the gas phase. It has been shown that LIB in water is similar to breakdown in ocular or biological media [99]. Hence, LIB for the purposes of laser nanosurgery and optical transfection will be described based on LIB in water. In order to model the breakdown process, water will be treated as an amorphous semiconductor as performed by Sacchi [100] and Vogel *et al.* [97]. As the band gap energy of water is $\Delta = 6.5$ eV, a laser wavelength of 800 nm, with a corresponding photon energy of 1.56 eV, requires five photons to overcome this band gap energy. The initiation of LIB can occur through either of the two mechanisms: direct ionisation by multiphoton absorption or *via* thermionic processes. Kennedy *et al.* [101] and Vogel *et al.* [97] provided an excellent review of these concepts. I will summarise them in the following subsection.

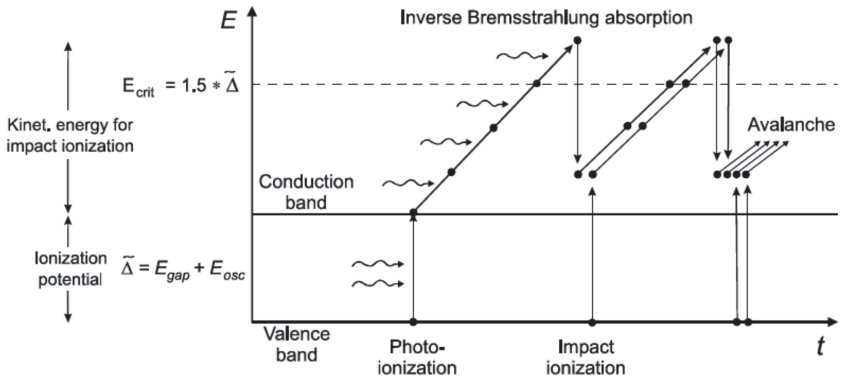

Figure 3.2: An illustration of plasma formation whereby water is assumed to be an amorphous semiconductor material. Multiphoton absorption leads to photoionisation of bound electron, inverse Bremsstrahlung, and impact ionisation. Repeated sequence of the latter two events could generate a huge growth in the number of free electrons present in the medium.-*With kind permission from Springer Science+Business Media* [97].

3.2.1 Multiphoton absorption and cascade ionisation

Essentially, a plasma is generated during the process of LIB. Plasma forms when the applied electric field is sufficient to cause ionisation of molecules and atoms. The occurrence of LIB in liquid and gas are characterised by the presence of plasma which strongly absorbs UV, VIS and IR light. A schematic diagram of sequence of events during LIB is shown in Fig. 3.2. Multiphoton ionisation occurs when a bound electron in the valence band absorbs several photons to allow photoionisation. Photoionisation is manifested when the electron is promoted to the conduction band. For ultra-short pulses with large irradiance to achieve LIB, the ionisation potential, $\tilde{\Delta}$ needs to account for the oscillation of the electron with the laser excitation field given by the expression [102],

$$\tilde{\Delta} = \Delta + \frac{e^2 F^2}{4m'\omega^2} \tag{3.1}$$

where ω and F denote the frequency and amplitude of the laser field respectively, e is the electron charge, $1/m' = 1/m_c + 1/m_v$ is the reduced mass that is given by the effective masses, m_c, of the quasi-free electron in the conduction band and m_v of the hole in the valence band [97]. When quasi-free electrons are formed in the conduction band, they can act as seed electrons for avalanche or cascade ionisation. In order for impact ionisation to take effect, the electron's kinetic energy must supersede $\tilde{\Delta}$. Quasi-free electrons created during impact ionisation may also proceed to cascade ionisation.

For cascade ionisation to arise, initial seed electrons or impurities must be present within the laser's focal volume. These are formed either by multiphoton absorption or by thermal ionisation in the medium. At high irradiances, the seed electrons absorb laser photons in a process called **inverse Bremsstrahlung**. When the seed electron is promoted to a higher energy than the ionisation potential, it can initiate impact ionisation of a bound electron, thereby producing two free electrons. This repeated events of inverse Bremsstrahlung and formation of free electrons can acquire a huge growth in the number of free electrons in the medium. Cascade ionisation is dependent on the laser irradiance, which is defined as the energy per unit area per unit time and requires the excitation laser to overcome a threshold irradiance value.

Multiphoton absorption leading to LIB requires coherent absorption of several photons to achieve the threshold for $\tilde{\Delta}$, requiring fs or ps pulses to initiate the phenomenon [91]. Q-switched ns pulsed lasers have higher threshold energies for LIB. With longer ns pulses, cascade ionisation occurs through thermionic processes leading to defects and impurities in the material, which act as seed electrons for cascade ionisation.

3.2.2 Plasma-mediated nanosurgery

In mode-locked fs laser mediated nanosurgery, the laser repetition rate is an important parameter in the extent of damage in the biological sample. Fig. 3.3 shows a schematic illustration of the interval of pulses for an amplified and oscillator-only fs laser system. Regeneratively amplified fs laser systems operate at typically kHz repetition rates and individual pulses are emitted with ms time interval. Meanwhile, oscillator-only mode-locked fs devices work at higher MHz repetition rates and have pulses separated tens of ns apart.

Although individual fs pulses may not induce significant heating in the sample [97], at sufficient pulse energy, the time between each pulses relative to the time for heat to diffuse away in the sample is an important parameter in the amount of damage on the biological sample. In fs laser waveguide writing technology, it has been observed that repetition rates of $\geq$ 200 kHz induce accumulation of energy leading to increase in melted volume on the glass [103]. Thermal confinement of the laser energy deposited is characterised by the the thermal diffusion time, T_d. Considering the thermal diffusion of water, κ= 0.7 μm$^2/\mu$s, T_d for λ= 800 nm and NA=1.2 can be obtained using the following expression [104],

$$T_d = \frac{0.124\lambda^2}{\kappa NA} \tag{3.2}$$

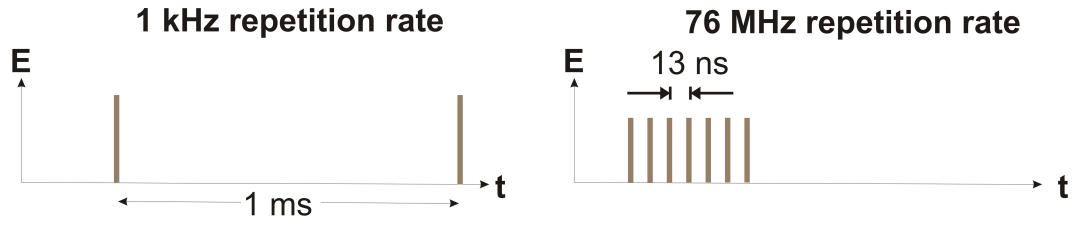

Figure 3.3: Illustration of the difference between 1 kHz and 76 MHz repetition rate fs lasers. In a kHz repetition rate laser, the deposited energy is dissipated before the next pulse arrives. Meanwhile, in high repetition rate fs lasers, there is accumulation of energy at the focal volume due to the successive application of pulses before the thermal relaxation of the sample.

which provide a T_d of 40 μs. Hence, high-repetition rate systems ($\geq$ 25 kHz) may induce cumulative heating due to the successive pulses applied, which arrive before the complete diffusion of heat out of the focal volume. For water, heat diffuses out at a rate of 0.7 $\mu m^2/\mu s$ and 40 μs after the application of the first pulse. Hence, subsequent pulses from an amplified fs laser device with pulses arriving at 1 ms interval will not lead to any cumulative effects and each pulse will interact with the material independently.

In laser nanosurgery, a certain critical quasi-free electron density, N_{crit}, must be achieved at the conduction band in order to sustain plasma growth and compensate for any losses through electron-ion recombination and normal diffusion out of the focal volume. N_{crit} is a criterion for breakdown threshold, particularly for laser pulses in ps or fs, where plasma luminescence cannot be observed. N_{crit} is given by the expression,

$$N_{crit} = \frac{\epsilon_o m_c}{e^2}\omega^2 \tag{3.3}$$

where ω is the oscillation frequency of the incident light, ϵ_o= 8.854×10^{-12} C^2 N^{-1} m^{-2} is the vacuum dielectric permitivitty, m_c= 9.1×10^{-31} kg is the mass of the electron and e= 1.6×10^{-19} C is the charge of electron [91].

From Eq. 3.3, the breakdown threshold is achieved when N_{crit}= 10^{21} cm^{-3} [97]. For λ= 800 nm, the N_{crit} = 1.8×10^{21} cm^{-3}. However, typical laser nanosurgery experiments with MHz repetition rate fs lasers were performed at much lower irradiances compared to the breakdown threshold. Plasma-mediated effects due to NIR fs pulses with MHz repetition rate occur at parameters well below this N_{crit} [97]. For example, damage was induced on unstained male rat kangaroo kidney epithelial cells (PtK2) using MHz repetition rate fs laser at considerably low average power

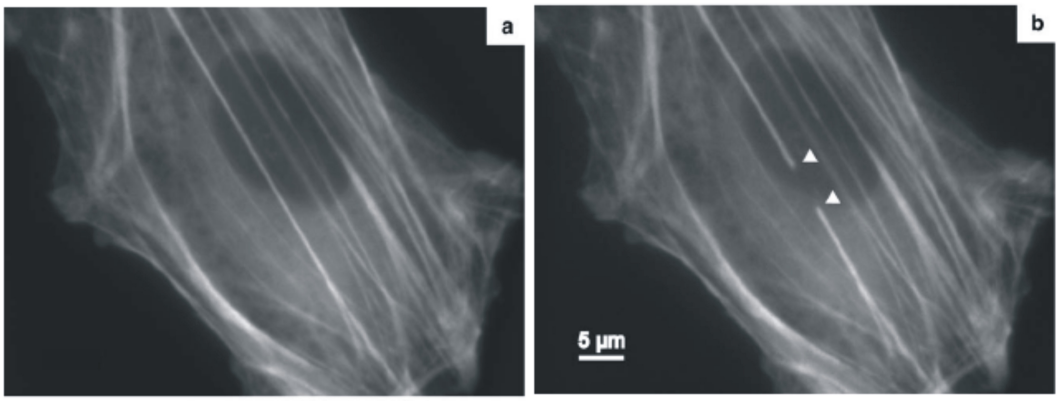

Figure 3.4: An image of an endothelial cell with stained YFP-labeled actin (a) before and (b) after laser dissection of an actin fiber bundle using a regeneratively amplified Ti:sapphire laser operating at kHz repetition rate. The triangles point to the cut ends of the actin bundles, pulling away from each other.—*Reprinted from Medical Laser Application, with permission from Elsevier* [108].

(80 MHz, 170 fs laser, P$\geq$ 7 mW, NA = 1.3, spot size =0.4 μm) [98]. The damage was attributed mainly to generation of ROS such as H_2O_2 as confirmed by cytochemical analysis [98]. Similarly, chromosome intranuclear dissection was demonstrated by König *et al.*, using the same laser at a laser power of 30 mW and irradiation time of 500 μs [105]. Furthermore, cell permeabilisation leading to transfection was demonstrated with fs lasers operating at MHz repetition rate using 50–100 mW with tens of ms exposure [25, 26]. With the parameters specified for the above-mentioned experiments, the calculated irradiance based on a diffraction limited laser beam have irradiances much lower than the breakdown threshold irradiance [97].

Hence, for MHz repetition rate fs laser systems, highly precise nanosurgery can be more accurately attributed to low density plasma-mediated effects which leads to cumulative photochemical effects [97]. These photochemical effects bring about the formation of ROS such as OH^- and H_2O_2 that interacts with biomolecules leading to either transient or permanent dissection. Recently, specific and localised DNA specific strand breaks were investigated using high-repetition rate lasers which involves the generation of highly-reactive oxygen radicals [106]. From their studies, aside from ROS generation, direct photochemical processes also occur, forming UV photo-products upon irradiation. Using oscillator-only fs lasers, at higher irradiances beyond breakdown threshold irradiance, cavitation formation occurs and temperature greater than 100 ^{o}C is attained [97, 107]. It was suggested that for highly precise nanosurgery applications, the presence of gas bubbles which displaces neighbouring cell or tissue material must be avoided.

Meanwhile, for amplifier based fs lasers operating at kHz repetition rate, the ablation of biological samples were performed at higher pulse energies, leading to thermoelastic stresses and formation of short-lived transient cavitation bubbles [97]. These effects bring about mechanical disruptions used for dissections. Although kHz repetition rate fs lasers have been effectively used for precise nanosurgery, there is an abrupt transition from weak to strong damage as a function of pulse energy and number of pulses using these laser sources [109]. Inspite of this, kHz repetition rate fs lasers have been used as effectively as MHz repetition rate fs lasers for specific applications in nanosurgery such as mitochondria ablation [108] and nanoaxotonomy for neuron regeneration studies of *C. elegans* [110]. As an example, Fig. 3.4 shows a fluorescence image of an actin network before and after laser dissection with a fs laser operating at kHz repetition rate. The image shows precise and very fine cutting of actin fiber bundles, without damaging other organelles within the cell.

3.3 Photodisruption

Using Q-switched lasers with relatively long ns pulses, laser interaction *via* LIB with soft tissues and cells results in generation of mechanical effects such as shockwave propagation, cavitation bubble and jetting. In this scenario, photodisruption occurs, leading to significant cell and tissue displacement. During photodisruption, the mechanical forces induce high amounts of thermoelastic stresses on the sample causing it to crack or split. In comparison to low density plasma-mediated nanosurgery, which provides spatially confined cutting of subcellular structures, photodisruption always results in cavitation and shockwave that limits the localisation of the interaction zone [91]. Due to this, adjacent cells or tissues are often affected.

Photodisruption leads to mechanical effects that scale to the amount of energy deposited in the sample. The threshold irradiance can be lowered using materials with large absorption coefficients. The mechanical effects occur in an ultra-fast manner often investigated using time-resolved imaging techniques. The sequence of events during photodisruption occurs with the propagation of the laser pulse and formation of a plasma. The plasma formed by LIB can produce extremely high temperatures and pressures. In liquid or biological material, the plasma created are typically very small and localised. Thermal effects within the plasma are limited and its subsequent expansion occurs adiabatically [111]. As the laser pulse propagates through the medium, the plasma continues to expand with very high velocities leading to shockwave propagation. It will also vaporise the surrounding media, creating a cavitation bubble which is filled with water vapour and gas associated with the medium [101]. As the plasma cools and the interior pressure of the cavitation

bubble decreases, the bubble will collapse. The bubble expansion and collapse have been shown to occur in the order of μs after the LIB event [112, 32]. This process repeats itself, resulting in secondary cavitation effects. The final collapse of the bubble creates residual bubbles that are formed by diffusion of dissolved gases in the focal volume [101]. Residual bubbles can persist ms to s after LIB and are visible under brightfield imaging which can experimentally determine photodisruption in cell nanosurgery experiments.

As the damage associated with photodisruption of tissue and cellular nanosurgery is often associated with cavitation bubble expansion and collapse [113, 32, 30], I will provide a background on cavitation bubble theory in the following subsection. An extensive discussion on shockwave propagation can be found in excellent reviews by Kennedy *et al* [101] and Niemz [91].

3.3.1 Cavitation bubble theory

Cavitation is the formation of water vapour and gas-filled bubble in soft tissues or liquid [101] and plays an important role in biomedical applications. It is often the main cause of damage to substrates as well as affecting tissue and cell membrane integrity. The bubbles provide a significant source of energy that have been harnessed for intraocular surgery and cell lysis. As a resulting mechanical effect of LIB, cavitation leads to disintegration of kidney stones by laser lithropsy [114], as well as many other medical applications.

Cavitation bubbles are interesting due to their violent and destructive actions when they encounter a boundary. It has been shown that the size of the bubble formed and its distance from the boundary determines the magnitude of fluid flow velocity and the presence of microjetting and counterjets [115]. The theory of cavitation bubble and collapse has been investigated since the start of 20^{th} century due to its destructive effects on solid materials, particularly in mechanical parts exposed to liquid cavitation bubbles such as ship propellers and hydraulic machineries [101]. Lord Rayleigh in 1917 first described the pressure changes due to the collapse of a cavitation bubble. The collapse time, T_c, as a function of the maximum gas bubble radius, R_B, is given by

$$T_c = 0.915 R_B \sqrt{\rho / P_o} \tag{3.4}$$

where ρ is the density of the liquid (1000 kg/m^3) and $P_o = P_\infty$ - P$_v$. P_∞ is the static pressure of the liquid and P_v is the vapour pressure of the liquid (2330 Pa at 20 ^{o}C). When the bubble collapses, the energy of the bubble can be derived from the work done of the surrounding fluid to the bubble wall boundary, which is given by the expression,

$$E_B = \frac{4\pi}{3} P_o R_B^3 \tag{3.5}$$

Substituting Eq. 3.4 into Eq. 3.5 provides the bubble energy as a function of measurable cavitation bubble parameters and can be written as

$$E_B = \frac{4\pi\rho}{3} \left(\frac{0.915}{T_C}\right)^2 R_B^5 \tag{3.6}$$

The cavitation bubble energy provides an estimate of the laser pulse energy conversion to mechanical effects. Experiments determining cavitation bubble energy using ns and ps pulsed lasers show that 72% of the ns laser energy is converted to mechanical effects compared to only 18% for ps pulses. This demonstrates that shorter pulsed laser sources, *i.e.* ps and fs laser pulses, provide finer nanosurgery effects compared to ns laser pulses [116].

3.4 Optical transfection and injection techniques

Having discussed the various mechanical techniques employed for cell membrane permeabilisation in Chapter 2 and the relevant mechanism for laser nanosurgery, in Section 3.1, I will now focus on describing laser-assisted techniques to deliver macromolecules into cells and embryos. Optical injection and transfection has been demonstrated using a variety of laser sources with differing modes of operation such as CW or pulsed mode with ns and fs pulse duration. CW based lasers have been employed for single-cell targeted delivery. In a pulsed laser operation, MHz repetition rate fs lasers, which interact with cells *via* low-density plasma, provide precise single-cell targeted delivery. Longer ns pulses generate a plasma leading to mechanical effects such as cavitation bubbles and thermoelastic stresses. Pulsed ns lasers are often employed for large-scale transfections where, the laser beam allows therapeutic treatment of many cells at a time. In the following sections, I will discuss the different optical delivery techniques using a variety of laser sources.

3.4.1 Single cell targeted delivery using continuous wave lasers

Single cell optical transfection with CW lasers is often performed using high NA objectives, dosing individual cells one at a time. The treatment is limited to the targeted cell and neighbouring cells remain unaffected. CW laser mediated optical transfection has been typically performed using argon ion lasers at 488 nm [23, 22, 24]. Palumbo *et al.* first demonstrated optical transfection using this laser source to transfect DNA plasmid constructs of β-galactosidase and chloramphenicol

acetyltransferase genes into murine fibroblasts cells [23]. Their results showed an increase in the β-galactosidase and chloramphenicol acetyltransferase activity in transfected cells compared to non-irradiated cells. Similarly, Schneckenburger *et al.* demonstrated with the same laser, 30% and 10% transfection efficiencies for young and aged CHO-K1 cell cultures, respectively [22]. Meanwhile, Nikolskaya *et al.* used an argon ion laser with laser parameters of 17 mW and 2 s, to transfect human neonatal cardiac cells, achieving 5% efficiency.

Recently, Paterson *et al.* demonstrated transfection using an inexpensive 405 nm diode laser to create stable cell colonies of CHO-K1 cells expressing GFP and Mito-DsRed protein. As argon laser systems have large footprint and occupy large table space, employing diode lasers would increase the portability of the device, providing inexpensive means for cell transfection. With CW lasers, optical transfection relies on linear absorption wherein photochemical and thermal interactions are the dominant effects. CW laser wavelengths employed were in VIS (*i.e.* 405 nm and 488 nm) while other laser wavelengths in CW mode have not been used for such applications. Importantly, several cell chromophores have absorption at these laser wavelengths, which may induce deleterious effects due to ROS generation [117]. Irradiation up to 2 s does not significantly reduce the cell viability [24]. CW lasers were focused on the cell at different focusing conditions (NA=0.4–1.25) with a range of laser energies (12–34000 μJ) to achieve successful transfection. Phenol red with typical final concentration of 15 mg/L was added to the buffer medium to aid absorption of the laser wavelength. It was conjectured that phenol red molecules absorb the laser wavelength resulting in heating and melting of the phospholipid bilayer [23, 22]. However, few studies have been conducted to understand membrane permeability changes during CW laser irradiation at this wavelength.

3.4.2 Optical transfection and injection using near-infrared femtosecond lasers

NIR fs laser based optoinjection and transfection are more mature systems compared to their CW counterparts. The difference between using the two laser sources can be understood in terms of the interaction of the lasers with the biological material. Fig. 3.5 shows a schematic diagram of single and multi-photon excitation in a sample. As mentioned previously, fs interaction with cell or tissue occurs through low density plasma-mediated process. Due to its nonlinear nature, the rate of photoionisation due to multiphoton absorption, $\mathrm{P}(\mathrm{I}_{MP})$ is given by the following expression [118],

$$P(I_{MP}) = \sigma_k I^k \tag{3.7}$$

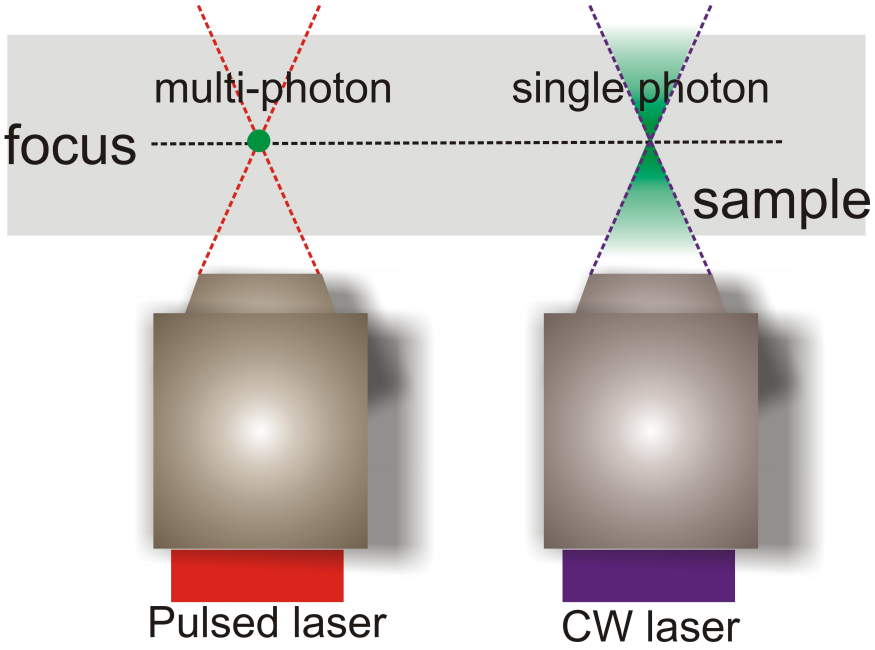

Figure 3.5: Schematic illustration of single-photon and multi-photon excitation in a sample. The pulsed and CW laser is denoted by red and blue lines, respectively with the fluorescence resulting from excitation is denoted by green. Due to the nonlinear nature of absorption using pulsed laser sources, the plasma-mediated effect only occurs at the focus. Whereas, with single photon interaction, the excitation is linear in nature, hence out-of-focus light may contribute to the effect on the biological sample.

where I is the intensity of the laser and σ_k is the multiphoton absorption coefficient for k- number of photons absorbed. Due to the Gaussian nature of the beam profile of the laser after the objective, the plasma-mediated effects only occur at the focus where the intensity is highest. In contrast to traditional CW lasers, the linear absorption occurs all throughout the beam and even the out of focus light may have an effect on the sample.

Using NIR fs lasers for cell transfection were first demonstrated by Tirlapur and König in 2002 [25]. Since then, fs lasers have been utilised with a variety of cell lines and biological systems. The system can provide high transfection rates and viability [26]. I will highlight a few studies on NIR fs laser-mediated optical transfection in this subsection. An excellent review on single-cell optical transfection is given by Stevenson *et al.* [16].

Targeted delivery using an NIR fs laser is versatile, allowing single cell and even sub-cellular poration to introduce important biomolecules into the cell. For example, Barrett *et al.* demonstrated the ability of NIR fs laser to deliver mRNA transcription

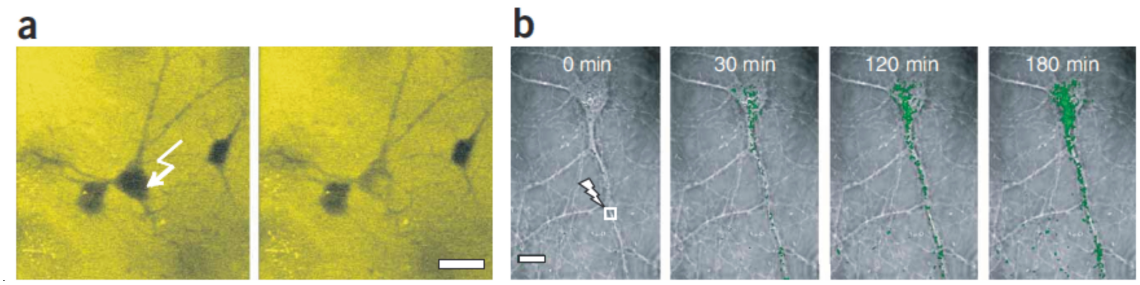

Figure 3.6: (a) Optoinjection of a membrane impermeable dye, Lucifer Yellow into living intact neurons. (b) Optical transfection of GFP mRNA into primary rat hippocampal neurons and observed up to 180 min after transfection. Scale bars, 20 μm.—*Reprinted by permission from Macmillan Publishers Ltd: Nature Methods; [17] Copyright (2006).*

factors to specific subcellular regions in an intact primary rat neuron, particularly the soma and the dendrites [17]. E-26-like protein 1 (Elk1) is a transcription factor that is localised in the dendrites [119]. In dendritic studies, it was hypothesised that mRNA activity maybe different when it is translated at different locations in the cell [17]. However, to understand how it functions during translation, spatially directed delivery must be performed in order to assess its activity. Fig. 3.6(a) shows an example of successful optoinjection of membrane impermeable dye, Lucifer Yellow into living intact neurons. A fluorescence signal is immediately detected, milliseconds after poration and delivery was localised as shown by the absence of signal from neighbouring cells. Also, GFP mRNA was optically transfected into primary rat hippocampal neurons. GFP mRNA was detected 30 min post treatment and like optoinjection with Lucifer Yellow, only the treated cell was transfected.

Hence, the technique was used to inject Elk1 mRNA into individual cells at particular regions within the neurons, specifically, the soma and the nucleus. It was found that delivery and direct translation of Elk1 in the dendrites initiated immediate cell death. In contrast, delivery of Elk1 and its subsequent translation in the soma did not alter the viability of the neuron. Understanding the mechanism of Elk1 role in cell death when delivered in the dendrites is still under further study but this result highlights the importance of subcellular delivery technique in understanding protein functionality within a cell. It opens up further investigations on how a single cell reacts at the molecular level with the introduction of small biomolecules to regionally directed sites within the cell.

The uniqueness of an NIR fs laser also stems from its ability to target and ablate in deep tissue. As explained earlier, with NIR fs lasers, the low-density plasma mediated effects only occurs at the focus with localised targeting. In addition, compared

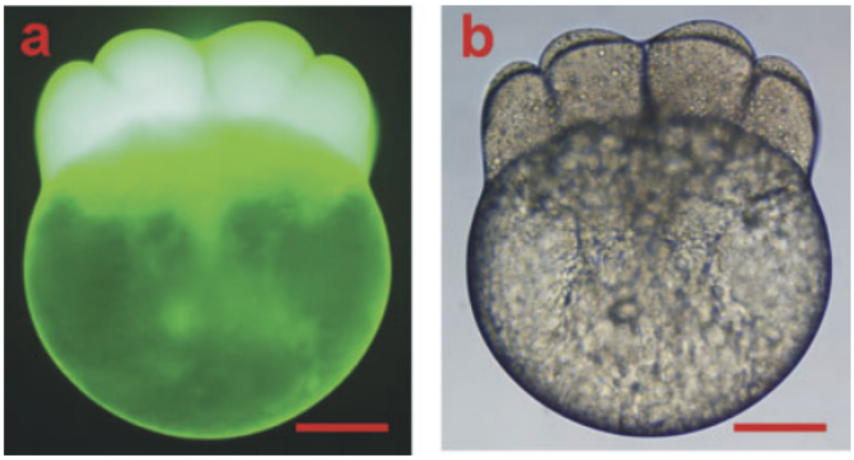

Figure 3.7: (a) Fluorescence and (b) brightfield images of a dechorionated embryo at 16-cell stage that was optoinjected in the blastomere cells to introduce FITC dye. Scale bar represents 200 μm.—*Reprinted by permission from John Wiley & Sons: Biotechnology and Bioengineering [120].*

to UV and VIS laser wavelengths, NIR light has deeper tissue penetration with less scattering. This coupled characteristic of NIR fs laser makes it an indispensible tool for optoinjecting deep within tissue without damaging the outer layers.

This was demonstrated by Kohli *et al.* on zebrafish embryos [120]. Zebrafish embryos are enclosed within a membrane called chorion which creates an outermembrane protecting the development of the embryo into a larva. Hence, techniques to deliver exogenous materials intracellularly are impeded. Methods to inject and deliver genetic constructs within individual cells in an embryo, without removing the chorion are desirable in the field of embryology. In this work, Kohli and coworkers demonstrated intracellular delivery of FITC dye and a DNA construct into the blastomere of a zebrafish embryo without removing the chorion. Fig. 3.7 shows brightfield and fluorescence image of an embryo optoinjected with FITC dye into its blastomere. This work demonstrates the unique application of NIR fs laser for intracellular delivery and does not require dechorionation of the embryos.

3.4.3 Multi-cell treatment using pulsed nanosecond lasers

Pulsed ns laser sources are effectively employed for multi-cell injection and transfection. As previously described, the interaction of long pulsed ns laser systems with a biological material is characterised by mechanical side effects such as cavitation bubble, shock wave propagation and microjetting. Hence, interaction with a pulsed

ns laser is often non-localised, treating large population of cells at a time. Currently, there are three relevant techniques using ns pulses for the purposes of cell transfection: laser-induced stress wave (LISW), optoporation and the LEAP^{TM} system. The laser-induced stress wave technique, pioneered by Terakawa *et al*, uses an Nd:YAG laser to irradiate a black rubber disk bonded with a transparent polyethylene terephthalate sheet attached to the bottom of a dish containing the cell monolayer [121]. With a single pulse of the Nd:YAG laser, a pressure wave with a μs timescale propagates in the medium. However, the efficiency of mammalian cell transfection is fairly low, less than 10% [122]. In this method, there is no direct interaction with the cells and the laser, and only the mechanical effect, specifically, the shock wave induced by the impact of the laser to the rubber sheet causes membrane permeabilisation.

Soughayer *et al.* focused the pulsed ns laser directly into the glass coverslip where the cells are attached [28]. Meanwhile, Hellman *et al.* focused the laser beam into the buffer medium of the cell to create LIB [30]. Both methods are categorised as optoporation technique. Optoporation *via* LIB in the glass or buffer medium creates cavitation bubble that expands and collapses within microseconds after the breakdown. A large zone of cell lysis (greater than 60 μm) and necrosis is created in the centre of the breakdown and surrounding cells are permeabilised in the process [30]. Fig. 3.8 shows brightfield (A,B) and fluorescence images (C,D) of cells before and after LIB on glass coverslip [28]. After the breakdown, some cells intake Texas Red dextran but remained viable, with visible Oregon Green signal, marked with a #. However, some cells (marked by a $\wedge$) are loaded but have compromised viability, observed by the absence of Oregon Green signal. The level of uptake characteristically decreases as a function of distance from the breakdown site.

The commercially available system called laser-enabled analysis and processing (LEAP^{TM}) uses a weakly focused pulsed ns laser beam to irradiate a population of cells to allow intake of exogenous biomolecules. A broad range of macromolecules from small molecules, dextrans, siRNA, plasmids, proteins, and semiconductor nanocrystals has been delivered to individual cells [29]. As the parameters used for transfection with the LEAP^{TM} system are lower than the threshold for LIB, the mechanism for delivery is conjectured to be photochemical in nature [123]. As such, this technique requires more investigation to fully optimise it for high throughput applications.

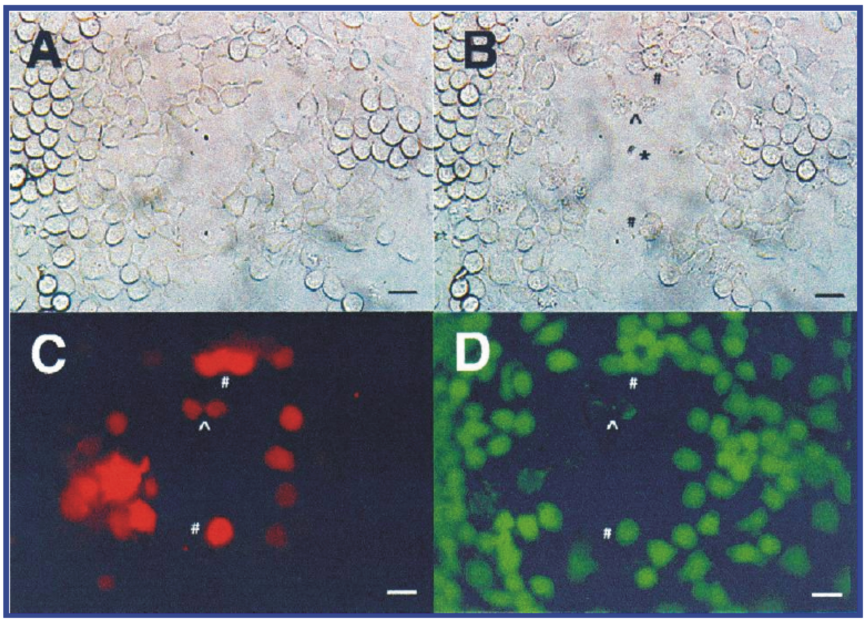

Figure 3.8: Brightfield (A, B) and fluorescence (C, D) images of cells before (A) and after (B, D) optoporation. $*$ marks where the laser beam is focused on the glass slide (B). The fluorescence of Texas Red and Oregon Green is displayed in parts C and D, respectively. Some cells (marked by a $\wedge$) are loaded but have compromised viability, observed by the absence of Oregon Green signal. Several cells that were loaded with Texas Red and have remain viable, with visible Oregon Green signal are marked with a #. Scale bar represents 20 μm.—*Reprinted with permission from [28]. Copyright, 2000 American Chemical Society.*

3.5 Summary

In summary, I have described different mechanisms for the purposes of laser nanosurgery. These laser-tissue and cell interaction can be classified into two regimes, linear mediated interaction which includes thermal and photochemical, and nonlinear mediated which includes photoablation, plasma-mediated and photodisruption. Importantly, the concept behind plasma-mediated and photodisruption was discussed by understanding LIB in water. The mechanical side effects of photodisruption were detailed focusing on cavitation bubble, the primary mechanism behind cell and tissue displacement surrounding the site of LIB.

The interaction of a laser with cells and tissues in the presence of strongly absorbing dye or photosensitisers are primarly mediated by photochemical effect. The highly reactive oxygen radicals interact with oxygen in tissue or cells causing damage or protein inactivation. Meanwhile, the temperature achieved during laser interac-

tion affects the specific thermal effects experienced by the biological samples. For single cell transfection studies, the notable temperature to consider is the gel-sol membrane transition which occurs between 42–45 ^{o}C, leading to membrane permeability changes [96]. Irreversible necrosis happens at 60 ^{o}C when cells are exposed at this temperature for several seconds.

With pulsed lasers above a certain threshold irradiance, their interaction with biological matter occurs *via* LIB, creating a plasma. LIB occurs through interplay of events such as multiphoton ionisation, inverse Bremsstrahlung and avalanche growth of free electrons. For ultra-short laser pulses such as fs and ps lasers, the initiation of LIB is mediated by multiphoton ionisation. However, for longer ns pulses, LIB arises due to thermionic process leading to defects in the media which acts as seed electrons for photoionisation. Femtosecond pulse-mediated nanosurgery is very precise and can ablate subcellular components within a cell. The precision of the technique is due to the interaction of the laser with the biological material, which occurs *via* low density plasma. Meanwhile, photodisruption is mediated by longer pulsed ns lasers. Mechanical side effects accompany photodisruption, particularly the formation of cavitation bubble, shockwave propagation and jetting when cavitation occurs near the boundary.

The interaction of lasers with cells and tissues discussed in this chapter provide us with the foundation to understand the different optical injection and transfection techniques using variety of laser sources. The mechanism behind CW laser based single-cell transfection may be due to thermal or photochemical effect but remains poorly understood. Meanwhile, targeted single-cell transfection using high-repetition rate NIR fs laser was conjectured to be due to low-density plasma, providing delicate pore formation with minimum damage on other subcellular structures. Pulsed ns lasers operate destructively due to the large threshold energy required to generate LIB. Hence, transfection based on these lasers have large zone of lysis, interacting with multiple cells at a time.

This chapter provides the foundation for the subsequent experimental work presented in this thesis. Applications of this technique for subcellular and embryo delivery would lead to great advancement in our understanding in cell and molecular biology as well as embryology. However, as each laser system has its advantages and disadvantages, further experiments should be performed in order to optimise the operation of each technique.

4

Transient transfection of mammalian cells using a violet diode laser

The main objective in this chapter is to build an inexpensive system for laser based cell transfection. Optical transfection techniques are often implemented using pulsed laser systems such as mode-locked Ti:sapphire laser with MHz repetition rate because of its high peak power allowing delivery of subnanojoule energy. However for optical transfection technology to be attainable and accessible, the cost has to be affordable and the system must have a smaller footprint. Hence, the possibility of using a simple and portable CW diode laser was explored and the mechanism for CW laser mediated transient cell transfection was elucidated.

4.1 Introduction

Previous reports of using CW lasers for cell transfection are based on argon-ion laser systems which emit multiple discrete laser lines spanning the violet to green wavelengths. Its wavelength component of 488 nm is most commonly employed for biological experiments particularly for confocal imaging. In recent years, bulky argon-ion systems have been replaced by inexpensive and compact diode lasers with good beam quality and laser stability for biophotonics application. Diode lasers have been utilised as a laser source for applications such as selective fluorescence [124],

holographic photolysis of caged compounds within neurons [125], photodynamic theraphy [126], photothermolysis [127] and confocal imaging [128].

Paterson and co-workers first demonstrated the use of 405 nm diode laser as a means to optically transfect CHO-K1 with plasmid DNA and generate stable cell colonies [31]. In this previous work, only stable transfection and not transient transfection was observed which maybe attributed to the limited amount of DNA material delivered to the cell. Although the generation of stable colonies is a routine procedure in cellular biology, as discussed in Chapter 2, this procedure can take up to weeks and can be time consuming and laborious. The generation of transient expressing cell lines allows us to circumvent the long process of selecting for stable colonies and therefore enable us to examine immediately the expression of a protein 24–72 h after transfection. This is desirable especially for pharmaceutical purposes, wherein large scale screening occurs for a particular disease. It is also important for mRNA and iRNA transfection technologies, which rely on the translation of the protein and its transient expression.

In this chapter, this transient transfection was implemented using a violet diode laser. CHO-K1 and HEK293 cells were chosen as the model systems as they are easily transfectable by other methods and are straightforward to culture. By varying the laser parameters and exposure time, a window of laser parameters was found wherein reliable transient transfection could be performed. By observing the viability of the cells at various laser parameters and calculating the temperature change during irradiation, I propose a mechanism for CW laser transfection at 405 nm in mammalian cells.

Furthermore, the technology has been applied to an important biological experiment by introducing small interfering RNA (siRNA) into cells thereby subsequently knocking down the expression of a particular protein. To demonstrate this, a modified HEK293 cell-line, which expresses the newly identified gene, willin/FRMD6 [129], was utilised for the experiments. This gene is under the control of an antibitotic inducible promoter, tetracycline. Optically transfecting a particular siRNA against willin into cells blocks the expression of the willin gene product. Although, siRNA delivery to mammalian cells has been reported for large scale mass optical transfection using an Nd:YAG laser [29], it has never been reported using CW lasers.

This work in this chapter is collaborative in nature and the significant contribution of several people should be acknowledged. The TRex-willin-GFP-HEK cell line used in the gene knockdown experiments was created by Dr. Liselotte Angus (PhD student, School of Biology). The calculation of temperature increase was done in collaboration with Martin Ploschner (PhD student, School of Physics and Astronomy). The author built the system, performed all experiments and analysis

presented in this chapter.

4.2 Materials and Methodology

4.2.1 Violet diode optical transfection system

Fig. 4.1 shows the schematic diagram of the system. The laser source was a commercially available 405 nm diode laser (Toptica, IBEAM-405-1V1) with an $M^2 < 1.2$ and maximum power of 40 mW. A telescope consisted of lenses L1 and L2 magnifies the beam. A half-wave plate and a polarising beam splitter in tandem were used to attenuate the beam power. A dichroic mirror at 45^o reflects the beam to the rear entrance pupil of a high numerical aperture water immersion, violet corrected microscope objective (Nikon Plan Apo; magnification = 63x NA =1.20).

The laser was focused to a diffraction limited spot of approximately 0.4 μm in diameter. The power at the sample plane was obtained by taking the power transmission measurements through the optics. The maximum laser power dosage for each cell was first characterised by empirically observing the cell for any signs of granulation, blebbing or necrosis. A beam shutter (Newport, UK model 845 HP-02) in front of the laser controlled the exposure setting. An exposure time of 1 s was used to observe the transfection efficiency for each power level employed. Bright field in Köhler configuration uniformly illuminates the sample. The image plane and laser plane were made coincident by changing the positions of lenses L1 and L2 and observing the image and laser focus. An xyz stage allowed us to vary the sample position. A neutral density filter was used to attenuate the beam after the tube lens. Finally, a color CCD camera (WATEC 250D) is used to capture the videos of the process. A photograph of the experimental setup is shown in Fig. 4.2(A). Meanwhile, a newly designed violet diode laser delivery system that can be fitted into one of the ports of a microscope is shown in Fig. 4.2(B).

4.2.2 Viability studies using Trypan blue Assay

For viability studies, Trypan blue is utilised to detect necrotic cells. Trypan blue is an indicator of cell membrane permeability. In the state of necrosis, the cell's protective membrane is compromised, leading to intake of extracellular material. HEK293 cells were plated on 35 mm diameter glass bottomed dishes and prepared similarly to transfection experiments except that no DNA was added. Cells were exposed to 2.1 mW and 3.4 mW laser power at exposure times from 80 ms–5 s. After laser exposure, cells are returned to the incubator for an hour, after which time 60 μL of 0.3% Trypan blue was added. Dead cells stained blue were counted

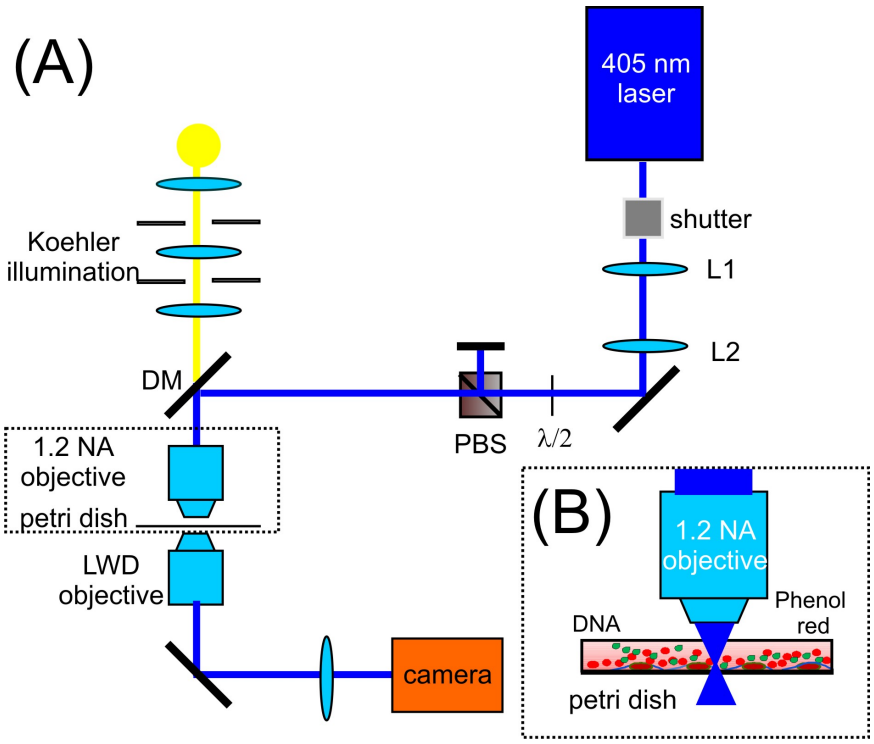

Figure 4.1: Schematic of an optical transfection system using a 405 nm diode laser. L -plano-convex lenses (L1= 50 mm and L2= 100 mm); PBS- polarising beam splitter; $\lambda/2$ - half-wave plate; M- mirrors; DM- dichroic mirror; LWD- long working distance objective. The whole system is mounted on a 60 × 90 cm optical breadboard. (B) The inset shows a schematic layout of a prepared sample in a petri dish showing the laser beam focused on a cell bathed in DNA and phenol red solution [130].

and the viability was calculated by obtaining the percentile ratio of dead cells with irradiated cells. Each data point is an average of 3 dishes, each containing 50 cells which were exposed to the laser.

4.2.3 Transmission measurement of the objective

The laser powers described in this chapter are based on the laser power delivered to the sample. Ideally, the transmission of the objective is measured by using a dual objective method. Taking the square root of the power loss provides the transmission of the light through the objective while taking into account the loss through the sample and immersion fluid used. However, since only a single objective is available, the transmission of the objective is measured by replacing the dichroic mirror with a 50:50 beamsplitter. A dielectric mirror with a drop of water on top is placed

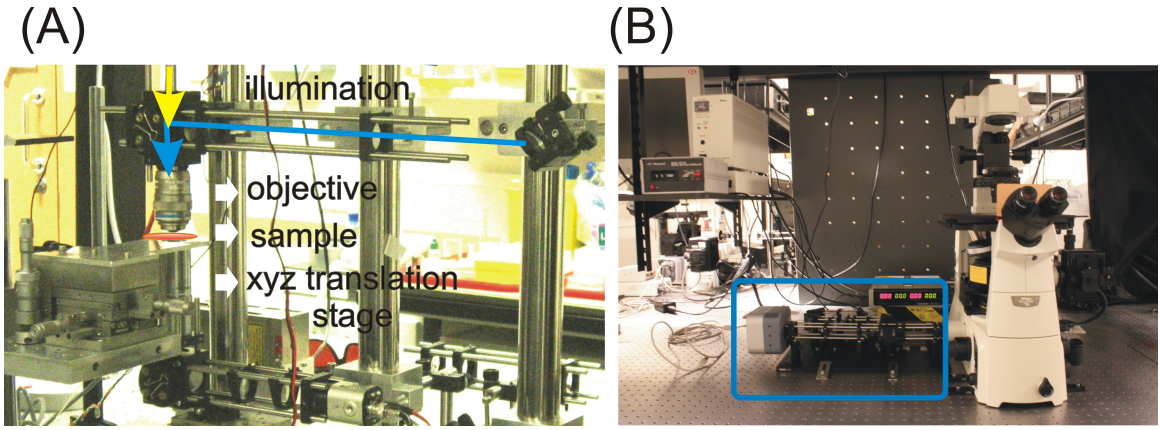

Figure 4.2: (A) Photograph of the experimental system used for the experiments. Shown is the laser beam (blue line) directed into the microscope objective and the illumination (yellow line) coming from above. (B) A newly designed violet diode laser delivery system that can be fitted into one of the ports of a microscope.

on the sample plane. After being reflected by the dielectric mirror, the beam has traversed the objective twice and the power loss can be obtained based on the incident and output power. Based on this measurement, the objective used in this experiment has a transmission efficiency of 84±1% at 405 nm laser wavelength. Each optical component reflection/transmission characteristic is accounted for and that the dielectric mirror used has a flat reflectivity (99 %) covering a range of angles.

4.2.4 Sample preparation for DNA optical transfection

All cell culture methods are discussed in the Appendix. 60-70 μL of CHO-K1 and HEK293 cells were seeded at a density of 2.4 x10^4 cells per mL onto 35 mm diameter glass-bottomed culture grade dishes (World Precision Instruments) to achieve 40-50% confluency. The cells were incubated at 37 ^{o}C for 24 h to allow cell attachment to the bottom of the glass dishes. Meanwhile, TRex-willin-GFP-HEK cells were plated 48 h prior to the experiment onto 35 mm culture dishes coated with Laminin (Invitrogen, UK) to improve their adherence on the dishes.

For each optical transfection experiment, individual CHO-K1 and HEK293 cells were exposed to up to 3.4 mW of laser power for 1 s at the focus. Before exposure, the cell monolayer was washed twice with OptiMEM (Invitrogen, UK) and then bathed with 30 μL solution containing 10 μg/mL plasmid DNA encoding for Mito-DsRed (Clontech) and 42.2 μM of phenol red (Sigma) in OptiMEM. Phenol red is a dye commonly used with cell culture medium to detect changes in pH. The absorption of

the solution used in the optical transfection experiments was measured and a molar coefficient cross section of 1.4 x 10^4 cm^{-1} M^{-1} at 405 nm was obtained.

A Type 0, 22 mm diameter coverslip was placed on top of the cell monolayer and a region of interest of approximately 1 cm in diameter was marked in the bottom of the dish in order to identify the region of dosed cells. The position of the laser was marked on the screen and by adjusting the position of the sample using the xyz stage, each cell was moved one by one to this location. On average, 50 healthy looking cells per dish were irradiated on the plasma membrane in a region 1–3 μm away from (and not directly above) the nucleus. The sample was always moved in a unidirectional pattern and always downwards upon reaching the edge of the marked region to ensure that each cell is irradiated only once. After dosage, the coverslip was removed with OptiMEM and phenol red solution, and then the cells were subsequently washed twice with the same medium. The cells were further incubated in fresh medium for up to 72 h after optical transfection. Control cells were prepared in the same manner but were not exposed to the laser.

The transfected cells were observed under a fluorescent microscope for expression of the Mito-DsRed gene. For each laser power and for each exposure time, 9 experiments were performed irradiating 50 cells per dish in the process. In calculating the transfection efficiency, the number of fluorescent cells 72 h after transfection was counted and the percentile ratio of this with the number of irradiated cells was obtained. This may result in an overestimate as cells continually divide and proliferate. A more accurate assessment would be to obtain the average growth rate of successfully transfected cells over 72 h and the number of fluorescent cells with this factor. However, this is not straightforward process as the rate of cell division depends on many factors and might be variable depending on differences in sample preparation. For simplicity purposes, I obtained a relative figure as a representation of our efficiency. In total, for n= 9 experiments, ≈5000 cells (including irradiated cells on control dishes without DNA) were treated allowing us to accumulate reliable statistics of the process.

4.3 Experimental Results

4.3.1 Viability tests with varying laser power and exposure time

The state of cellular viability is an important criterion to consider in order to achieve optical transfection. Viability is defined as the ability of a cell to perform its normal and physiological processes, resulting in mitosis. There are several methods available to assess cellular viability. The most obvious and most commonly employed method

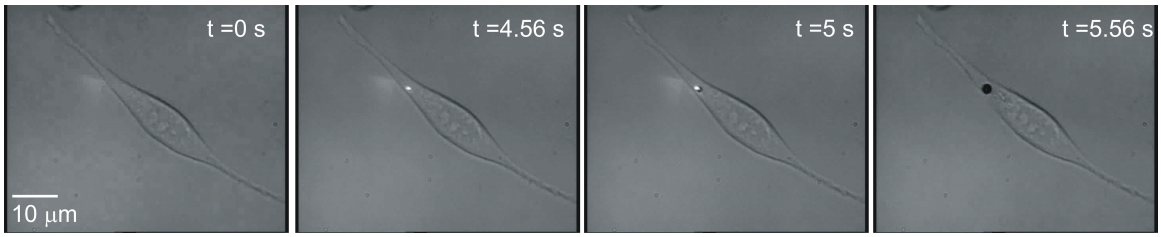

Figure 4.3: Time lapse imaging of an irradiated CHO-K1 cell with a 405 nm focused diode laser at P= 18 mW . A cell was irradiated starting at t=0 s. A strong backscattered signal was observed after ≈3 s of irradiation, afterwhich a visible bubble gas bubble was produced on the cell. A black mark is left on the irradiated part of the cell after 5 s of laser exposure.

is observing any morphological changes to the cell by detecting presence of cell blebbing and granulation, which is physical evidence of necrosis. On the other hand, to quantify the percentage of cell viability in a population, the exclusion of membrane dyes are employed. In this section, the parameters for optical transfection were narrowed down by determining the parameters that would provide a good percentage of viable cells.

Several experiments were performed to characterize the power (P) and exposure time (T) required to retain viable cells after irradiation with the focused violet laser. CHO-K1 and HEK293 cells were irradiated with the focused violet laser with varying laser power and exposure time. The laser power was measured using a sensitive broadband power and energy meter system (CVI, Melles Griot, 13 PEM 001/J) capable of measuring laser powers between 10 μW–2 W. Power measurements were taken at the backaperture of the objective. The corresponding power at the sample plane was calculated by multiplying the transmission of the objective with the measured power.

For irradiated cells, the cellular morphology was observed for signs of necrosis. At a P= 18 mW, after a few seconds of irradiation, backscattered light was observed at the irradiated site and a gas bubble was created on the membrane which collapsed when the laser was cut-off (shown in Fig. 4.3). After exposure to the laser, the cell irradiated at this laser dosage showed granulation and nuclear condensation.

Hence, lower P were tested for varying T. At P= 3.4 mW and T= 10 s, the presence of plasma membrane blebs was observed followed by the cytoplasm became increasingly granulated and the nuclear envelope becoming more pronounced. Membrane blebs are spherical extensions in the membrane which are characteristics of early stage apoptosis [131]. There is evidence that at the onset of bleb formation, the cytoplasm completely separates itself from the cytoskeleton [131]. During me-

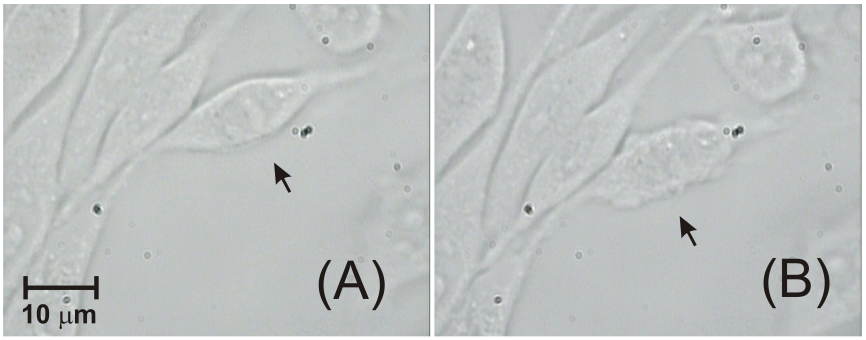

Figure 4.4: (A) Image of a cell before irradiation and (B) after irradiation. Membrane blebs are formed after irradiation of focused violet diode laser using P= 3.4 mW and T= 10 s on CHO-K1 cell.

chanical and chemical induced stress, blebs can grow as large as the cell's diameter and sometimes are nonretractable. Due to the overextension of plasma membrane, it exceeds the tensile stress allowance for the membrane, thus the cell fails to recover contributing to its lysis.

The exposure time was shortened incrementally by 2 s and the morphological changes on the cell was further observed. Shorter T, delayed the signs of membrane damage instead of immediate cell death after irradiation. Notably, membrane blebs were not only found on the irradiated area but were also found all over the cell. This may imply that the photodamage on the cell due to the focused violet laser encompassed the whole cell and not just the site of irradiation.

Based on these morphological changes at the laser powers mentioned, the possible laser dosage parameters for optical transfection were further constrained by performing a dye exclusion assay on HEK293 cells exposed to focused violet laser. The parameters P= 2.1 mW and 3.4 mW were chosen for the viability experiments. All cells exposed to 2.1 mW and 3.4 mW for T= 6–10 s immediately showed blebbing and granulation which was interpreted as compromised viability. This further narrow down the potential optical transfection exposure settings to $T < 6$ s. Hence, cells were treated with shorter exposure to the laser (T= 80 ms to 5 s). Fig. 4.5(A) shows the percentage of cells that remained viable after exposure to the laser.

Necrotic cells stained with Trypan blue are shown in Fig. 4.5(B). In general, viability was observed to decrease with increasing laser exposure time. For a 1 s exposure, viability was found to be 96.4±1.2 and 95.4± 1.2% for laser powers 2.1 mW and 3.4 mW respectively. The viability marginally decreased from 86.7±1.2 to 65.3±4.2% with 3.4 mW at 2 s respectively. This small increase in laser power from 2.1 mW to 3.4 mW resulted in a sharp 6-fold decline in viability at 3 s exposure times

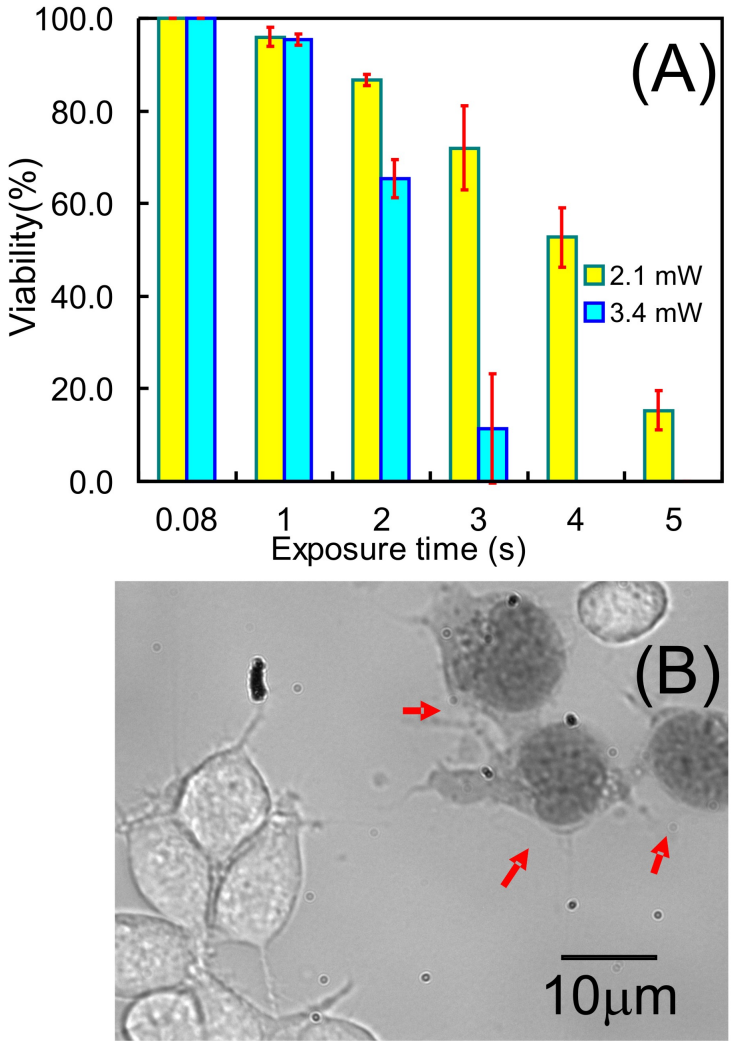

Figure 4.5: (A) Viability of HEK293 cells exposed to laser at 2.1 mW and 3.4 mW at the focus at varying exposure time. Error bars represent ± standard deviation (n=3 experiments of 50 dosed cells). (B) Bright field image of laser exposed HEK293 cells. Cells pointed by the red arrows were irradiated with the laser and have taken up the Trypan blue dye, a sign of cellular necrosis [130].

from 72±9.2 to 11.3±12.1%. LD50, defined as dosage entailing 50% cell viability occured at an energy density of 6.3 MJ/cm^2.

In order to further understand the relationship between the viability and the laser parameters, the normalised viability in log scale was plotted as a function of laser energy (E), wherein $E{=}P{\times}T$. For energies $<$ 10 mJ, the log of viability follows an exponential curve as a function of energy dose as shown in Fig. 4.6 and follows the

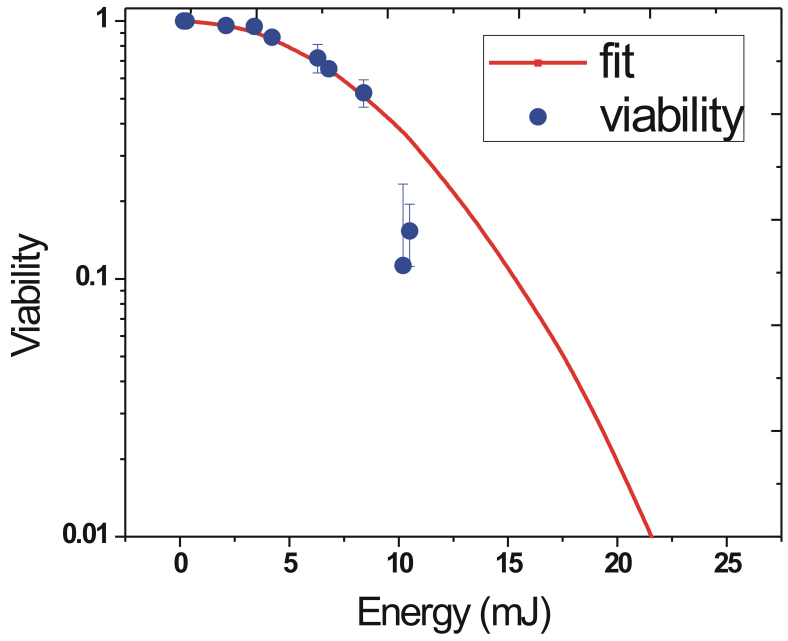

Figure 4.6: Log of viability (V) as a function of energy dosage (E). Data points below E= 10 mJ follow a survival function given by Eq. 4.1.

relationship [132],

$$V(E) = e^{-\alpha E - \beta E^2} \tag{4.1}$$

where α= -0.005 and β= 0.01. The exponential decay depicts a low-dose rate response at E<10 mJ wherein single-strand breaks often occur with surviving fraction of cells still managing to repair itself after irradiation. However, beyond 10 mJ, the data fit follows a faster rate of decay (α= -0.005 and β= 0.025) which may imply, a threshold laser energy dose leading to more direct cell necrosis such as double-strand breaks with minimal surviving fraction of cells (0-10 %). The viability study demonstrates the sensitivity of the mammalian cells to violet-blue light irradiation at even modest laser energy.

The toxicity of violet-blue laser in mammalian cells has been previously investigated. It has been shown that at certain levels of irradiation of violet-blue light, the interaction induces photodamage through absorption by cellular endogenous photosensitisers [117] which subsequently leads to adverse chemical reactions. Possible cellular chromophores absorbing in the violet-blue region include porphyrin

ring structures and flavins [133, 134, 135]. In addition, Hockberger and co-workers reported induced damage by violet light (400-410 nm) from a xenon arc mercury lamp on mammalian cells. This damage was thought to be due to the stimulated production of H_2O_2 by photoreduction of flavins and/or flavins containing oxidases located within the mitochondria and peroxisomes [135]. ROS production was also observed using an NIR fs laser pulses which they attribute to 2-photon absorption. Oxidative stress may lead to several structural deformations such as: fragmentation and condensation of nuclei; DNA strand breaks and loss of membrane protective functionality leading to cell apoptosis [25]. Despite this, good viability of 90% to 100% was obtained with optimal laser power and exposure time (P= 2.1 mW and T $\leq$ 1 s; P= 3.4 and T $\leq$ 1 s) of the focused violet diode laser.

4.3.2 Optimisation of optical transfection efficiency

Successful transient expression was achieved with the Mito-DsRed DNA plasmid for both cell lines as shown in Fig. 4.7(A and B). In contrast to previous work [23, 22] which reported small dark circular spots on the cell that disappeared several minutes after laser irradiation, these dark spots were not observed during our experiments. More conclusively, these dark circular spots repeatedly appeared for cells irradiated with laser parameters beyond a therapeutic dosage. No visible reaction, hole or cavitation bubble from the cell was observed using the laser and exposure times described in this chapter for successful transfection. Whether DNA transfection using CW lasers necessitates a nano-size hole is not yet confirmed, but the increase in membrane permeability may be enough to allow circular DNA plasmid to enter inside the cell through the cell membrane. Further studies will be needed in order to discover the changes within the membrane structure at the site of laser irradiation.

The transfection efficiency after 72 h as a function of laser power, using a 1 s exposure time for HEK293 cells, is shown in Fig. 4.7(C). Each power level results in a transfection efficinecy that is significantly different from the control group ($p<0.05$) with the exception of 0.8 mW, as determined by One-Way Analysis of Variance (ANOVA) followed by Dunnett's statistical test. The start and tail of the plot were significantly different from each other as determined from ANOVA followed by Fischer's pairwise test ($p<0.05$). As indicated in Figure 4.7(C), an enhanced transfection efficiency was observed upon increasing the laser power from 0.8 mW to 1.3 mW with efficiencies of 3.4±3.4 to 28.6±6.3%, respectively; showing a power dependence on the probability of cell poration and subsequently transfection. The optimum laser power was found to range from 1.3 mW to 2.5 mW which yielded transfection efficiencies between 28.1±5.8 and 36.6±4.8 %. Within this range of power level, the efficiencies were not significantly different from each other but were

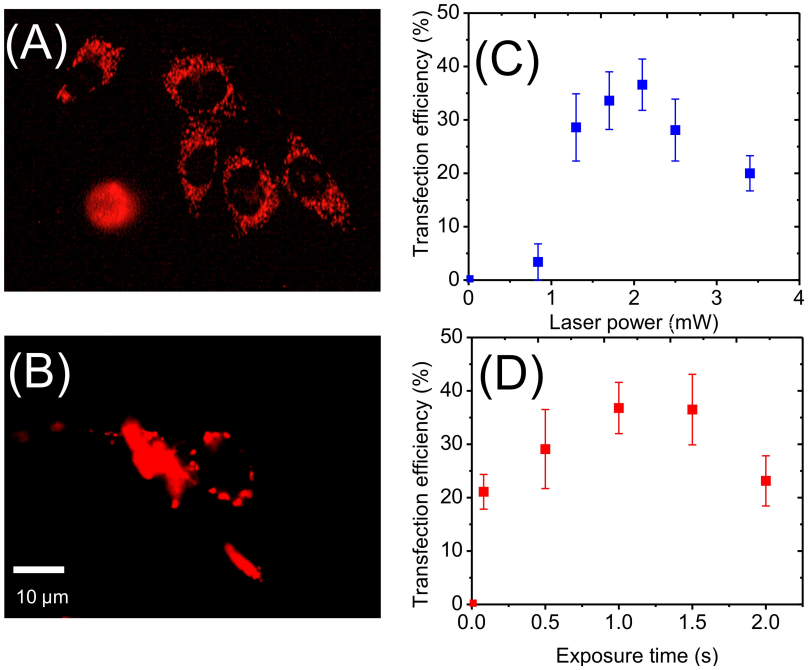

Figure 4.7: Fluorescence images of (A) CHO-K1 and (B) HEK293 cells transfected with Mito-DsRed plasmid. (C) Transfection efficiency of HEK293 cells as a function of laser power at the focus using 1 s exposure time. (D) Transfection efficiency of HEK293 cells as a function of laser exposure time at 2.1 mW. The error bars represent ± standard deviation. (n=9 experiments of 50 dosed cells) [130].

significantly different from 0.8 mW and 3.4 mW ($p<0.05$). Since the mitochondria were tagged for transfected cells, it was possible to observe their streaming, which is an indicator of the overall health of the treated cells.

The transfection efficiency of HEK293 cells was also determined as a function of laser exposure time for a fixed laser power of 2.1 mW. Fig. 4.7 (D) shows the transfection efficiency as a function of irradiation time from 80 ms-2 s. ANOVA followed by Dunnett's statistical test showed that transfection efficiencies obtained from different exposure times were significantly different compared to the control ($p<0.05$). Though significant transfection efficiency can already be obtained at 80 ms exposure, 1.0 s and 1.5 s appeared to be optimal for transfection at this laser power. Increasing the exposure time from 1.5 s to 2 s, resulted in the decline of the average transfection efficiency from 36.5±6.6 to 23±4.7%, respectively.

The parameters represented here are not exhaustive and optimal settings may still vary depending on the type of cell and environmental conditions. Each cell line, due to its differing chemical functions and properties can have diverse reactions to irradiation from a given laser. For example, the maximum transfection efficiency obtained for CHO-K1 at 2.1 mW and 1 s exposure time was only 23±1.5% compared to 36.6±4.8 % for HEK293 cells. Hence, application of this technology to different cell types may require further optimisation.

Along with transfection experiments, control experiments were performed by preparing dishes of cells in DNA solution but without laser irradiation. Control dishes were prepared and treated in the exact same manner as the experimental samples. 72 h after the experiment, the control dishes were also checked for fluorescence and expression of Mito-DsRed protein. The level of spontaneous transfection was found to be consistently very low (0-3 cells per dish) and negligible in comparison to the transfection efficiencies achieved. Spontaneous transfection is defined as cells expressing the protein without exposure to the laser irradiation.

From the transiently transfected cells, it was also possible to select cells with integrated DNA in their nuclear genome using the antibiotic, Geneticin/G418, and thus enables generation of stable colonies from the transiently transfected cell lines, as shown in Fig. 4.8. Two days after optical transfection, fresh medium was added with 0.5 mg/mL G418 (Invitrogen). Over time, cells that have not integrated the DNA in their genome die. Over the period of two weeks, colonies expressing the Mito-DsRed protein started to grow.

In comparison to previous studies, the laser energy used in this present work was of the order of 2000 μJ, compared to only 12 μJ used by Paterson *et.al* [31]. Successful transient transfection using our CW focused 405 nm laser required an energy density of 1.5 MJ/cm^2 which is in close agreement with the energy density

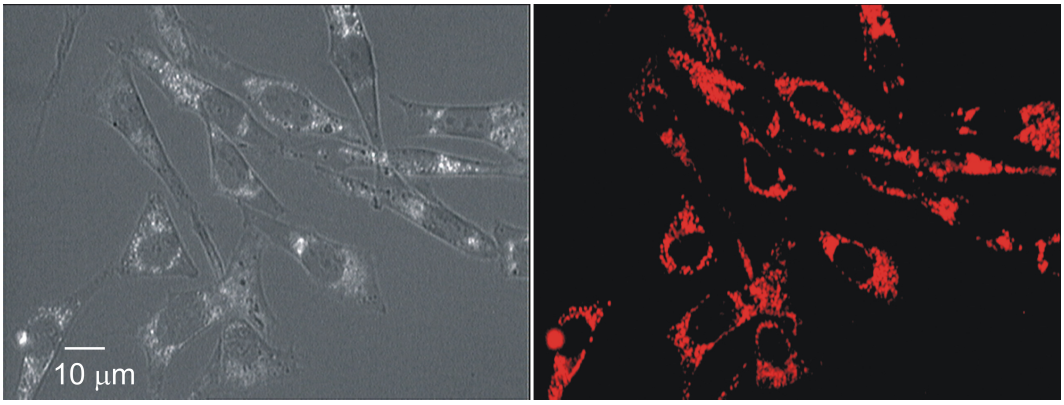

Figure 4.8: Brightfield (LEFT) and fluorescence (RIGHT) images of stable cell colonies obtained by transiently transfecting CHO-K1 cells at laser power of 2.1 mW and 1 s exposure time.

reported using focused 488 nm argon-ion laser (1 MJ/cm^2) [22].

4.3.3 Gene knockdown using the violet diode laser

RNA interference (iRNA) is a technology developed by Fire and Mello in 1998 [136], which allows the knockdown in expression of a specific gene. Small interference RNA (siRNA) interferes with new protein expression, resulting in silencing of the gene. siRNA are short oligonucleotides with lengths of 20-25 nucleotides which bind specifically to the mRNA of the protein of interest. This leads to the formation of a siRNA complex, which results in mRNA cleavage and its subsequent degradation [137]. The applications of this widely used gene silencing technology include studying a gene's function, but also the potential therapeutic modification of gene expression in human diseases. Hence, the application of the violet laser transfection by demonstrating its feasibility to deliver siRNA into mammalian cells and knockdown a particular protein called willin [129]. The sequence of this protein is found in Appendix.

Modified HEK293 cells with the tetracycline inducible protein, willin-GFP, which I refer to as TRex willin-GFP-HEK cells were utilised for this experiment. The expression of willin can be induced with the addition of 1 μg/mL tetracycline to activate willin-GFP expression. Willin knockdown was performed using siRNA with a final concentration of 5 nM, specifically targeting the protein (GACAGAGCAGCAAGAUACUAUUAUU, CACAGACUAUAUGUCGGAAACCAAA, GCCUCUAUAUGAAUCUGCAGCCUGU; Invitrogen). The protocol for chemical transfection and corresponding western blot is found in Appendix. Western blot analysis shows

that willin-GFP expression is significantly reduced after 48-72 h of siRNA transfection [130]. This therefore indicated that the siRNA used were specific and effective in decreasing willin expression.

Therefore, for the gene knockdown experiments, 5 nM stock of the siRNA duplexes with the Mito-DsRed encoding plasmid was added to the transfection medium. 10 μg/mL of Mito-DsRed was also added in order to identify cells that had been successfully transfected. Cells were targeted using 3.4 mW laser power at the focus and a 1 s exposure time. Control dishes included: (a) cells with Mito-DsRed plasmid and siRNA, without laser treatment, (b) cells without Mito-DsRed plasmid but with siRNA, without laser treatment (c) cells without both the Mito-DsRed and siRNA with laser treatment. Expression of willin-GFP was then induced by the addition of tetracycline and cells were monitored for fluorescence over the next 2 days. For all control dishes, spontaneous DNA transfection or knockdown was not observed.

Fig. 4.9 shows images of optically transfected TRex willin-GFP-HEK cells in the presence of the willin specific siRNA and the Mito-DsRed plasmid. In the left panel of Fig. 4.9(A) is a successfully transfected TRex willin-GFP-HEK cell, as shown by the expression of mitochondrial targeted red fluorescent protein. The center image (Fig. 4.9(B)) is the same field of view but under bright-field imaging. The right hand panel (Fig. 4.9(C)), shows the green fluorescent cells. Blue and red arrows are cells which exhibit clear knockdown of willin-GFP expression as indicated by the absence of green fluorescence. For one cell, indicated by the red arrow point is a cell which was co-transfected with Mito-DsRed encoded plasmid and siRNA. The laser's specificity of action is indicated by the fact that untreated cells have neither been knocked down nor transfected with Mito-DsRed, as observed by lack of fluorescence in all control dishes checked under fluorescence microscope.

Interestingly, there were more occurrences of gene knockdown with the siRNA than of DNA transfection as shown in Fig. 4.9(C) where cells (blue arrows) had knockdown of willin-GFP expression but were not expressing Mito-DsRed. It can be deduced that the efficiency for gene knockdown will be higher compared to DNA transfection as smaller siRNA molecules are more mobile than DNA plasmids (*i.e.* 25 bp versus 5000–6000 bp). To understand this, it was assumed that there is a simple passive diffusion event for DNA or siRNA from the extracellular medium to the cytosol during optical transfection. Based on this model, one can compare the rate of diffusion of plasmid DNA and siRNA. The diffusion coefficient, D_f [138] is obtained using the equation,

$$D_f = \frac{k_B T_p}{6\pi\eta_v R_G} \tag{4.2}$$

where k_B is Boltzmann's constant, η_v is the viscosity of the medium and T_p is

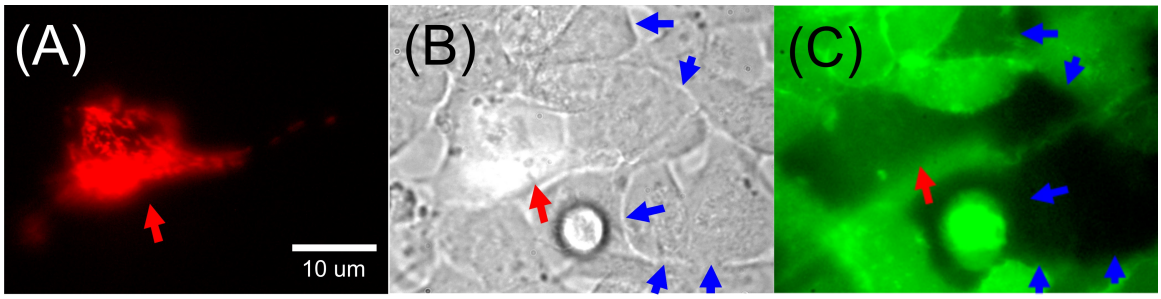

Figure 4.9: Gene knockdown using a violet diode system. (A) A TREX-willin-GFP-HEK cell fluorescing red due to the expression of the Mito-DsRed and (B) under brightfield imaging. (C) Image of the same field of view showing GFP fluorescence and non-fluorescing cells. Red arrow points to a cell which has been co-transfected with Mito-DsRed and willin specific siRNA. Blue arrows point to cells that have been transfected with siRNA only [130].

the temperature in Kelvin. Meanwhile, Prazeres provided an estimation of R_G for super-coiled DNA plasmids described by [139],

$$R_G = 0.402 \times N \tag{4.3}$$

where N is the number of base pairs. For siRNA, the Flory scaling law applies and the radius of gyration is given by

$$R_G = 5.5 \times N^{1/3} \tag{4.4}$$

Based on these equations, 25 bp siRNA diffuses approximately 100x faster than a 5600 bp plasmid DNA allowing more siRNA molecules to diffuse into the irradiated site.

4.4 Mechanism of violet diode laser poration

Based on previous studies using the 488 nm argon-ion laser for cell transfection, it was conjectured that a melting of the phospholipid bilayer occurs due to the light absorption of phenol red molecules in the medium causing localised thermal effect on the irradiated site [23, 22]. To elucidate the mechanistic process of poration, an estimate of the temperature at the beam focus was calculated based on modeling the phenol red as a sphere of radius, r, immersed in a non-absorbing medium. Since the absorption and the consequential increase in temperature occur only in close proximity at the focus, one can assume that the laser energy is absorbed only by

the phenol red sphere. The radius, r of the sphere can be made equivalent to the radius of the beam spot by,

$$r = \frac{0.61\lambda}{NA} \tag{4.5}$$

where λ = 405 nm and NA= 1.2. Since most of the incident power of the laser goes through the sphere of radius, r, we can assume that the substitution of a focused Gaussian beam with a plane wave of incident intensity where P is the power of the laser at the focal plane going through the geometrical cross-section of the sphere, will not introduce any significant error to our estimate. The Mie scattering problem may be solved for the phenol red sphere surrounded by the non-absorbing medium [130]. The imaginary part of the index of refraction of the phenol red sphere was determined by the equation,

$$\hat{n} = n\left(1 + i\frac{\alpha\lambda}{4\pi n}\right) \tag{4.6}$$

based on the measured absorption coefficient, α= 0.6 cm^{-1}, noting that the change in real part of the index of refraction, n is negligible. This yielded an expression for the index of refraction given by

$$\hat{n} = 1.33 + i1.93 \times 10^{-6} \tag{4.7}$$

The solution provided the absorption cross section of the phenol red sphere which is σ= 2×10^{-18}m^2. Hence, the heat absorbed, Q by the phenol red can be obtained, wherein

$$Q = I\sigma = 3 \times 10^{-8} W \tag{4.8}$$

During CW irradiation, one has to take into account the considerable heat loss due to heat flow into surrounding medium. The heat flow, $\boldsymbol{j}_Q$ is proportional to temperature gradient, ∇T_p given by the diffusion equation [91],

$$\mathbf{j}_Q = -k_o \nabla T_p \tag{4.9}$$

where k_o is the thermal conductivity. Since the CW laser is focused at a very small volume (1×10^{-20} m^3), the temperature diffuses and achieves steady state very rapidly. The steady state temperature increase, ΔT_p can be characterised by the thermal diffusion of the absorbed heat to the surroundings and is mainly dependent on thermal conductivity of the surrounding medium. Considering that the steady state temperature is achieved within several μs [97] and the irradiation settings used in the experiments were of the order of ms to s, one needs only to consider the ΔT_p

for the calculated heat absorbed Q. To obtain ΔT_p, Q can be equated to the integral of Eq. 4.9 over the sphere boundary, which is given by the expression [140],

$$\Delta T_p = \frac{1}{4\pi}\frac{Q}{k_o r} \tag{4.10}$$

where k_o= 0.6 W/mK is the thermal conductivity of water. From this, the calculated ΔT_p is 0.02 K or 0.02 ^{o}C.

The temperature calculation at the focus in the phenol red medium revealed that the gradient temperature is very small $\approx$ 0.02 ^{o}C. Since the experiments were performed at 25^{o}C, the calculated temperature change is insufficient to achieve the reported temperatures of 42–45^{o}C, which are necessary for a membrane phase transition [96] and is certainly well short of the required temperature rise required for microbubble formation [97]. Interestingly, the experiments revealed that cell poration was dose dependent, varying as a function of both exposure time and average power. If photothermal effect is minimal then this result suggest that a dose dependent photochemical reaction dominates during irradiation of a focused 405 nm laser, affecting membrane integrity.

Photochemical reactions leading to cell membrane permeability changes may arise from production of reactive oxygen species (ROS) such as $O2^-$, OH^* and H_2O_2 radicals. These radicals induce oxidative stress and are known to be elicited by the irradiation of light at this wavelength region [133, 134, 135], which may lead to subsequent lipid peroxidation, closely related to possible impairment of the phospholipid bilayer [141]. At the site of irradiation, localised generation of ROS and its interaction with the lipid bilayer may cause changes in the permeability state of the cell. The involvement of oxidative stress in optical transfection remains poorly understood and requires sophisticated time-resolved fluorescence imaging which is beyond the scope of this chapter.

However, the involvement of ROS in this process was confirmed as the addition of phenol red in the medium was observed enhanced the overall transfection efficiency as shown in Fig. 4.10. Phenol red has been shown to protect cells against the harmful effects of ROS [142]. At the site of irradiation, the intracellular ROS diffusing locally impairs the cellular membrane leading to the uptake of the DNA. It can be presumed that although the phenol red molecules will not inhibit the localised formation of intracellular ROS at the membrane, it will deactivate the extracellular ROS that diffuse far from the irradiation site and compromises the overall viability of transfected cells.

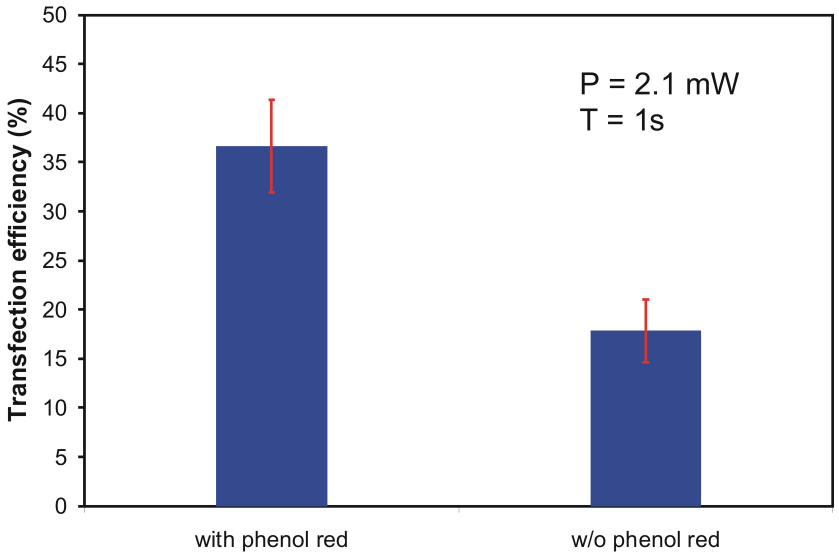

Figure 4.10: A comparison of transfection efficiencies obtained for HEK293 cells using 2.1 mW at 1 s exposure time for cells in transfected in with and without phenol red. Error bars represent ± standard deviation. (n=9 experiments of 50 dosed cells)

4.5 Conclusion and Future Work

In this chapter, a compact and cost-effective optical transfection system was built using a violet diode laser. With this technique, mammalian cell lines such as CHO-K1 and HEK293 cells can be robustly and reliably transfected with an efficiency of up to 40%. Furthermore, the chapter reports results on the transfection efficiency as a function of parameters, laser power and exposure time. The mechanism of optical transfection using a CW violet diode laser was elucidated by calculating the change in temperature at the focus.

Prior to transfection experiments, the parameters in which cells remain viable after irradiation of focused violet diode laser were determined based on morphology and Trypan blue viability assay. Morphological changes on the cell showing blebbing and granulation of the cytoplasm provided the initial upper limit at which viable irradiation could occur. Furthermore, a systematic viability study after irradiation using P= 2.1 and 3.4 mW for T= 80 ms–5 s. An exponential decay of viable cells were obtained with increasing P and T. For P= 2.1 and 3.4 mW for T $\leq$ 1 s, a high percentage of viability of 90–100% was obtained.

Hence, optical transfection of plasmid DNA using focused violet diode laser was performed for P= 2.1 mW with varying T= 80 ms–2 s as well as fixed T= 1 s

and varying P= 0.8 mW–3.4 mW. The results showed that the efficiency of CW optical transfection strongly depends on laser power and exposure time. A dose dependent curve was obtained with varying laser parameters. Even a short exposure of 80 ms yielded a transfection efficiency of 20% but increasing the exposure to 1.5 s further increased the efficiency. With longer exposure time, $\geq$ 2 s, and higher power $\geq$ 2.1 mW the efficiency decreased, which can be attributed to the loss of significant viability of the irradiated cells. The maximum achievable transfection efficiency using this technique is around 40%.

To extend the biological application of optical transfection, gene knockdown experiments were performed on TRex-willin-GFP-HEK cell line to silence the gene, willin with an siRNA. A specific and targeted successful knockdown was demonstrated with the absence of green fluorescence on the transfected cells. More cells were knock down compared to transfected with DNA, showing a size-dependence efficiency which maybe due to diffusion difference, as well as, the biological barriers that plasmid DNA has to go through prior expression as discussed in Chapter 2.

In addition, based on the parameters obtained for transfection, the mechanism for membrane permeability changes using the violet diode laser was elucidated by calculating the change in temperature at the focus. The parameters are significantly lower compared to published reports using pulsed fs and ns laser sources, hence, membrane disruption based on plasma formation can be disregarded as the mechanism for cell transfection using this laser source. Based on Chapter 3, the two dominant mechanisms at these laser parameters and exposure time are photothermal and photochemical. The temperature calculations using the parameters used for cell transfection were performed by obtaining the absorption coefficient of a phenol red sphere using Mie scattering theory. Based on this temperature calculation, which showed that the change in temperature is not enough to induce changes in membrane fluidity, I proposed an ROS-mediated effect that impairs the membrane and allows DNA plasmid to enter the cytosol.

Hence, further experiments will be required to understand the exact mechanism for poration events caused by violet diode laser light. This may entail measuring ROS level using cell permeant fluorecarboxy-H_2DCFDA, which is sensitive to changes in concentration of the radical, hydrogen peroxide. To detect the presence of ROS levels, the fluorescence level must be monitored during the irradiation requiring fast and sensitive imaging system. Furthermore, fast response probes can be utilised to detect changes in membrane potential or Ca^{2+} gradients during cell poration which can be related to the viability and membrane permeability. This would allow one to detect biochemical perturbation on the cell with the localised exposure to the violet laser.

Advance application of the technique can be demonstrated with its capability to transfect cell lines such as post-mitotic neurons or quiescent cells which are difficult to transfect using conventional chemical based transfection. Initial work has been performed on optical transfection and optoinjection of exogenous materials into mammary epithelial cells, MCF10-A, using a violet diode laser. These cell lines can be efficiently transfected only by retroviral means. Up to 30% transfection efficiency of Mito-DsRed plasmid was achieved on this cell line. Further work is necessary in order to optimise the parameters for each cell line in order to demonstrate the capability of the technique to transfect a variety of samples in an *in vitro* culture.

The advantages of using a violet diode laser for optical transfection is two-fold. Firstly, it is inexpensive compared to fs and ns systems which are more commonly employed for optical transfection. Secondly, it is portable and both the laser and optics can be engineered within a small box that can be retrofitted in any microscope system. Demonstrating cell transfection using this laser is an essential step towards commercialisation allowing biology laboratories to access the technology for future significant single-cell transfection experiments.

In the following chapter, I will discuss the developments on optical injection and transfection technique using an NIR fs laser. A versatile and reconfigurable SLM incorporated in the system which addresses the crucial requirement for targeting and precise pore formation on the membrane using this laser. Furthermore, I will present our results on enhanced optoinjection and transfection by employing different targeting modalities.

Part of this work was published in Journal of Biomedical Optics,**15**, 2010 [130].

5

Femtosecond (fs) holographic system for optical injection and cell transfection

A spatial light modulator is a versatile diffractive optical element for beam steering via wavefront modulation. This chapter demonstrates an implementation of spatial light modulator on an NIR fs optical transfection system for enhanced optoinjection and transfection. In this work, different modalities of poration are presented providing control over dosage with "point and shoot" capability providing a user-friendly device for optoinjection and cell transfection.

5.1 Introduction

In the previous chapter, transient transfection was demonstrated using a CW violet diode laser. However, with increasing advancement in engineering of laser designs especially for pulsed laser sources, ultra-short NIR fs lasers became more mature systems for optical transfection. In this technique, a tightly focused NIR fs laser irradiates a femtolitre volume of the cellular membrane producing a site-specific transient opening on the membrane allowing genetic materials to enter the cell [25, 26]. Targeted single cell fs-based optical transfection has been unrivalled in terms of

its post-treatment viability and efficiency. Transfection efficiencies up to 80% and cellular viability as high as 90% have been achieved using this technique [16].

The use of a fs pulsed NIR has been a popular choice for most optical cell transfection applications due to its localised irradiation leading to precise ablation and significantly low toxicity. A Ti:sapphire laser operating at a wavelength of 800 nm and pulse duration of $\approx$ 100 fs is often employed creating a sub-micron pore generated by multiphoton absorption. The highly localised technique has been applied not only to conventional cell lines but also to a variety of biological systems. Fs pulsed NIR laser has been used to optically transfect undifferentiated stem cells [18]. It has been applied to challenging transfection experiments such as localised delivery of a transcription factor Elk1 mRNA into the soma or the dendrites of rat hippocampal neurons [17]. Irradiation of fs pulses *in vivo* to mouse tibia muscle enabled prolonged gene expression with minimal toxicity [143]. Furthermore, a zebrafish embryo enclosed in a chorion can be optically transfected without apparent damage to the developed larva [120].

However, for the system to be a consistent and reliable cell transfection tool, several challenges are yet to be overcome. As the technique relies on multiphoton absorption, as described in Chapter 3, it requires precise alignment of the laser focal beam to the membrane. Very small axial misalignment can lead to a decrease in efficiency of up to 30% [144]. Hence, a NIR fs Bessel beam (BB) generated with an axicon lens is used for cell transfection [144]. Bessel beams are non-diffracting modes of light which can be visualised as an optical syringe, extending the range at which multiphoton absorption could occur. Endoscopic applications are envisaged by fabricating a micro-axicon at the tip of an optical fibre [145] as well as an integrated system consisting of a lens fibre and microfluidic delivery for poration [146] which may progress *in vivo* optical transfection in living animals.

Improvement of the engineering and design of laser-mediated drug and gene delivery methods will enable the technology to be accessible and transferred to advanced molecular and biology research laboratories. Further advancement towards easy to use systems that does not necessitate an experienced experimentalist would lead to their wider application and commercialisation. Hence, in this chapter, a **fs holographic system** was developed employing a fs system for high-throughput and user friendly optical transfection and injection. A spatial light modulator (SLM) was integrated into an fs optical transfection system that permits "point and shoot" targeting, providing full control over the lateral and axial positioning of the beam. This enhances the accuracy of targeting which is an important step towards the laser treatment of large number of adherent cells. In addition, enhanced optoinjection and optical transfection was demonstrated with varying targeting modalities.

In combination with a piezo-driven scanning mirror, the laser could be deflected over a wider 140 μm field of view which permits dosing of multiple cells at a time. In the future, the aim of this work is to build the same system using a violet diode laser. However, at present, higher efficiency for commercially available SLM can be obtained for wavelengths in the NIR.

The work presented in this chapter was performed in collaboration with Dr. Maciej Antkowiak (SULSA Technologist, University of St. Andrews). The experimental setup was designed and aligned by both the author and Dr. Maciej Antkowiak. The controlling software was authored by Dr. Maciej Antkowiak. A LabView program authored by Dr. T*ô*mas Ci*ẑ*m*á*r (Medical Research Fellow, University of St. Andrews) was used to correct for aberrations. The author performed all the cell work, contributed significantly in developing the protocol for optoinjection and performed the optical transfection experiments presented in this chapter.

5.2 Optical beam steering using a spatial light modulator

Beam steering of the focal spot in a field of view is advantageous for optical manipulation techniques. In optical trapping, the focal spot position can be laterally translated with the use of a mirror situated at the conjugate plane of the back-aperture of the objective. The displacement of the focal beam is related to the reflection angle of the mirror. In more advanced systems, either a galvo or piezo mirror is incorporated to the system, providing fast lateral control of the focal beam. In a scanning configuration, galvanometer (galvo) mirrors with feedback loop can rapidly translate the beam up to 2 kHz. Alternatively, piezo mirrors which have slower milli-seconds reconfiguration times but are superior in "step and hold" positioning applications wherein the beam is desired to be fixed in a precise location for a certain period. In other applications, acousto-optical deflectors (AOD) have been implemented for fast MHz scanning rate for time-shared beam multiplexing.

However, applications such as optical transfection and optoinjection, not only require lateral displacement of the focal beam but also precise axial positioning. For galvo, piezo and AOD systems, if an axial displacement of the focal spot is required, an additional lens is needed or the objective itself, has to be translated which significantly slows down the process and allows time-shared beam multiplexing in one plane only. A much faster and more flexible two- or three dimensional positioning of multiple foci was achieved using a configuration of four AOD [147]. However this was obtained at a price of a significant increase in pulse duration from 200 fs to 1.8 ps, which is detrimental to the multiphoton efficiency of the system.

On the other hand, an SLM in a Fourier configuration can provide flexible and fast lateral and axial positioning of the beam in the sample plane. Hence, wavefront modulation in the Fourier space provides an advantage over other beam steering techniques as it can provide beam steering, axial control and beam shaping all at the same time. This permits full three dimensional control on the focal spot at the sample plane providing user-control and flexibility over the desired experimental parameters.

5.2.1 Optically-addressed parallel aligned spatial light modulator

A liquid crystal (LC) spatial light modulator (SLM) is a versatile tool for dynamic wavefront modulation. An SLM can be visualised as a 2-dimensional periodic pixel array with LC components sandwiched in between two conducting plates. Nematic LC can be distinguished from other types of LC used in SLM as they have parallel molecules throughout the LC cell with randomly located centres [148]. The LC cell thickness is adjusted based on the incident light wavelength. Each pixel in the LC-SLM can be electronically or optically addressed thereby allowing modulation of the phase of an incident beam. In electronically addressed SLM, a localised and defined voltage is applied to the LC layer. In this configuration, the molecules of the LC align themselves in response to the voltage which modulates their characteristics [149]. Meanwhile, an optically addressed SLM utilises a laser diode module for writing and an amorphous silicon layer which reads the write light intensity. The write light changes the impedance of the amorphous silicon layer and subsequently applies a voltage change on the LC layer [150]. A computer generated hologram (CGH) determines the information to be encoded to the write light. The bitmap of a CGH is an image made up of an 8-bit per pixel in grey scale wherein zero value (black) represents zero phase and 255 (white) represents a phase of 2π. Table 5.1 shows the specification of the optically addressed parallel aligned (PAL)-SLM utilised in this chapter.

Properties	Hamamatsu PPM X8267-13
Number of pixels	$\approx$ 590,000 pixels
Effective image area	20×20 mm
Phase modulation level	more than 2π radian
Maximum spatial display resolution	19 lp/mm
Wavelength	700–800 nm

Table 5.1: Specifications of the optically addressed PAL-SLM (Hamamatsu, PPM X8267-13) utilised in the fs holographic system.

5.2.2 Computer generated hologram for beam steering

To calculate the CGH to be displayed in the SLM for optical beam steering, the fastest way is to obtain the linear superposition of the desired beams using phases corresponding to prisms and lenses. This simple approach of superposing prisms and lenses gives full control over the three dimensional positioning of the focal spot. Let us consider ζ,η and x, y to be the transverse coordinates of the SLM and the imaging plane respectively. The appropriate wavefront modulation corresponding to lateral translation of the focused spot can be obtained by calculating the CGH for a linear blazed diffraction grating given by the equation [151]

$$\phi(\zeta,\eta) = \left(\frac{2\pi}{\Lambda_x}\zeta + \frac{2\pi}{\Lambda_y}\eta\right) mod 2\pi \tag{5.1}$$

where Λ_x= $\lambda f/\Delta x$ and Λ_y= $\lambda f/\Delta y$ are the period of the grating in the x and y, Δx and Δy are the desired translation in x and y respectively while λ is the wavelength of light and f is the focal length of the lenses and objectives used.

On the other hand, if the desired focus spot is intended to be located a distance Δz away from its original position, adding a quadratic phase which mimics a Fresnel lens can shift the focus spot up and down parallel to its optical axis [151] as written in the following equation.

$$\phi(\zeta,\eta) = \left(\frac{\pi\Delta z}{\lambda f^2}(\zeta^2+\eta^2)\right) mod 2\pi \tag{5.2}$$

The phase corresponding to both lateral position and focal spot translation is given by the sum of Eq. 5.1 and Eq. 5.2 written as,

$$\phi(\zeta,\eta) = \left(\frac{2\pi}{\Lambda_x}\zeta + \frac{2\pi}{\Lambda_y}\eta + \frac{\pi\Delta z}{\lambda f^2}(\zeta^2+\eta^2)\right) mod 2\pi \tag{5.3}$$

Hence, the creation of multiple spots with arbitrary position and power is possible by summing up the individual complex functions, $e^{i\phi_j(\zeta,\eta)}$ and calculating the argument of the sum of the complex functions, $\phi_{total}(\zeta,\eta)$ given by the following expression,

$$\phi_{total}(\zeta,\eta) = arg\left(\sum_j e^{i\phi_j(\zeta,\eta)}\right) \tag{5.4}$$

An example of CGH used for the experiment are shown in Fig. 5.1 (A–C). Fig. 5.1 (A) shows the CGH to laterally displace the spot in x,y. Fig. 5.1 (B) is the CGH to displace the focus along the axial direction. The corresponding CGH to be displayed in the SLM to both translate and axially displace the focal spot is the

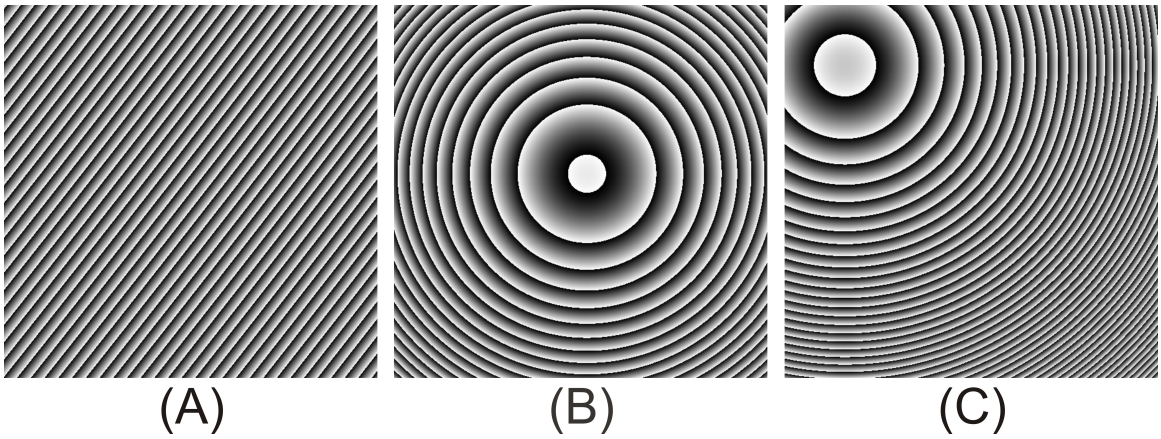

Figure 5.1: Example of computer generated holograms to (A) laterally translate the beam along the x,y, (B) displace the focus along the axial direction (C) and combination of lateral translation and displacement of the focus.

sum of Fig. 5.1 (A) and (B), shown in Fig. 5.1 (C). For our purposes, the amplitude variation was neglected. This results in the creation of ghost images and higher order diffraction orders [152]. Hence, a slit is positioned at the intermediate plane after the SLM as shown in Figure 5.2 to block the zeroth order and the ghost images allowing only the modulated spot (1st order diffraction) to pass through the rest of the optical train.

There are several pre-existing algorithms that had been utilised to create multiple optical traps such as iterative schemes based on Gerchberg-Saxton and adaptive additive algorithms which improves the hologram performance albeit the increase in computational cost. However, for the purposes of the fs holographic system, the linear superposition method is adequate for the desired application.

5.3 Experimental Design

The fs holographic system consists of two components, (1) a fs holographic poration system capable of fast lateral and axial positioning of the beam for enhanced optoinjection and cell transfection and (2) a microscopy system capable of brightfield, epifluorescence, phase contrast, differential interference microscopy and time-lapse imaging. The experimental design is shown in Figure 5.2. The system is built around a Nikon TE-2000 inverted microscope. An additional scanning head can also be utilised for confocal imaging. The poration beam is from a Ti:sapphire fs laser (Coherent Mira 900 pumped by Verdi-V5) with wavelength centred at 800 nm,

pulse width of approximately 180 fs and 80 MHz repetition rate directed to the upper fluorescence turret of the microscope.

The laser passes through a polarising beam splitter (PBS) and half-wave plate ($\lambda/2$) for power attenuation. An electronic shutter triggered through a data acquisition (DAQ) card controls the exposure of the laser on the sample. The beam is first expanded and collimated by a pair of lenses (L1 and L2) with focal lengths of f_1= 50 mm and f_2= 1000 mm respectively. With a series of mirrors with reflection coatings specific for 800 nm, the beam is directed into a SLM (Hamamatsu PPM X8267-13) with 768 by 768 control pixels. The beam expansion served two purposes, firstly, to overfill the 20 × 20 mm active area of the SLM and secondly, distribute the power of the beam over a larger area which avoids damaging the liquid crystal. The incident angle of the laser beam to the SLM is kept at less than 10 degrees to maintain phase modulation linearity. A half-wave plate ($\lambda/2$) before the telescope rotated the polarisation of the laser to maximise the power diffracted into the first order.

The beam is demagnified by a pair of lenses L3 and L4 with focal lengths f_3= 500 mm and f_4= 200 mm. A demagnification factor of ×2.5 is chosen to just slightly overfill the backaperture of the microscope objective (Nikon, 0.8 NA) and achieve a diffraction limited spot. L5 (f_5= 200mm) and L6 (f_6= 200 mm) relays the image on the SLM to the backaperture of the objective. The transmission of the microscope objective is measured to be 66±1% by a dual objective method. A slit is positioned at the focal plane of L3 (intermediate plane) to block the unmodulated zeroth order and ghost spots shown in Fig. 5.3 (A). However, blocking the zero and negative orders limits the available targeting field of view to half (70 μm) as shown in Fig. 5.3 (B).

5.3.1 Aberration correction

Optical aberrations are present in any optical system which degrade its imaging capabilities leading to blurring of images. The aberration in an optical system prevents the beam from focusing to its ideal diffraction-limited spot, leading to spreading of its beam profile. Hence, in optical transfection systems, aberrations decrease the power density at the focus and the efficiency for multiphoton absorption affecting the efficiency of poration. Furthermore, with a reflective type SLM, such as the one utilised for this experiment, its slight nonunformity causes significant aberration to the input light beam [148]. However, an advantage of incorporating an SLM is it can correct for the summative aberration in the optical system by displaying a corrective CGH on the SLM. Fig. 5.4(A) illustrates the CGH imposed on the SLM for aberration correction. In the fs holographic system, a technique

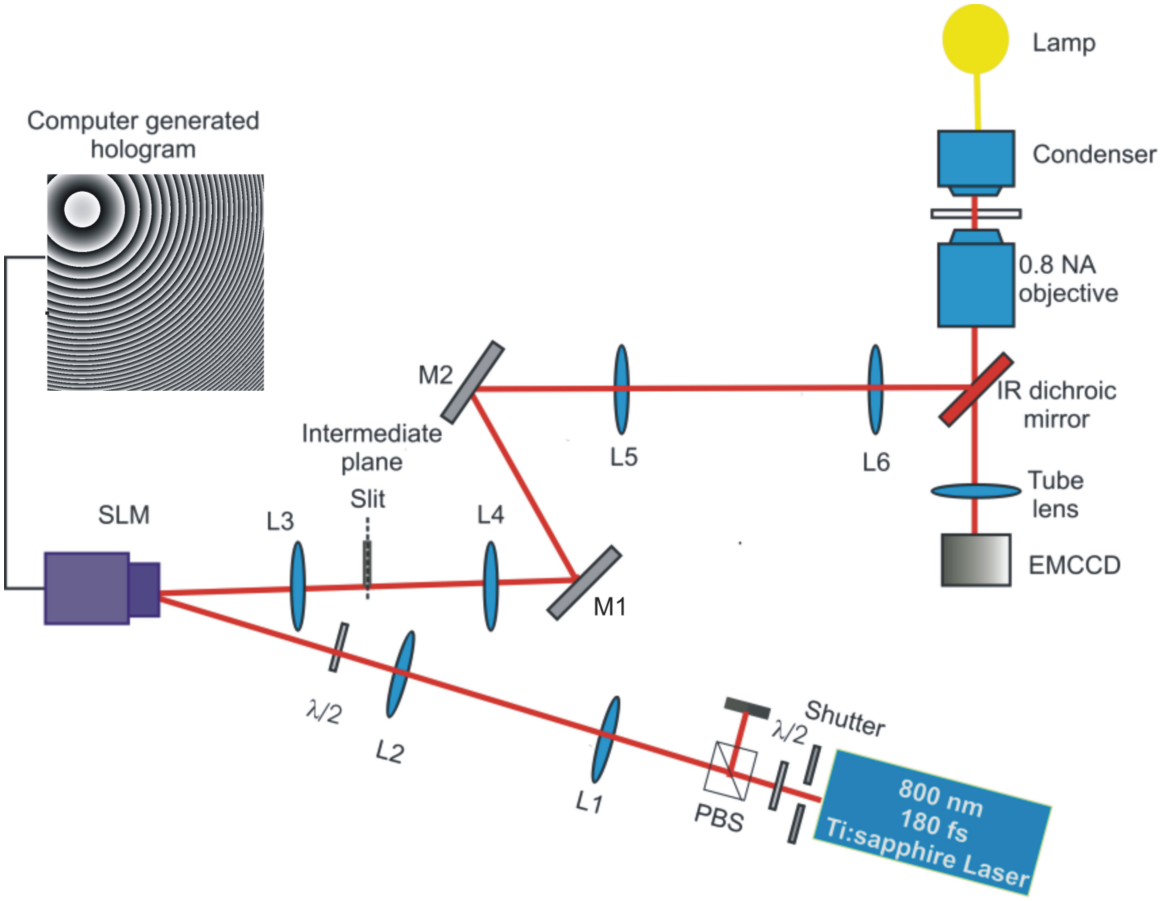

Figure 5.2: Schematic diagram of the fs holographic system for targeted and accurate fs cell transfection. L-lenses; M-mirrors; PBS-polarising beam splitter; $\lambda/2$- half wave plate; SLM-spatial light modulator. The fs laser beam is expanded by a telescope system (L1 and L2) passing through an electronic shutter. The beam is directed to an SLM which is used for beam steering and additional wavefront modulation to control the axial position of the laser beam. A dichroic mirror deflects the fs laser to the back aperture of a 0.8 NA, 60× Nikon, microscope objective. Imaging is performed using an EMCCD camera. L1 and L2 with focal lengths f_1= 50 mm and f_2= 1000 mm respectively expands the beam to fill the active area of the SLM. L3 (f_3= 500 mm) and L4 (f_4= 200 mm) demagnifies the beam to ensure that the backaperture is overfilled. L5 (f_5= 200 mm) and L6 (f_6= 200 mm) relays the image on the SLM to the backaperture of the objective.

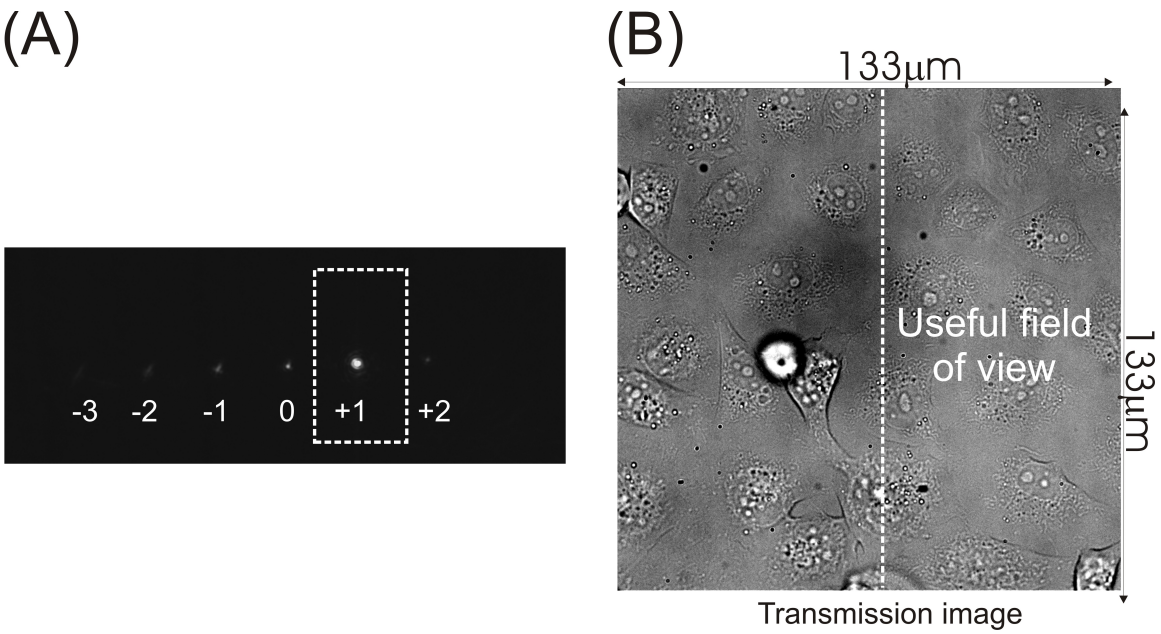

Figure 5.3: (A) Diffraction orders obtained upon imposing a blazed CGH on the SLM. The 1^{st} order diffraction was used for cell transfection and optoinjection. (B) An image showing the full field of view using 60× objective and the useful field of view due to the necessary blocking of other diffraction orders.

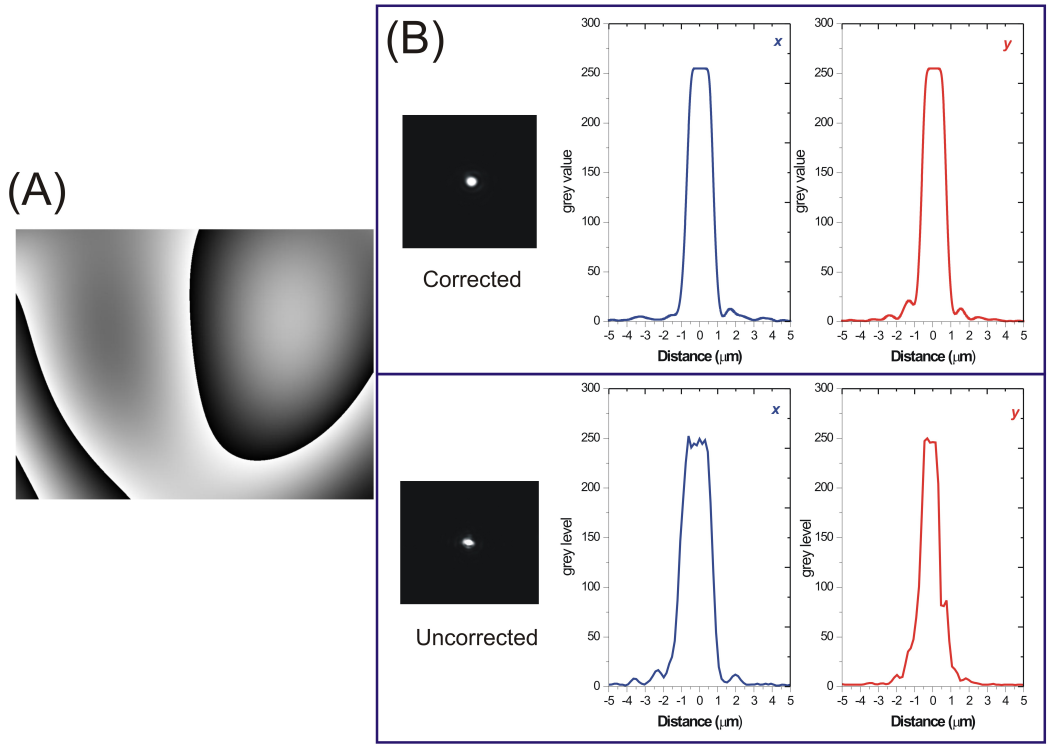

Figure 5.4: (A) The CGH imposed on the SLM to correct the aberrations of the laser beam. The laser beam was corrected by visual inspection of the image of the focused beam while simultaneously adjusting the Zernike polynomial coefficients thereby changing the CGH imposed on the SLM to achieve a symmetrical beam profile. (B) TOP and BOTTOM - Image of corrected and uncorrected beam respectively and their corresponding x and y intensity profile.

based on the expansion of the wavefront on a circular pupil in Zernike polynomials is utilised. The first six radial orders (24 modes) correspond to the most significant aberrations such as astigmatism, coma and spherical aberration. The individual polynomial coefficients can be adjusted accordingly, changing the CGH displayed on the SLM in order to correct for the aberrations of the laser beam. By visual inspection and subsequent adjustment of the polynomial coefficients, a symmetrical focus laser spot can be obtained. Bottom image in Fig.5.4(B) shows the uncorrected beam which exhibits intense astigmatism, coma and spherical aberrations. Coma and spherical aberrations are observable when the beam is defocused. The top image shows the corrected beam. When the corrective CGH (Fig. 5.4(A)) was encoded in the SLM, a circularly symmetrical beam profile was obtained.

5.3.2 Calibration characteristics

Based on previous independent investigations, the efficiency of poration is dependent on the power at the focal spot [26]. As discussed in Subsection 5.2.2, lateral positioning can be achieved by imposing a blazed linear grating CGH, where the period of the grating is inversely proportional to the desired translation. However, the modulation efficiency of the SLM is also dependent on the period of the phase impose on it. With decreasing period on the blazed phase, the efficiency to the translated beam decreases and more power is directed to the unmodulated zeroth order. For consistency, it is crucial to calibrate the power of the translated beam as a function of its position over the available field of view. Hence, the power at the sample plane was characterised as a function of the position of the translated beam relative to the zeroth order beam in the field of view.

The laser power was measured using a high peak power thermopile sensor (Coherent, PM10V1) with a digital readout (Coherent, FieldMaxII-TO). Using a LabView program, the CGH was changed incrementally to deflect the beam to a given x and y position and subsequently the power was measured at this position. Since the zeroth order and the other diffraction orders were blocked, they have negligible contributions to the power delivered to the sample plane and only the first order diffracted beam was measured. Figure 5.5(a) shows the experimentally measured efficiency of the first order diffraction at different positions in the sample plane. The diffraction efficiency of the translated beam dramatically decreases with its lateral displacement from the zeroth order. Furthermore, at 50 μm away from the position of the zeroth order, the corresponding normalised power efficiency left at the translated beam is only 0.2.

In order to achieve a uniform power over the field of view, a coefficient factor A is imposed to control the fraction of power at the poration spot and the final form of the complex field will become [14]

$$M(\zeta,\eta) = Ae^{\frac{2\pi i}{\lambda f}(\zeta\Delta x+\eta\Delta y)}e^{\frac{-\pi i\Delta z}{\lambda f^2}(\zeta^2+\eta^2)} + (1-A)e^{\frac{2\pi i}{\lambda f}(\zeta\Delta x_0+\eta\Delta y_0)} \tag{5.5}$$

The first part of the Eq. 5.5 refers to the modulated 1st order beam used for optoinjection and optical transfection while the second part indicates the unwanted fraction of light. Since the SLM only modulates the phase, unwanted ghost spots will be created. This is minimised by positioning the unwanted fraction of light vertically above the zeroth order. With a slit in place to block the ghost spots and the zeroth order, the unwanted amount of light is kept at a minimum. Furthermore, to ensure a precise power control, the power left at the poration spot was experimentally measured as a function of the coefficient A at various points within the field of view shown in Figure 5.5(b). It was found that the power for poration at a specific value

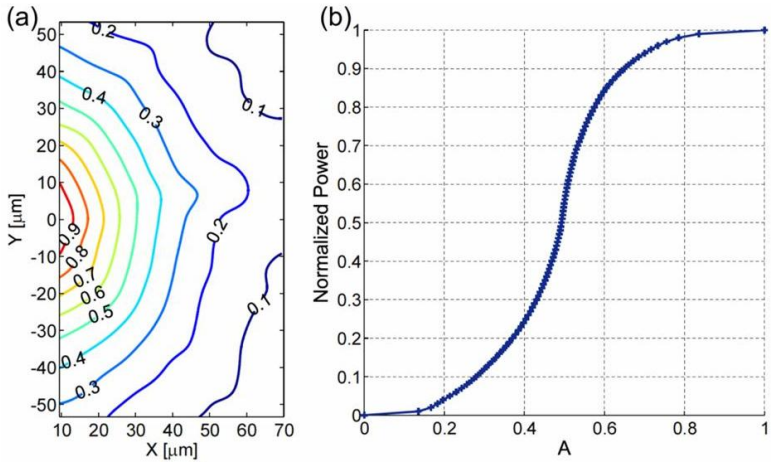

Figure 5.5: Calibration characteristics of (a) diffraction efficiency of the SLM and the distance of the first order from the zeroth order measured by placing a thermopile sensor at the sample plane to measure the power at the first order as a function of position in the field of view. Image in (b) shows the fraction of total power left in the poration spot as a function of coefficient A in Eq. 5.5 [14].

of A does not vary more than 1–2%.

5.3.3 Controlling software and camera

The system is controlled by a custom-made LabView 8.5 (National Instruments) software providing user control over the mode of poration, shutter duration, number of doses and camera settings. Image is acquired using an Electron Multiplying Charge Coupled Device (EMCCD, Andor iXon+). An EMCCD differs to normal CCD camera due to an additional Electron Multiplying register (EM) allowing weak signals to be multiplied before any readout noise is added by the output amplifier [153].

The EMCCD camera allows us to detect very faint signals often observed in optoinjection experiments with propidium iodide. An EM gain of 5 is used with 1 s exposure setting of the camera to capture the raw images of the optoinjection experiments. In order to reduce any background noise, the camera is cooled down to -75^{o}C to minimise the presence of dark current. The CGH displayed on the SLM is an 8-bit grey-scale bitmap image. By pointing the mouse on the screen and the software registering the pixel position in x and y, the program correspondingly calculate the CGH to deflect the beam at this position which allows "point and shoot" in any position in the field of view with single pixel precision, providing a targeting accuracy of 133 nm using a $\times$60 objective. The electronic shutter is

triggered through a DAQ card wherein the shutter duration and the delay between shutter exposure can be controlled for multiple laser exposure configuration.

5.3.4 Sample preparation for optoinjection experiments

CHO-K1 and HEK293 cells were utilised for this experiment. Cell culture methods are discussed in Appendix. For the fluorophore optoinjection experiments, the cell monolayer was washed twice with 1 mL OptiMEM (Invitrogen) before addition of 3 μM of Propidium iodide (PI, Invitrogen) in OptiMEM to the cells. The fluorescent signal from PI was captured, 5 min after irradiation. Afterwards, cells were washed twice with 1 mL of OptiMEM and fresh medium was added before incubating the cells for at least 90 min.

Prior to fluorescence imaging for cell viability, cells were washed twice with 1 mL of Hanks' Balanced Salt Solution (HBSS, Sigma). After which, 2 μM of Calcein AM (CAM, Invitrogen) in HBSS solution was added prior incubation for 15 min. The non-fluorescent CAM is cell membrane permeant and is converted to green fluorescent Calcein after hydrolysis of intracellular cell esterases. Once inside, it is retained by the cells that have perfectly intact plasma membranes. However, in damaged or dead cells both unhydrolysed and fluorescent products immediately leak out of the cell with little or no esterase activity. Healthy cells have a characteristically bright green fluorescence while minimal or punctate signal is indicative of cell death or compromised viability. All experiments were performed at 37 ^{o}C. The DNA transfection efficiency was calculated as the number of fluorescent cells after 48 h over the number of irradiated cells.

5.4 Experimental Results

5.4.1 Different modalities of optoinjection

Independent studies on fs optical transfection reported the dependence of the efficiency of the technique on the combination of laser parameters, pulse energy and exposure time [26, 27] but few studies had been conducted on the effect of accurate positioning of the focus spot with respect to the cell membrane. The common practice for fs optical transfection [26, 18] is that the laser beam's position (x,y) and it's focal position(z) is fixed at the sample plane. By using a micrometer precision, xyz translation stage, each cell is positioned spatially with respect to the beam. With this practice, the lateral positioning could be accurate enough as the focal beam spot (≈ 1.2 μm) is one-order magnitude smaller than the size of the cell. However, the axial positioning may not be as accurate to precisely target the cell

membrane (thickness of ≈ 5 nm) and not damage any of the intracellular cytosolic compartments within the cell.

Moving the cell axially with respect to the focus of the laser by defocusing and refocusing the image of the cell allows the operator to determine approximately the location of the membrane. At certain laser threshold intensity, a visible gas bubble is obtained in response to the laser when the focal spot hits the membrane. By looking for this adverse response from the cell, one could approximate where the membrane is with respect to the focus spot. However, because of the variation in cell's thickness and degree of curvature, this varies from cell to cell, leading to inconsistencies on the positioning of laser focus with respect to the cell membrane.

It has been shown that the Bessel beam (BB), with its characteristic nondiffracting syringe of light, can improve the transfection efficiency over a longer range of axial positioning [144]. Previously, an SLM system enabled beam steering and multiplexing of a BB [154]. However, as the creation of BB results to concentric rings which do not contribute to multiphoton absorption [144] and the phase modulation in the SLM results in a significantly loss in power due to limited diffraction efficiency, incorporating a BB to the system imposes a limitation to the available power at the sample.

Another solution is to introduce a controlled sequential dosage at different spatial and axial positions within the cell. Computer control of both the SLM and the shutter provides precise delivery of sequential fs pulses. The improvement of the controlled sequential dosage on cell membrane poration is tested by optoinjection of freely diffusing fluorescing dye, PI. The delivery of the dye provides a more direct confirmation that an opening in the membrane has been made allowing small molecules to enter the cell. PI was chosen due to its small size (668.4 Da) and provides a distinct fluorescence signal when the dye has intercalated with the DNA and mRNA within the cell. For both drug and gene delivery, the viability of the cell after treatment is a primary concern for such applications. Hence, CAM was added 90 min after poration to determine the percentage of viably optoinjected cells.

Hence, different targeting modalities in poration were implemented using the fs holographic system. Laser parameters used were laser power (P) = 70 mW and exposure time (T) = 40 ms. These parameters were chosen based on prior experiments allowing successful optoinjection and similar parameters employed in independent studies [27]. The beam focus was positioned 7 μm above the bottom substrate of the dish wherein repeatedly a visible gas bubble was obtained for CHO-K1 cells. Each dose is given 700 ms apart which did not lead to cumulative effects.

Fig. 5.6 shows typical images acquired during the experiment. As shown in Fig. 5.6(a), cells that became necrotic after optoinjection obtained a very intense PI

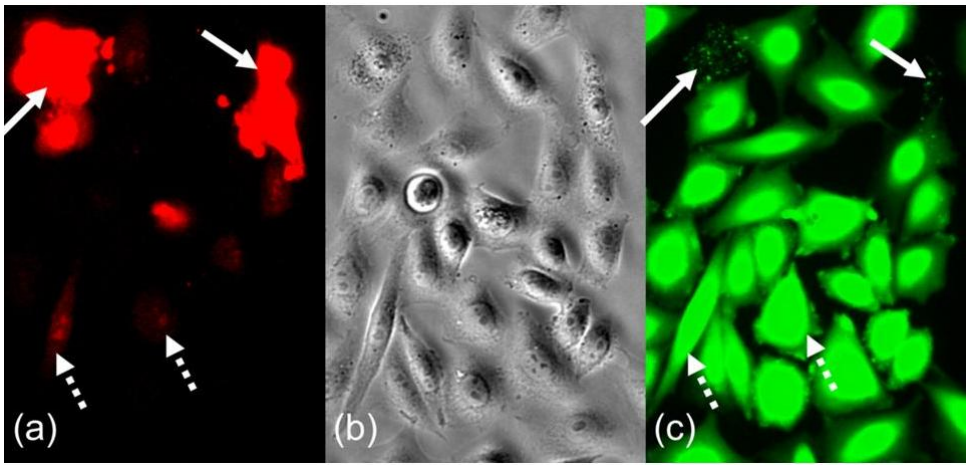

Figure 5.6: Images acquired during optoinjection efficiency and viability experiments. (a) PI signal 5 min after irradiation, (b) phase contrast image of the field of view (c) CAM fluorescence image 90 min after irradiation. The necrotic cells are pointed out by solid arrows and the viable cells are pointed out by dashed arrows [14].

signal in the nucleus (solid arrows). Meanwhile, successfully optoinjected cells that remained viable have a weak but almost uniform fluorescence in the cytoplasm (broken arrows). Notably, necrotic cells (see Fig. 5.6(b)), have distinct granular features on the cytoplasm and the outline of the nucleus is clearly visible. CAM fluorescence image (see Fig. 5.6(c)) confirmed that these cells are necrotic, as they have either punctate or absent CAM signal which implies compromised cell viability due to the lack of esterase activity. On the other hand, optoinjected cells with uniform PI signal on its cytoplasm have very bright CAM signal which signifies that the treated cell is both optoinjected and viable.

In this experiment, three types of targeting were implemented for cell optoinjection: "single" dose on a single axial and lateral position on the cell, "triple axial" providing three sequential doses on separate axial planes 1 μm apart and "triple lateral" which allows three sequential doses on separate lateral positions, 2 μm apart forming an equilateral targeted dosage points. Triple axial allows dosing of three individual axial positions in the cell membrane. In this experiment, dosing with this configuration leads to a single visible gas bubble located at the second dose which corresponds to the membrane. On the other hand, triple lateral leads to two or three individual visible gas bubbles which often lead to abrupt cell necrosis and its lysis.

The percentage of optoinjected, viably optoinjected and viable was determined within all the irradiated cells for the three different modalities of poration using

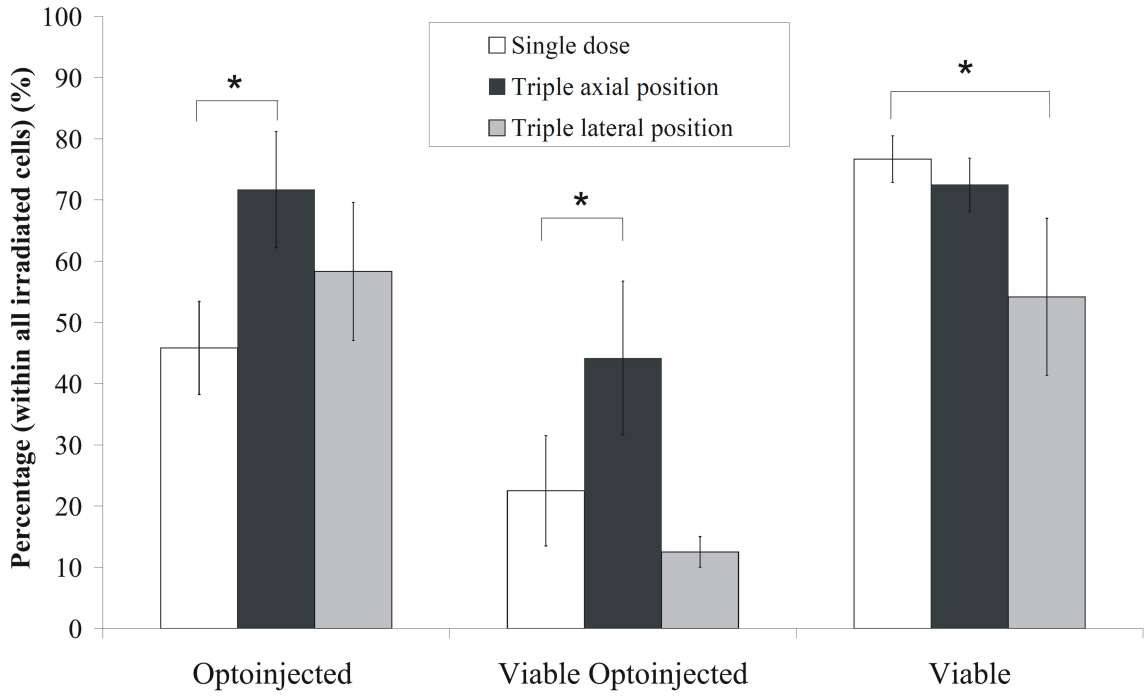

Figure 5.7: Optoinjection efficiency using different modalities of dosage, single, triple axial and triple lateral dose. Error bars represent the standard error of the mean with n=3 experiments with 40 dosed cells,*—significant data sets in unpaired two tailed t-test($p< 0.05$) [14].

.

P= 70 mW and T= 40 ms was obtained. Each data point comprised of n= 3 experiments each with 40 dosed cells. Fig. 5.7 shows the percentage of optoinjected, viable and viably optoinjected cells after treatment. Triple axial dose provided the best performance as it allowed 40% viable optoinjection and 72% successful injection of cells. This showed a marked improvement in optoinjection efficiency compared to 45% obtained for a single dose. Hence, enhance precise targeting of the membrane is crucial to achieve successful optoinjection. Meanwhile, although the dosage using triple lateral provided an improvement over the single dose on optoinjection efficiency, the generation of multiple gas bubbles on the membrane led to compromised cell viability at this laser parameter leading to lowest viable optoinjection efficiency percentage of less than 20%.

The poration effects *via* laser-material interaction are due to the expansion and collapse of short-lived cavitation bubbles produced within a couple of microseconds after irradiation [97]. At sufficiently high laser intensity, long lasting residual gas

bubbles lasting from milliseconds to seconds are visible using brightfield imaging. It is conjectured that they arise due to dissociation of biomolecules into volatile and non-condensable fragments [97]. In this study, optoinjection in the absence of visible gas bubbles was not observed similar to observations by independent studies [27]. However, the presence of gas bubbles did not always guarantee a successful optoinjection. For example in Fig. 5.7 wherein triple axial dose led to 90% of the cells with gas bubble, among the treated cells, only 70% actually showed successful optoinjection.

5.4.2 Optical transfection with the fs holographic system

The attractiveness of the technology stems not only from viable delivery of molecules but also to perform genetic modification *via* optical transfection. Similar to the optoinjection experiments, the transfection efficiency was determined as a function of the different targeting modalities presented. Optical transfection experiments were conducted on CHO-K1 and HEK293 cells using the different modalities of poration. For single, triple axial, triple lateral and untargeted raster scan, the laser parameters used were P= 60 mW and T= 40 ms. This combination of parameters was proven to show successful cell transfection in previous independent studies [25, 26]. In contrast to optoinjection, for the parameters used for successful optical transfection, the presence of visible gas bubbles was not observed.

Successful transfection of Mito-DsRed plasmid into HEK293 cells was obtained for each modality of poration. A representative image of successfully transfected HEK293 cells is shown in Fig. 5.8(A). The transfection efficiency for various modes of poration for HEK293 cells is shown in Fig. 5.8(B) for n=4 samples each with 50–100 targeted cells. With a single dose on individual HEK293 cells, the transfection efficiency obtained was 34%. It was found that the increase in efficiency is not significantly different for single, triple axial and triple lateral. However, the plot shows an increase in the average transfection efficiency with increasing number of doses on the membrane. For example, compared to single dose, an increase in average transfection efficiency from 34% to 45% was obtained with triple lateral dose. Thus, multiple doses was further investigated to observe if it would enhance the transfection efficiency.

The delivery of 16 shots of fs pulses in a 4 × 4 pattern in a single axial plane (× 16 raster) was implemented at lower laser parameters, P = 30 mW and T = 40 ms compared to earlier targeting schemes. A lower laser parameter was chosen as increasing the number of doses would increase the total energy delivered to the sample which may induce cell necrosis. From Fig. 5.8(B), the 16 shots in a 4 × 4 pattern dosage within the cell's cytoplasm provided the highest transfection efficiency of

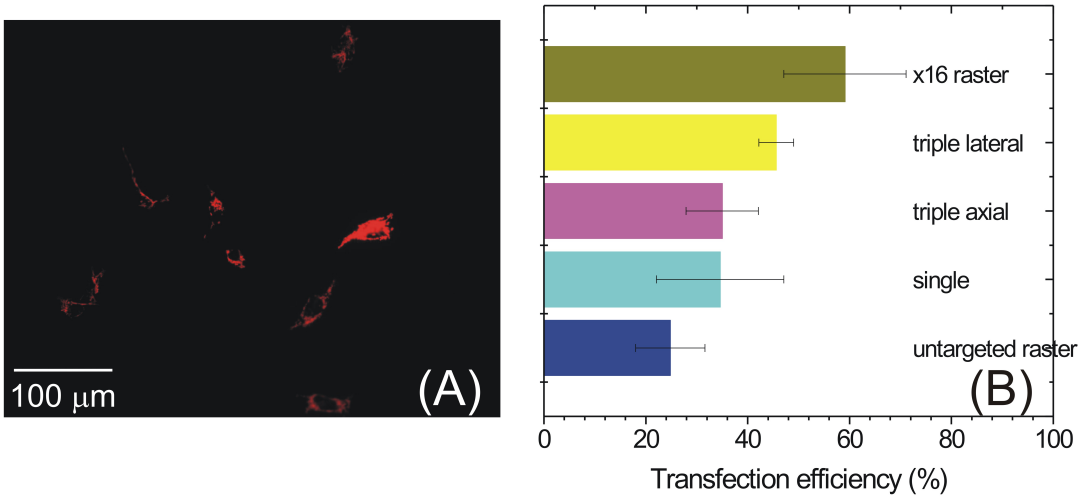

Figure 5.8: (A) Fluorescent image of HEK293 cells successfully transfected with a plasmid expressing Mito-DsRed. (B) Optical transfection efficiency of HEK293 cells for different modalities of poration. Laser parameters of P= 60 mW and T= 40 ms was employed for untargeted raster scan, single, triple axial and triple lateral. Laser parameters of P= 30 mW and T= 40 ms was used for ×16 raster (4 × 4 dosage) on the cell membrane. Each data is comprised of n=4 samples, with 50–100 dosed cells. Error bars represent ± standard deviation.

55% which was found to be significantly different from a single dose. In these experiments, lower laser power was not necessarily detrimental to the efficiency. Instead, increasing the number of laser shots to the cell membrane can compensate for lower P. Similarly, lower laser powers at 30–35 mW and even shorter exposure time 5 ms with 16 random shots was also employed in transfecting rat hippocampal neurons [17, 155]. The effectiveness of increasing laser doses at lower laser parameters can be understood in terms of enhanced number of poration sites where DNA material can enter, increasing the probability for transfection. Laser parameters on previous independent investigations on fs optical transfection utilised three doses of P= 50–100 mW and T= 16–40 ms [26, 144, 18] applied to a range of cell lines. These parameters are within the range where substantial heating already occurs on top of free-electron mediated chemical effects [97] which may affect the viability of the cell and reduce the efficiency of transfection.

Furthermore, the efficiency of the system was tested to provide unassisted and untargeted raster scan for high-throughput transfection. This is desirable for experiments requiring large number of transfected cells. In the presented SLM fs holo-

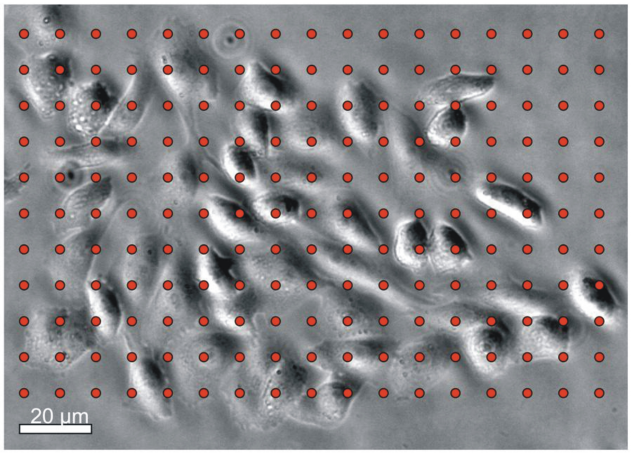

Figure 5.9: Schematic diagram of the raster scan irradiation wherein each point is set at 10 μm [14].

graphic system, the beam could be moved from spot to spot rather than scanning the beam along the sample in a continuous manner. In this configuration, length of laser exposure is precisely controlled which is crucial to the success of poration and maintaining cellular viability.

Based on the typical cell diameter of CHO-K1 which is 15–20 μm, the grid spacing was set at 10 μm (see Fig. 5.9). In a typical sub-confluent monolayer of CHO-K1 cells, 750 cells populate a substrate area of 1 mm^2. Hence, the time it requires to perform an unassisted raster scan of this area, considering an exposure time of 40 ms and a delay time of 50 ms to reconfigure the SLM corresponds to a total time of 900 s. Therefore, the throughput of the system can be estimated to be around 1 cell/second. Depending on the cell density on the sample dish, each cell could be dosed with the laser more than once. There are also instances when the fs laser is delivered to an empty space (see Fig. 5.8). With this configuration, the achievable DNA transfection efficiency of CHO-K1 and HEK293 cells is around 24% comparable to single dose with transfection efficiency of 34%. Alternatively, an automated targeted fs pulse delivery on each cell within a field of view could be performed with an appropriate image processing algorithm.

5.4.3 Selective co-transfection

Many studies in molecular biology require the expression of two or more unrelated genetic material in a two-step manner for protein functionality studies. Although,

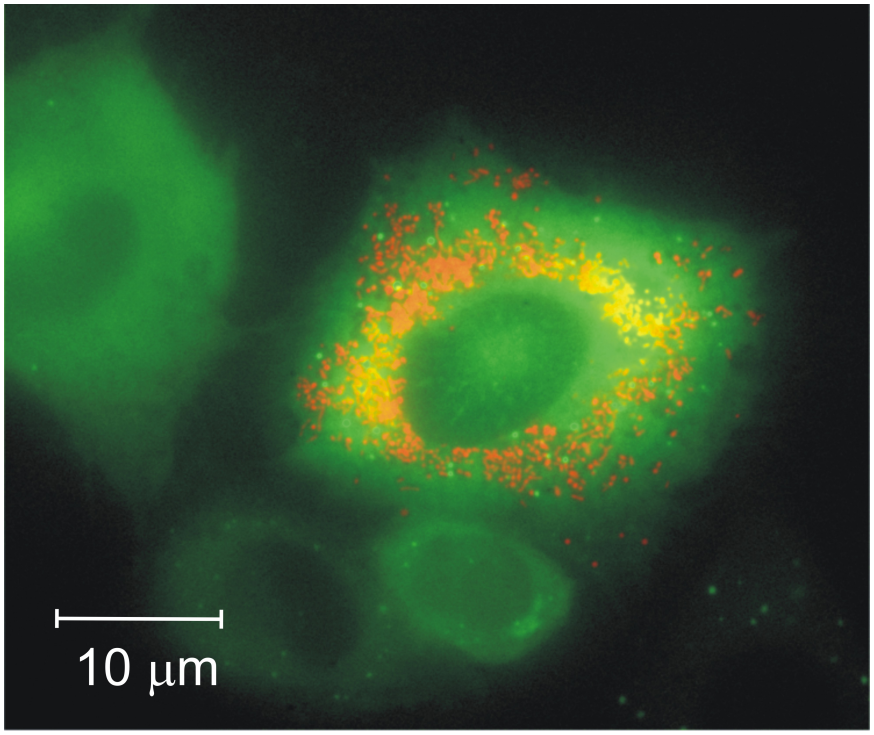

Figure 5.10: A green fluorescent protein (GFP) expressing CHO-K1 cell selectively phototransfected with a plasmid expressing Mito-DsRed [14].

co-transfection in one step is also possible, it is less efficient in maintaining high levels of expression for both proteins transfected within the cell. It is often better to transfect the cell with one gene at a time then screen for the cells with high level of expression. If the gene of interest is tagged with a fluorescent marker, epi-fluorescent imaging can aid in identifying already transfected cells to be targeted.

To demonstrate the capability of the system to perform selective co-transfection, CHO-K1 cells were chemically transfected with pCS2mt-GFP plasmid developed by Klymkowski and co-workers [156] using Lipofectamine 2000 (Invitrogen) according to manufacturer's specification. 24 h after chemical transfection, cells were washed twice with complete medium, after which, fresh complete medium was added before further incubation. A mixed population of fluorescing and non-fluorescing cells were obtained.

Cells expressing pCS2mt-GFP plasmid were observed by the characteristic expression of uniform fluorescence within the cell's cytoplasm and its absence from the nucleus. Epi-fluorescent imaging was performed using FITC HYQ Nikon filter cube (excitation: 460–500 nm, emission: 510–560 nm). 27 h after chemical transfection, fluorescence image was capture for the sample and individual cells that were

expressing GFP were transfected with Mito-DsRed plasmid which yielded a population of cells expressing both plasmids (see Fig. 5.10). This experiment opens up the possibility for a precise and selective, step by step transfection for treating cells based on earlier expression of a particular protein. For example, this technique maybe useful for differentiation of pluripotent stem cells into specialised cell types which may necessitate repeated and gradual transfection. Furthermore, the ability to track therapeutic transplanted single cells *in vivo* is an important aspect in stem cell biology [157]. The flexibility of single-cell optical transfection may allow targeting of earlier transfected cells *in vivo* and tracking them within a very dynamic microenvironment.

5.5 Fs holographic system combined with a piezo-driven scanning mirror

In the previous sections, a fs holographic system was presented for enhanced cell transfection. With this system, a "point and shoot" capability is demonstrated with flexible targeting modalities for fs irradiation of mammalian cells. Significant improvement in optoinjection efficiency was achieved with precise targeting of the membrane using a triple axial dosage, applying sequential fs pulses at different axial positions. On the other hand, 16 shots on the membrane enhanced the transfection efficiency of mammalian cells. However, the system targeting capabilities is constrained by its small 70 μm field of view. The system's versatility could be further enhanced with a wider field of view allowing optical transfection of single or multiple cells in an array on a tissue and observing for the subsequent effect on its neighbouring cells. Furthermore, a wider-field targeting capability accommodates beam multiplexing allowing several cells to be targeted at a time in a single field of view increasing the throughput of the system.

An additional platform that could increase the field of view for targeting is to incorporate a piezo-driven scanning mirror in the setup. With a piezo-driven scanning mirror in tandem with a SLM, a full-field of view targeting with full axial control could be achieved. The scanning mirror is utilised to laterally translate the beam, meanwhile, the SLM could enable axial positioning and beam shaping by wavefront modulation of the laser beam. Decoupling the lateral and axial control provided more flexibility on the system by having a more uniform power when the beam is translated over the whole field of view, removing the need for amplitude correction for "point and shoot" targeting.

The modified optical train is shown in Fig. 5.11. Similar to Fig. 5.2, the fs laser beam passes through an electronic shutter and a $\lambda/2$ waveplate and PBS

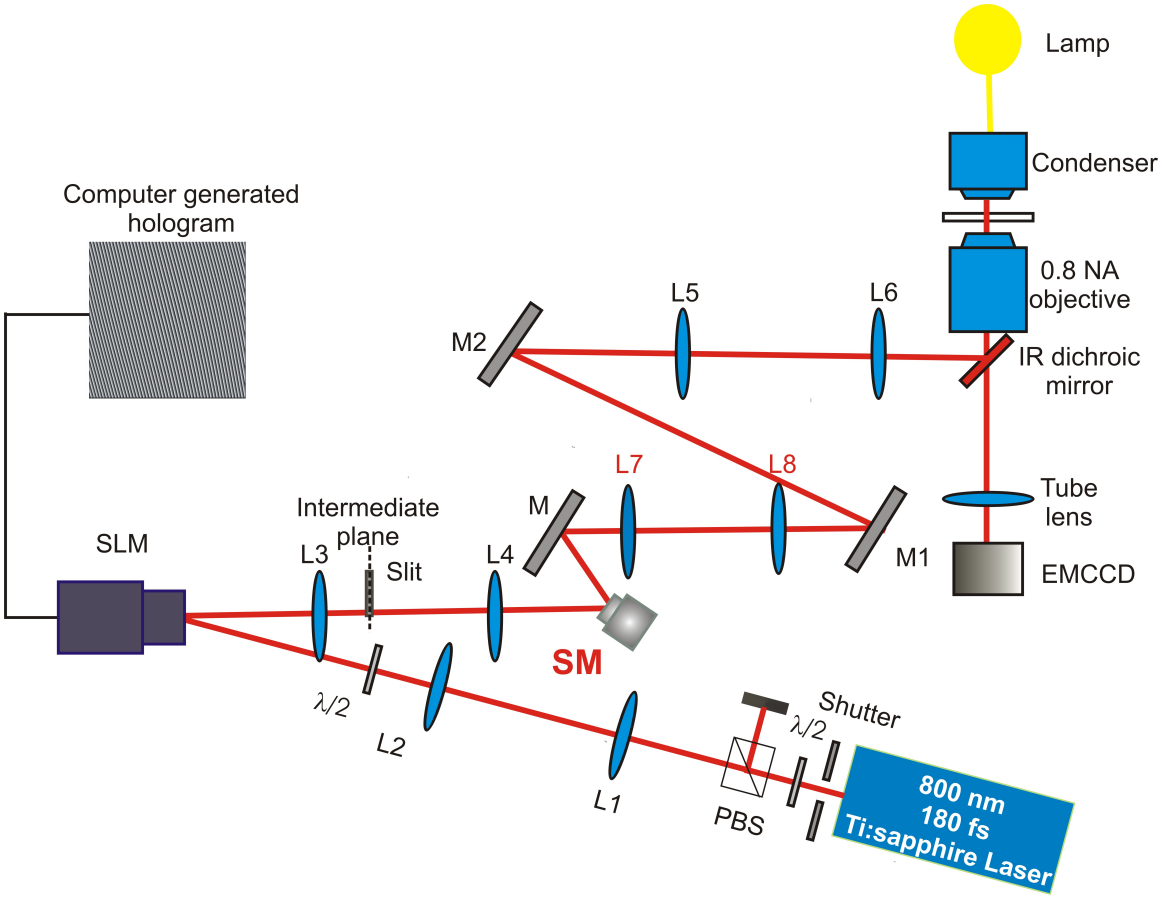

Figure 5.11: (A) Modified optical train with the scanning mirror (SM) in place. L-lenses; M-mirrors; PBS-polarising beam splitter; $\lambda/2$- half wave plate; SLM-spatial light modulator. Lenses: f_1= 50 mm, f_2= 1000 mm, f_3= 500 mm, f_4= 125 mm, f_5= 200 mm, f_6= 200 mm, f_7= 150 mm and f_8= 300 mm. In this configuration, each cell in the field of view can be irradiated with uniform power for optical injection and transfection.

pair for power attenuation. Lenses, L_1 and L_2 with focal lengths, f_1= 50 mm and f_2= 1000 mm respectively, expands the beam to overfill the SLM active area. At the SLM, a fixed CGH of a linear blazed grating is imposed to separate the 1st order from the rest of the diffraction orders. All the other orders are blocked at the intermediate plane. The 1st order beam from the SLM is demagnified using lenses L_3 and L_4 with focal lengths f_3= 500 mm and f_6= 125 mm respectively. In order to avoid loss of power, the beam incident into the 12.5 mm (diameter) of the scanning mirror (SM-S334, Precision Instruments) was made smaller ($\approx$ 5 mm) than the mirror aperture. The piezo-paired driven scanning mirror has a milliseconds response time and can provide a tip-tilt range of 60 mrad. It has a reflectivity of 98% over the wavelength range 500 nm–2 μm. L_7 and L_8 (f_7 = 150 mm and f_8 = 300 mm) expands the beam to twice its size in order to overfill the backaperture of the objective. In order to optimise the scanning feature of the mirror over the whole field of view and to ensure that any wavefront modulation at the SLM is imaged to the sample plane, the SM should be at a conjugate plane with the SLM. Hence, lenses L_3 and L_4 are in 4-f configuration with the SLM and SM. The distance between L_3 and L_4 is the sum of their focal lengths.

Steering the beam with the SM ensured that the power was maintained all throughout the field of view. A slight defocusing was observed when the beam was scanned at the edges due to the curvature of the plano-convex lens used after the SM. To improve this, an F-theta lens should replace L7 in the system inorder to ensure a flat image field at the sample plane during the beam steering.

Fig. 5.12(A) is a still image of a video showing a touch-screen interface whereby remote operation of the femtosecond holographic system is possible allowing "point and shoot" over the wireless internet. A LabView program allows remote access by linking the transfection software with the touch-screen interface of a laptop. This technology could be particularly useful for studies requiring cell transfection in the presence of highly-dangerous mutagens which requires the microscope to be enclosed in a laboratory hence, control of the system may only be performed through remote access. Furthermore, in order to show the system's wider-field targeting capability, optoinjection of fluorescent dye in mammalian cells were performed in a patterned manner. A dish with a confluent monolayer of CHO-K1 cells was bathed with a 3 μM solution of PI. In order to provide precise and accurate control of the field of view to be targeted, the microscope was fitted with a motorized stage (Marzhauser Scan, IM 120x100) that can be computer-controlled as well. A predefined checkerboard pattern was created, requiring four fields of view each with an area $\approx$ 140 μm by 140 μm of cells to be targeted. After targeting all the cells, the stage is moved towards the next predefined field of view. Fig. 5.12 (B) shows an image of of optoin-

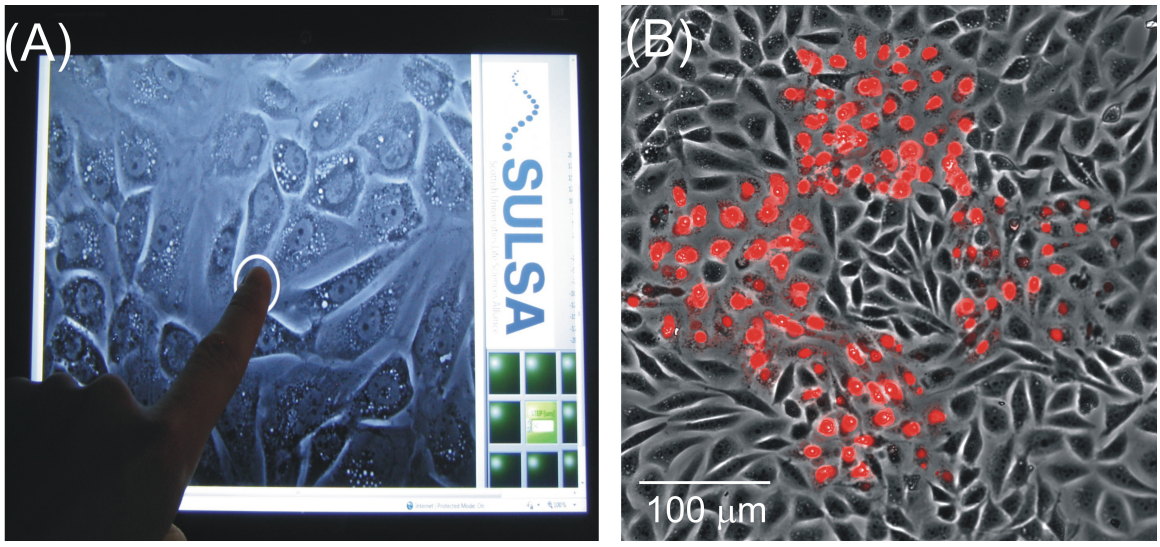

Figure 5.12: (A) A still image of a video of the system showing a touch-screen interface which allows remote operation of the femtosecond holographic system allowing point and shoot of cells over the wireless internet. (B) An image of CHO-K1 cells optoinjected with PI in a checkerboard pattern.

jected cells with PI in a checkerboard pattern. Hence, the system could be used to create optoinjected cells in a user-defined arrangement which could be employed to target specific cells cultured on chemically micro-patterned surfaces. The technique enables targeted gene delivery of cells in a pattern for applications studying cell behaviour, wound healing and cellular interactions.

5.6 Discussion and Conclusions

This chapter presented a fs holographic system for enhanced optoinjection and cell transfection. It utilised a dynamic and reconfigurable spatial light modulator that allows fast lateral translation and axial positioning of the laser beam with respect to the cell membrane. Wavefront modulation enabled fast beam steering to provide "point and shoot" and precise axial control which is crucial to the efficiency of optoinjection and cell transfection.

Computer control of the femtosecond holographic system provided flexible and accurate sequential dosage enabling different poration modalities. Targeting modalities such as "single", "triple axial" and "triple lateral" dosage were tested at laser parameters P= 70 mW and T= 40 ms inorder to determine the percentage of optoinjected and viable cells. Significant improvement was achieved with triple axial dose over a single dose on the optoinjection of PI into CHO-K1 cells, showing an increase of the percentage of optoinjected from 45% to 72%. Hence, precise targeting of the membrane is crucial for optoinjection of molecules. For fs optical transfection, at laser parameters P= 60 mW and T= 40 ms, increasing number of membrane pores increased the average optical transfection efficiency compared to a single dose. Furthermore, a significant improvement was achieved over single dose when 16 shots of 4 by 4 pattern of dosage was created on the membrane using laser parameters, P= 30 mW and T= 40 ms. With this poration modality the average efficiency almost doubled from 34% to 60% compared to single dose.

In comparison to optoinjection, wherein a visible gas bubble is a precursor to successful optoinjection, at the combination of parameters for successful optical transfection experiments, visible gas bubbles were not observed in all modes of poration. In fact, a combination of laser parameters in the absence of visible gas bubbles was found to be effective for optical transfection, previously mentioned as well by other independent studies [158, 159]. In contrast to optoinjection wherein a considerable size (greater than 500 nm) of a pore maybe required for a significant amount of fluorophore to diffuse in the cytoplasm, optical transfection may require less mechanical disruption and small-size and short-lived changes on the membrane not resolved by our current microscopy system is sufficient for DNA to enter the cytoplasm. As discussed in Chapter 3, precise dissections performed using NIR fs lasers are due to photochemical reaction arising from low-density plasma during laser interaction with the subcellular organelle. In the same way, changes in membrane permeability during optical transfection maybe governed by ROS species that interacts with the membrane which are present during fs irradiation. In contrast to optoinjection, wherein its success can be purely attributed to the diffusion of the fluorophore in the cytoplasm, the transport of the DNA during optical trans-

fection maybe different. The entry of the DNA into the cytoplasm maybe due as well to a binding mechanism wherein the subtle changes during irradiation of the cell membrane enables the plasmid DNA to bind to the outer leaflet of the plasma membrane similar to electroporation as discussed in Chapter 2. Future work should include mechanistic studies of the transport of DNA in the cytoplasm during laser irradiation which to my knowledge has not yet been fully investigated. I recommend on using single-molecule fluorescence microscopy by tagging DNA fragments with nucleic acid stains such as TOTO or YOYO (Invitrogen) in combination with membrane stains for future studies to allow imaging and understanding of the delivery of DNA plasmids into cells by optical transfection. Further understanding of the mechanism of optical transfection will enable improvement on the efficiency of the system especially for high-throughput applications.

The presented optical system provides an avenue for automated, high-throughput targeting of adherent cells. This chapter showed that a raster scan mode of poration could provide an average transfection efficiency of around 24 %. As a next step, an appropriate image algorithm could be utilised in order to identify the cells in a field of view and perform automated targeting to individual cells. Automation in microscopy has been applied particularly for high-throughput automated genome and chemical analysis [160], fluorescence based viability asssays [161] and high-throughtput iRNA screening [162]. In this chapter, selective two-step optical transfection was also demonstrated by creating a mixed population of fluorescing and non-fluorescing cells. In this experiment, I showed that cells which were tagged with GFP can be specifically targeted and transfected with a different plasmid yielding a population of cells expressing both GFP and Mito-DsRed protein. In combination with image segmentation and epi-fluorescent imaging, the system opens the way to automated multi-step gene therapy based on earlier delivery and expression of one of the genes.

To improve the range of beam steering of the system, a piezo-driven scanning mirror was inserted in the system. This provided a full field of view "point and shoot" capability allowing more cells to be targeted, increasing the applicability of the system to target complex biological samples. CHO-K1 cells were optoinjected or optically transfected in a pattern. In this chapter, the capability of the system to optoinject large number of cells in a user-desired pattern was demonstrated with a monolayer of CHO-K1 cells optoinjected with PI in a checkerboard manner. Furthermore, the system could also be remotely accessed over the wireless internet which opens the possibility for remote "point and shoot" of cells for optoinjection and optical transfection.

One aspect of the system that is not fully described here is the potential to use the

same fs laser holographic system to perform nonlinear imaging and specific targeting of cells in a tissue for delivery of genes *in vivo*. Previously, a multiphoton imaging system has been employed for image sectioning of a thick samples as well as precise deep tissue ablation [163]. In the same manner, the fs holographic system could be used for multiphoton imaging, identification of cells to be transfected, optical transfection of specific cells and tracking of the fate of transfected cell. The fs holographic system is a versatile, user-friendly system for optoinjection and optical transfection with the potential for commercialisation. At present, the device is still bulky, occupying large optical table space which may limit its portability. A similar design using the violet diode laser presented in Chapter 4 maybe the future prospect in order to build a small box design with the same functionalities.

In the following chapter, the NIR fs holographic system described here will be utilised to perform optical injection and manipulation of developing *P. lamarckii* embryos. Employment of NIR fs holographic system for optical manipulation of embryos provides an advancement in the embryology field as they could be an alternative to conventional microinjection technique.

Part of this work was published in Journal of Biophotonics, **3**, 2010 [14].

6

Integrated optical approach for the manipulation of developing embryos

In this chapter, a complete optical approach for the manipulation of a developing embryo will be presented. Optical manipulation in this context, is broadly defined as a means to orient, trapped a biological sample using a laser. Similarly, this chapter demonstrates successful intracellular delivery of a range of impermeable molecules into individual blastomeres of the annelid Pomatoceros lamarckii embryo by optoinjection, even when the embryo is still enclosed in a chorion using the fs holographic system. By switching to the continuous wave mode of the Ti:sapphire laser, the same system can be employed to optically trap and orient a single embryo whilst maintaining its viability. Hence, a full all-optical manipulation platform is demonstrated paving the way towards single-cell genetic modification and cell lineage mapping in emerging developmental biology model species.

6.1 Introduction

Optical manipulation allows contact-free handling of microscopic biological samples [164]. Using light, a microscopic species can be probed, trapped, sorted and optoinjected in order to understand its physiological properties and its response to mechanical, chemical or environmental stimuli. Importantly, optical manipulation

of biological samples is fully sterile, compatible with microscopic imaging and can be easily automated for high throughput image-based processing. Often it also causes less stress and collateral damage when compared to traditional mechanical techniques, which provides much better long-term viability of manipulated samples. A focused laser beam can exert sufficient force to tweeze and orient a cell or subcellular organelle [165]. Optical manipulation of biological samples such as cells, bacteria and DNA molecules have been extensively employed as a tool for holding, stretching and characterising samples [165]. At the same time a pulsed focused laser beam of sufficient intensity can porate the membrane of a single cell leading to optical injection of molecules and genetic material [16, 18].

An important advantage of optical tools for manipulation is their easy reconfigurability, which provides much needed versatility in a multi-modal operation on a variety of samples. For example, a multiphoton system can be utilised for both subsequent imaging and laser ablation [166]. Similarly, a single fs laser system can be toggled between continuous wave (CW) and fs operation for optical trapping of cells and intracellular delivery of macromolecules [21]. Since optical manipulation systems are often built around microscopes, subsequent long-term imaging is possible without disturbing the sample on the stage, maintaining the physiological environment of the sample.

This work demonstrates optical manipulation of a complex biological sample, such as a developing embryo. Although optical trapping of single cells has been employed in many applications, such as Raman spectroscopy [167], optical stretching [168] and microrheology measurements [169], there were very few studies on optically orienting and trapping embryos, which are tens of microns in size. Optical trapping of single cells has been employed in model systems such as CHO cells [170, 171], fibroblasts [172] and *E.coli* bacteria [173] with a maximum optically trapped size of 20 μm. Optical trapping of larger specimens has often been demonstrated using optoelectronic tweezerss (OET) for the orienting and trapping of motile specimens such as *Tetrahymena pyriformis* [174]. OET of mouse embryos has also been demonstrated for the purposes of embryo sorting prior to implantation [175]. Recently, optical trapping of a variety of swimming motile specimens was reported using a dual beam mirror trap [164]. These results show that a non-contact automated optical method to move, orient and hold developing embryos would provide an alternative over the commonly used intrusive glass capillaries, which cause unnecessary stress in the sample and require manual dexterity.

At the same time, there is significant interest in finding alternatives to microinjection based delivery of DNA, mRNA or siRNA into single cells of developing embryos for the purposes of their cell selective genetic modification. In recent years, optoin-

jection by NIR fs laser pulses has been found to be an effective tool in delivering different types of biomolecules into single cells with high post-treatment viability. Focused NIR fs lasers create a transient pore due to membrane interaction with a low density plasma created by multiphoton ionisation [97]. The focused NIR fs pulses interaction with tissue or cells relies on nonlinear absorption; hence, the affected area is limited to the focal volume of the laser beam enabling a highly targeted and precise ablation *in vivo* with limited collateral damage in the surrounding cells. To date, utilising NIR fs pulses for optoinjection of an embryo has only been reported on large (1 mm) zebrafish [120] and (1.5 mm) *Xenopus laevis* [176] . However, the absorption, structure and size properties may be completely different with embryos of different species.

In this study, two modes of Ti:sapphire laser operation were used in a combined system for optical manipulation and injection of small developing embryos. By toggling between CW and pulsed mode-locked operation, I demonstrate independently optical trapping of the 60 μm sized embryos of *Pomatoceros lamarckii* and optical injection of macromolecules into its individual blastomeres. In this work, I show how the holographic system based on a spatial light modulator (SLM) presented in Chapter 5 can be used as a highly flexible tool for stable trapping of an embryo and enhanced targeting of its individual blastomeres. By changing the light wavefront modulation encoded on the SLM, three dimensional beam steering and multiplexing can be achieved. Using this system, individual embryos can be positioned and oriented in three dimensions using a low NA objective, allowing optical orientation and manipulation within a large field of view. At the same time, as demonstrated in Chapter 5, an SLM can be used to enhance viable optoinjection of single cells by more precise multiple targeting of their membranes. The versatility and ease-of-use offered by this combined system opens new avenues in flexible and dynamic manipulation of developing embryos.

The samples were obtained from Dr. David EK Ferrier (Scottish Ocean Institute, University of St. Andrews). Dr. Hana Cizmarova contributed towards sample preparation. The optical trapping work was performed in collaboration with Dr. Maciej Antkowiak. The author performed all the experiments presented in this chapter.

6.2 Pomatoceros lamarckii

The specific interest in this chapter is to perform orientation and trapping of developing 60 μm sized embryos of *Pomatoceros lamarckii* as well as as well as optoinjection of fluorescent dyes of varying sizes into its individual blastomeres. *P. lamarckii* is a

marine organism, abundant in intertidal and shallow sub-littoral zones. They form calcareous habitation tubes attached to stones, shellfish and ship hulls. *P. lamarckii* is found to be a significant biofouling agent and causes considerable economic loss particularly for mussel farming [177]. *P.lamarckii* has also been considered a dependable resource of mitotic cells and can spawn naturally almost all year long with a temporary stoppage for 1-2 months [178]. They have been studied for ecotoxicology research, assaying larval survival and anaphase aberration for detection of mutagens in the marine environment [178].

In the literature, *P. lamarckii* has been reported to be found in various coastal areas in the UK and Ireland such as Tinside, Plymouth [179, 180, 181, 178], Bantry Bay, Ireland [177], the south coast of Cornwall [178] and France [182]. Initially, there were thought to be the same species as *Pomatoceros triqueter* [183] but morphological differences in their operculum structure confirmed that they are separate species [182]. In *P. triqueter*, the operculum is mounted obliquely on the peduncle and characteristically convex, cone-shaped. On the other hand, *P. lamarckii* is mounted centrally on its stalk and concave in shape [181]. Currently, the two species of *Pomatoceros* can be distinguished by their depth preference and habitation tubes. *P. triqueter* exists subtidally up to depths of 70 m and has a habitation tube with a single central keel visible with a semicircular opening [184]. While *P. lamarckii* has three keels and has sharper, almost triangular, opening.

P. lamarckii is a member of the Lophotrochozoa clade of bilaterian animals, which are relatively poorly represented in terms of our understanding of animal development [180, 179]. These polychaete annelids have relatively conserved gene sequences and complements, as well as gene and genome organisation [179, 185, 186]. Due to their conservative evolution and retention of many ancestral characteristics, *P. lamarckii* is considered to be a promising model for understanding animal evolution [187, 188]. However, at present there is no technology that has been demonstrated to allow successful and viable manipulation of the embryo of this species. Hence, developing optical methods to manipulate the embryos of this species would significantly improve our capabilities in understanding the development of *P. lamarckii* and open the way to manipulate other small embryos.

6.3 Optical trapping

In order to implement the confinement and three dimensional positioning of an embryo, one needs to understand how light acts on a particle in an optical trap. Optical trapping was pioneered by Arthur Ashkin and presented in his seminal paper published in 1970 which states..."*if a beam with milliwatts of power hits a*

2.68 μm sphere off center, the sphere is simultaneously drawn into the beam axis and accelerated in the direction of the light" [189]. Since then, optical trapping has become a powerful tool to manipulate and control particles of a variety of sizes. This technique is based on the concept that light itself carries momentum given by the relationship,

$$p = \frac{E}{c} = \frac{h\nu}{c} = \frac{h}{\lambda} \tag{6.1}$$

where $E = h\nu$ provides the energy of the photon and λ is the wavelength of the light. The interaction of light with an object causes a change in the direction of light, either by being reflected or refracted. This induces a transfer of its momentum which consequently results to an applied force on the object due to Newton 2nd law, F=$\frac{\partial p}{\partial t}$. Light exerts a force in the range of pico to femto Newton that may feel insignificant for macroscopic objects but has the capability to propel, guide and tweeze microscopic objects.

An optical trap may be visualised as a *potential well* wherein the trapped object oscillates in the vicinity of the lowest energy potential. It is also equivalent to a mass-spring system where the force on the particle is given by F= kx, the stiffness or the quality of the trap is characterised by k given a displacement, x from the equilibrium position. Due to the transfer of momentum of light to the particle, the particle will experience a force which attracts it to the highest intensity of light. The force exerted by light is conventionally decomposed into two components, a scattering force which acts to push the particle along the direction of the light while the gradient force which acts to pull it at the position of highest intensity. In order to obtain a stable optical trap in three dimensions, the axial gradient component must exceed the scattering component in order to counteract the push on the particle away from the highest intensity region. The condition necessitates the use of high NA objectives (NA>1) to achieve a very steep gradient in intensity. There is a small offset due to the balance of the scattering and gradient force, hence the equilibrium position of the trap is located a few microns downstream the focus.

The size of the optically trapped object with respect to the wavelength of light dictates which mathematical treatment one use to understand an experimental scenario. Firstly, if a particle has a radius *(r)* smaller than the wavelength of light ($r << \lambda$), then the particle can be considered as an electromagnetic dipole in the **Rayleigh regime**. On the other hand, when the particle's radius exceeds the wavelength of light ($r >> \lambda$), **geometric optics** can be used to analyse the optical forces from refraction and reflection. For completeness of discussion, I will detail optical trapping for both size regimes. However, as the size of material employed in this work is tens of microns in size, the geometric optics trapping will be sufficient to

explain the forces on the object for this chapter.

6.3.1 Geometric optics

In this regime, where in the particle size is much larger than the wavelength such as r>10 λ, geometric ray optics is suffice to explain the interaction of light with the particle. In geometric optics, the optical forces are independent to the particle size [190]. In the following scenario, let us consider a particle with an index of refraction greater than the surrounding medium. The particle will cause the refraction of an impinging light ray. Based on Newton's 3^{rd} law, this will cause the particle to be pushed in the direction *opposite* to the refracted ray direction. Let us consider a laser focused by a lens with a Gaussian profile as shown in Fig. 6.1. An axial gradient force acts to confine the particle along the axial direction shown in Fig. 6.1(A). The scattering force (F_{scat}) is directed along the direction of the light. However, due to the refraction of light pointing in the direction of F_{scat}, the gradient force (F_{grad}) component opposite the direction of light propagation will pull the particle towards the region of highest intensity. When the ratio of F_{grad} and F_{scat} is greater or equal to 1, a three dimensional optical trap can be obtained.

A particle acted upon by intense ray and a dim ray is shown in Fig. 6.1(B). In this case, the *action and reaction force* pair due to refraction of light and the net force on the particle can be understood more clearly. The intense ray signifying a higher intensity compared to dim ray is refracted by the particle towards the left. However, the light will push the particle with equal and opposite force towards the right. Considering the rays acting on the particle are symmetrical but having a Gaussian in intensity profile, the particle will always be pushed towards the center, where the highest intensity occurs. Although simplistic in nature, the geometric optics is a good basic foundation in understanding the forces and the concept of confinement of a particle in an optical trap. A more thorough and detailed calculation of the forces on a dielectric particle using geometric ray optics is presented by Ashkin [191]. However, the geometric optics treatment is only limited to relatively large particles. But in scenarios where very small particles are optically trapped wherein light is scattered elastically and the index of refraction of the particle with respect to its environment is considered, the Rayleigh regime provides a more accurate assessment on the forces on the particle.

6.3.2 Rayleigh optical trapping

In this regime, the incident electromagnetic field is constant over the entire particle and the scattering force is due to absorption and re-irradiation of light by the par-

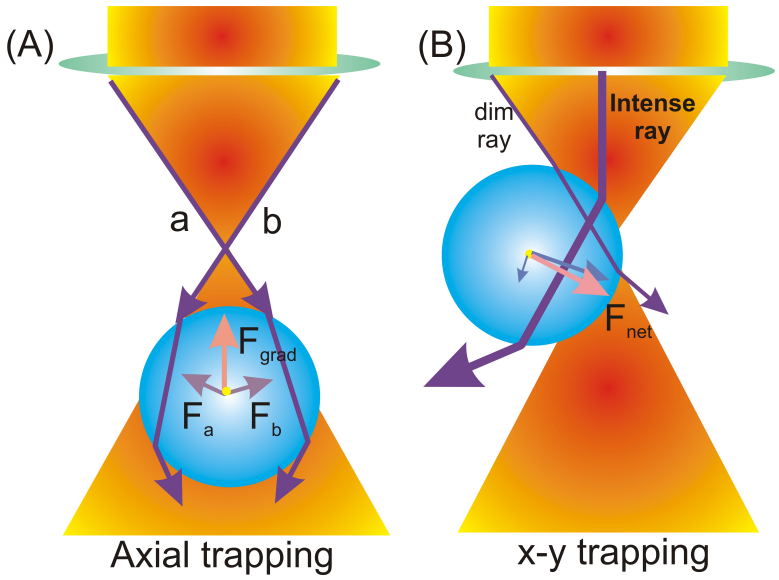

Figure 6.1: A schematic diagram of optical trapping force using geometric optics. (A) shows rays a and b being refracted as it impinges on a particle. The scattering force is directed downwards but the net gradient force propels the particle towards the focus of the beam. (B) shows an intense ray on a particle thereby changing its direction. By action and reaction, light will push the particle in the opposite direction, pushing the particle towards the highest intensity region of the beam.

ticle. The total force can be decomposed into its components, the F_{grad} and F_{scat} [190] as shown below

$$F_{scat} = \frac{I_o \sigma n_m}{c} \tag{6.2}$$

wherein

$$\sigma = \frac{128\pi^5 r^6}{3\lambda^4}\left(\frac{m^2-1}{m^2+2}\right)^2 \tag{6.3}$$

where I_o is the intensity of the incident light, σ is the scattering cross-section of the sphere, n_m is the index of refraction of the medium, m is the ratio of the index of refraction of the particle (n_p) and the medium. Meanwhile, the time-averaged F_{grad} can be obtained using the following equation [190]

$$F_{grad} = \frac{2\pi\alpha_p}{cn_m^2}\nabla I_o \tag{6.4}$$

wherein

$$\alpha = n_m^2 r^3 \left(\frac{m^2 - 1}{m^2 + 2} \right)^2 \tag{6.5}$$

where α_p is the polarisability of the sphere.

From Eq. 6.2 and 6.4, simply increasing the intensity of the incident light will not create a three-dimensional optical trap. Clearly, a strong factor is the scattering cross section and the polarisability of the particle which depends mainly on the ratio of the index of refraction of the particle with respect to its environment. This imposes a limitation on the particles that can be optically trapped to only high index of refraction materials ($n_p \approx 1.5$) such as polymer or silica. The optical wavefront of a laser beam have to be modified to a Laguerre-Gaussian [192, 68] or vortices [193] in order to trap low index materials.

The theoretical treatment of the forces acting on a particle in an optical trap is progressing towards a more generalised and complete theory ranging over varying sizes of particles. Notably, the majority of sizes of particles optically trapped falls between the sizes of 0.2-5 μm wherein the geometric optics and the Rayleigh regime fails. Rayleigh regime provides a more accurate force calculation compared to geometric optics and is often extended to increase its applicability to larger particles. Chaumet and Nieto-Vesperinas derived an expression for the total time averaged force on a sphere in Rayleigh regime but may also be applied to larger particles using coupled dipole method [194]. A more complete overview of current approaches for calculating trapping forces are presented elsewhere [190].

6.3.3 Optical trapping configurations

Based on the concept that light can induce a momentum change and thereby can exert a force on a particle led to the development of the field of optical trapping. The most common configuration is a single-gradient laser trap shown in Fig. 6.2(A), more commonly known as an **optical tweezers.** It has a similar configuration with most optical transfection systems shown in this thesis, wherein a single laser beam is focused very tightly using a high NA objective. This technique has been employed for handling and orienting a variety of particles such as microparticles [189], nanoparticles [195], living cells [167] and small-sized ultra-cold atoms [196].

In some applications, a single-beam gradient laser trap can be used to levitate objects [197]. In this case, a single beam is weakly focused providing a more dominant F_{scat} component, pushing the particle along the direction of beam's propagation axis (Fig. 6.2(B)). Low index refraction particles are often propelled in this type of trapping configuration such as hollow glass spheres which sometimes necessitates the use of donut mode beams [198]. For trapping of microparticles in air, at some point

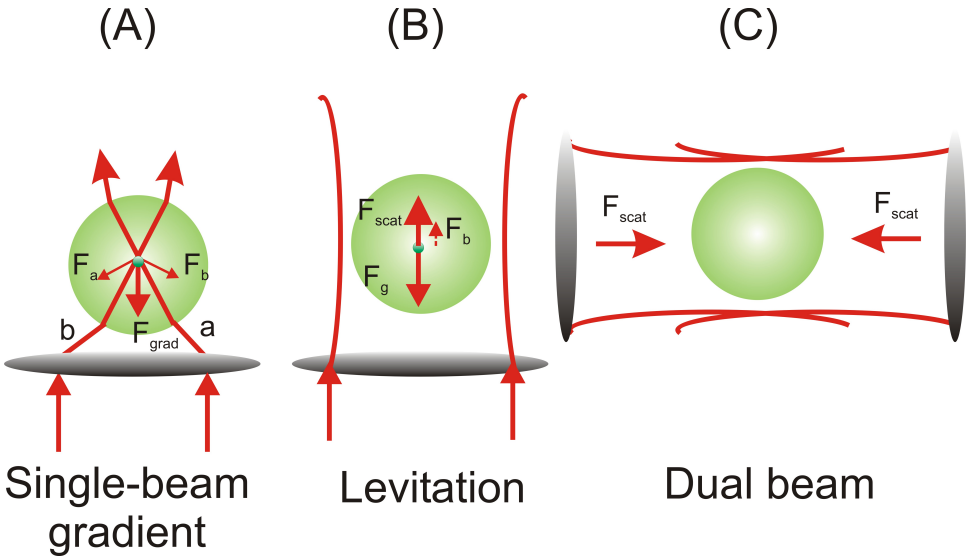

Figure 6.2: A schematic illustration of different trapping configurations. (A) shows a single beam-gradient trap more commonly known as optical tweezers in which a particle is trapped at the region of highest intensity of a tightly focused laser beam. (B) shows a diagram of levitation trap wherein a particle is pushed along the direction of the laser beam and is stably confined at the position wherein gravity (F_g) is equal with the scattering force (F_{scat}) for trapping in air. In water, the additional buoyant force (F_b) contributes to the upward scattering force. (C) shows a dual-beam trap in which two beams in a counter-propagating manner are used to confine the particle.

along its propagation axis, the F_{scat} component will cancel with gravity, F_g= mg. In water, the buoyant force (F_b) will contribute to the upward F_{scat}. In both cases, a stable region along the propagation axis can be found at which the object can be confined and move accordingly.

In a more sophisticated manner, an object can be trapped using two beams in a counter-propagating manner as shown in Fig. 6.2(C). In this configuration, the confinement is due to the balance of scattering force components from both beams. The particle is confined at the position where the F_{scat} component from each beam cancels. The confinement transverse to the propagation is provided by the F_{grad} due to the Gaussian profile of the beam. Dual beam traps are often employed using two independent optical fibres. This technique has been used for stretching cells [168], as well as, combined confinement and Raman spectroscopy of single cells [199].

6.4 Materials and Methods

6.4.1 Experimental Setup

The experimental setup was fully discussed in Chapter 5 and shown in Fig. 5.2. For optoinjection experiments, the laser, a diode pumped (Coherent, Verdi V-5) Ti:sapphire fs laser (Coherent, MIRA900) operating at 180 fs, 80 MHz with its wavelength centered at 800 nm was operated in mode-locked configuration. For optical trapping experiments, the Ti:sapphire laser was switched to CW mode operation with an output wavelength at 800 nm. The beam was directed through a 0.5 NA, ×20 air objective (Nikon). The shutter was open throughout the experiment. The three dimensional position of the focal spot within the sample was controlled by a combination of a blazed grating and a Fresnel lens displayed on the SLM, as described before in Chapter 5. At the same time, the beam could be multiplexed by displaying a complex superposition of multiple modulations.

The system was fully equipped with differential interference contrast (DIC) and epi-fluorescence imaging based on an EMCCD camera (Andor iXon+) used to monitor dye optoinjection and perform long-term imaging. All components of the system, such as the SLM, shutter and EMCCD camera, were controlled by a user-friendly software (Labview 8.5) for sequential doses performed in the optoinjection experiments as well as for optical trapping experiments. The multi-modal platform was developed with a "point and shoot" functionality for optoinjection or in the case of optical trapping "point and trap" for ease of use. It was also capable of automated pre-defined displacement of the focal spot allowing a sequenced computer controlled dosage of laser in multiple spatial locations on the blastomere surface, providing enhanced optoinjection efficiency as shown in Chapter 5.

6.4.2 Animal collection

This study was conducted during the period of May–December 2010. Adult worms were collected at East Sands, St. Andrews and maintained in natural sea water at ambient temperature (approximately 15 ^{o}C during summer). Habitation tubes were attached to rocks and collected during low-tide periods. Although the rocks collected were abundantly populated by *P. lamarckii* tubes, there were a few instances were we found rocks with co-habiting species of *Pomatoceros*. Hence, prior to detubing, the tubes were distinguished from each other.

Adult worms (Fig. 6.3(A)) were removed from their calcified tubes by breaking open the posterior portion of the tubes and forcing the animals backward. Following de-tubing, fertile animals release their gametes. Fertile male worms have

cream-colored abdomen and emit a white or cream sperm material during detubing. Meanwhile, fertile female *P. lamarckii* have pink or orange abdomen and are larger in size than male worms. During the summer (May–July), large number of fertile animals were obtained; fewer specimens were collected during autumn to winter months (October–December). During the unreproductive stage of these worms, female worms tend to generate immature eggs, which are smaller ($\approx$ 24 μm) than mature eggs ($\approx$ 55–60 μm) (see Fig. 6.3(B)). Male worms tend to dominate the population. Male and female worms were transferred into separate petri dishes. In some cases, worms with no apparent gametes were obtained. These visual observations were in agreement with the study performed by Cotter and co-workers [200].

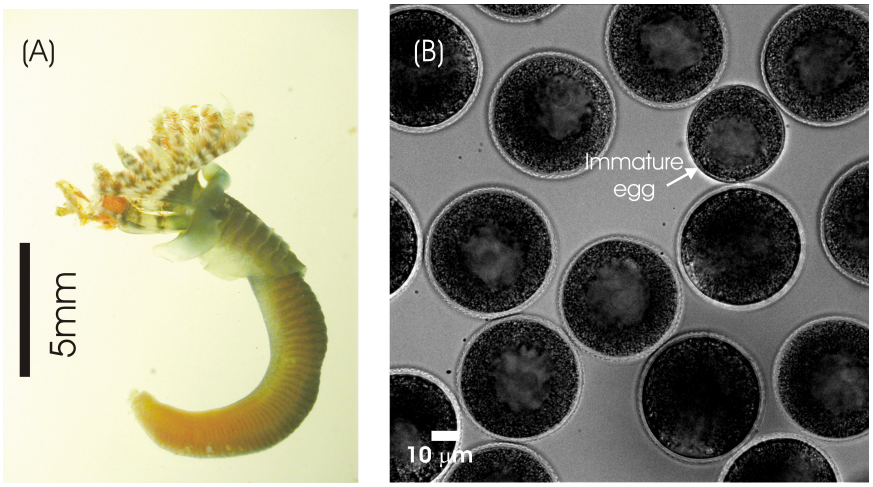

Figure 6.3: (A) Adult detubed *Pomatoceros lamarckii*. (B) Eggs obtained from a fertile *P.lamarckii* female worm.

Eggs were rinsed through a 100 μm sieve and then collected into a 40 μm sieve. 1.4 mL of water containing sperm were then added and left for 15 min to allow fertilization to occur. The embryos were washed and then transferred to a dish of fresh sea water. The embryos were kept in a Styrofoam box with an ice pack at one end to maintain the temperature between 14 and 18 ^{o}C.

6.4.3 Sample preparation

P. lamarckii embryos immersed in seawater were placed into 10 mm glass bottom petri dishes (World Precision Instruments). For optical trapping experiments, the glass-bottom petri dish was treated with 20 mg/mL poly-2-hydroxyethylmethacrylate (Sigma-Aldrich) in 95% ethanol and the solvent was allowed to evaporate, to prevent the embryos from adhering to the bottom of the dish. Optoinjection experiments

were performed with Texas red and Fluorescein fluorescently labeled dextrans of molecular weight 3 kDa, 10 kDa, 70 kDa and 500 kDa (Invitrogen) and propidium iodide (PI, Invitrogen) diluted in filtered seawater to a final concentration of 10 μM.

6.5 Experimental Results

6.5.1 Proper development of embryo is temperature dependent

Prior to optoinjection experiments, the conditions at which embryos will result into a proper developed embryos develop normally in the absence of laser treatment were first optimised. This requires counting the number of properly developed larvae in the population. A critical factor in the development of the embryos is the environmental temperature. In this subsection, the development of the *P. lamarckii* embryo was described and the optimal environment temperature which leads to normal body plan.

Two to three hours after fertilization, *P. lamarckii* embryos undergo equal spiral cleavage and subsequent divisions occur at 30 min to 1.5 h intervals at normal room temperatures of 20^{o}C. Incubating the embryos at cooler temperature (14^{o}C) slows down their development by up to 1 h. Six to seven hours after fertilization, embryos form a slit like opening called blastopore, after which the embryo/larva will start to rotate about the dish. Within 24 h after fertilization, the embryo will develop into a swimming diamond shaped larva called trochophore (see Fig. 6.4 (A)).

Three thousand embryos were monitored during the peak fertile season (June–August) to determine the percentage of population that developed into properly developed larva. The development of the embryo is severely affected by the room temperature, hence the number of properly developed embryos was determined for two conditions. An average of 100 embryos were placed in a dish and left inside a styrofoam box with an ice pack on one end which maintained the temperature around 14–18 ^{o}C. Another 100 embryos were placed in a dish and left at room temperature which during summer can reach up to 25^{o}C.

Representative images of normal juvenile trochophore larvae, 24 h post fertilization are shown in Fig. 6.4 (A). A properly developed trochophore can be characterised by a diamond-shaped normal body plan, with visible prototrochal cilia. The trochophore larva swims actively around the dish. Meanwhile, an abnormally developed larva is indicated in Fig. 6.4(A). Abnormal trochophore often swim in its place or does not move about around the dish. Embryos with an arrested growth are also counted as abnormally developed.

Fig. 6.4(B) shows the percentage of properly developed larvae for the two tem-

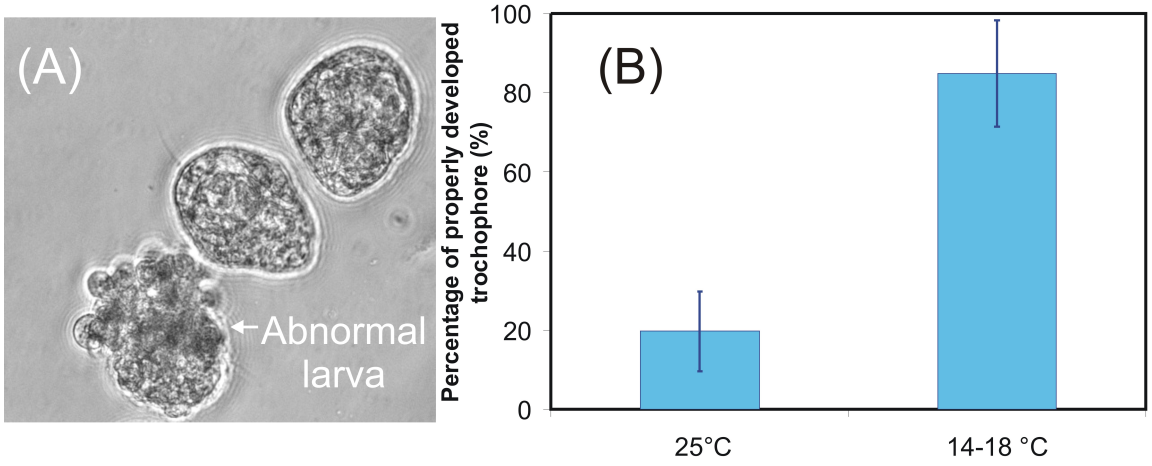

Figure 6.4: Images of (A) juvenile trochophore larvae after 24 h indicating abnormal larva. (B) Plot shows temperature dependence of properly formed juvenile trochophore larvae. Each data is n= 11 samples each containing 100 embryos. Error bar represents ± standard deviation.

perature conditions. With room temperatures reaching up to 25^o C, the percentage of properly developed larvae were only 20 ± 10%. With temperatures maintained between 14 and 18 ^{o}C, the percentage of properly developed larvae, increased four-fold to 85 ± 13%. Each data point is comprised of n= 11 samples containing an average of 100 embryos. Within 48 h, a complete trochophore larva develops with an apical tuft (At) situated at the apex, a visible rounded stomach (S), intestine (In) and protoctrochal cilia (pt). The mouth is found posterior to the pt while the anus is located posteriorly at the dorsal side (see Fig. 6.5) [180].

6.5.2 Intracellular delivery of macromolecules into living embryos

Single cell genetic modification *via* delivery of genes in a living embryo is an essential aspect in pushing the boundaries of developmental biology. Microinjection using a fine capillary needle is often utilised to deliver exogenous materials such as fluorescent dyes, DNA, RNA or morpholinos. However, this technique becomes very challenging when the size of cells to be injected is less than that of conventional model systems in embryology such as *Xenopus laevis* (1.5 mm), *Drosophila melanogaster* (200 μm by 500 μm) or *Danio rerio* (1 mm), for which systematic methods of manipulation and molecular biology are already well established. To date, microinjecting small embryos is still difficult to perform as the embryos are

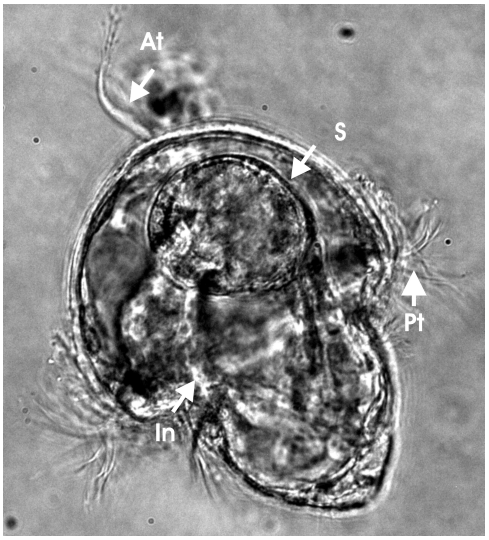

Figure 6.5: *Pomatoceros lamarckii* trochophore larva 48 h after fertilization. At-apical tuft, S-stomach, In- intestine, Pt-Prototrochal cilia.

prone to fluid loss or even bursting with small changes in tonicity, leading to compromised embryo viability. An even more challenging prospect is injecting material into micron sized blastomeres within well developed embryos. Accurate injection of exogenous material into an embryo requires experience in order to achieve high success rates.

Recent technological advances in microinjection including automated [40] and robotic systems [41] or microelectromechanical based devices [42] have been implemented for high throughput microinjection. However, the technique itself is still invasive leading to poor repeatability and low embryo survival. Methods such as chemical digestion of the outer layers or electroporation to permeabilise eggs and embryos have also been demonstrated [201, 202]. However, inherent toxicity with using chemicals on eggs and embryos is still an issue. Furthermore, both of these techniques are non-specific and lack cell-targeting capabilities. Hence, further development of procedures for the targeted injection of material into embryos is essential to enhance understanding in this field.

Ultrastructural studies on eggs of the sister species *Pomatoceros triqueter*, showed that the plasma membrane is first enclosed in a perivitelline space (500 nm) which is surrounded with a thick chorion (0.5–1.0 μm). External to this is an intermediate layer (70–100 nm) and an outer border layer (70–90 nm) [203]. In the present study, the mechanics of intake of fluorescein conjugated dextrans was investigated in early stage embryos by confocal imaging showing negative contrast images of the embryos.

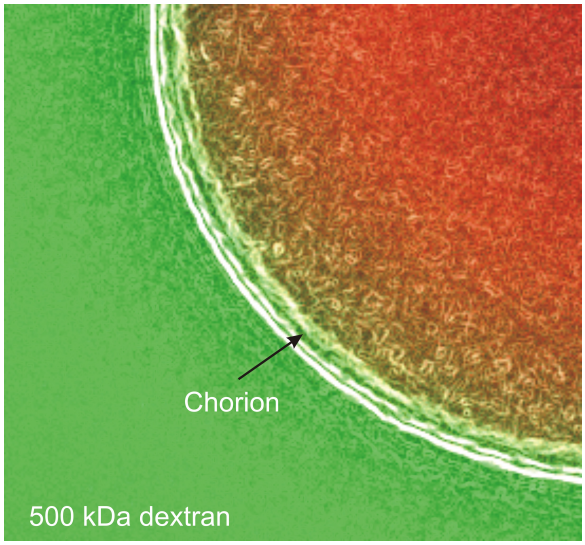

Figure 6.6: Fluorescence image of an embryo bathed in 500 kDa fluorescently labelled dextrans showing the chorion. The 500 kDa dextran can penetrate through the chorion layer but not the plasma membrane.

Staining of the plasma membrane with a lipophilic dye FM4-64 (Invitrogen) of soaked embryos in fluorescein fluorescently labeled dextrans showed that dextran size of 500 kDa can penetrate through the outer layers but not through the plasma membrane of individual blastomeres of the embryo as shown in Fig. 6.6. Embryos were optoinjected at 2-cell (Fig. 6.7 (A)) and 4-cell (Fig. 6.7(B)) stages of development with 3 and 70 kDa fluorescein labeled dextrans. Fig. 6.7(C) and 6.7(D) show that dextrans can be optoinjected into the blastomeres without removal of the chorion. Fluorescently labeled dextran of sizes 3, 10, 70 and 500 kDa were found to be successfully optoinjected into individual blastomeres of living embryos. Independent studies showed that dextrans larger than 500 kDa have a very low diffusion ratio in the cytoplasm [83, 84]. This implies that dextrans larger than 500 kDa are almost immobile and may not be able to diffuse passively in the cytoplasm of the embryo. Since 70 and 500 kDa correspond to DNA sizes of 106 and 760 bp respectively, they are representative of oligonucleotide sizes that are desirable to optoinject into these embryos. As a conclusion, individual blastomeres can be targeted without the need to chemically or mechanically remove the outer membrane of the embryo, leaving it intact during manipulation, which is crucial for proper development.

In the early stages of the embryo (2-cell and 4-cell stages) after optoinjection with the pulsed fs Ti:sapphire laser, the fluorescently-labelled dextrans can be seen to perfuse and spread within the individual blastomere within several minutes of the

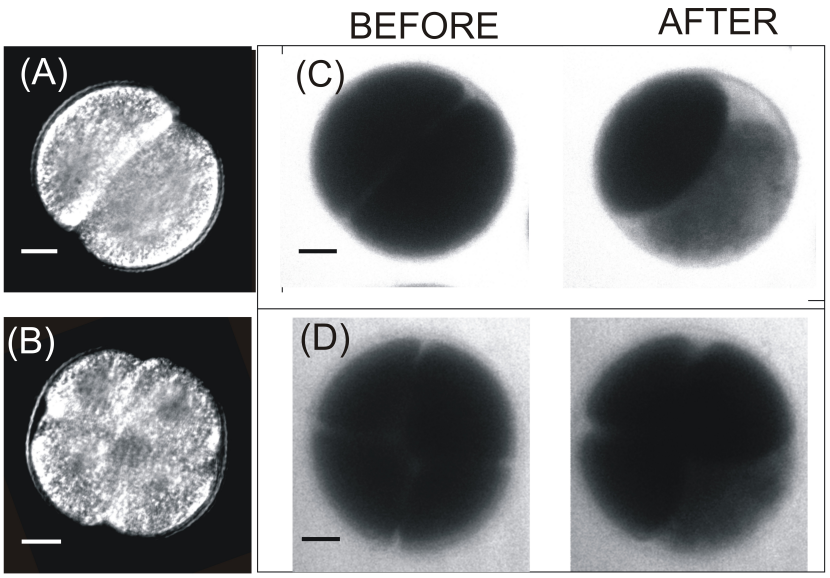

Figure 6.7: Images of (A) 2-cell and (B) 4-cell stage *P. lamarckii* embryos. Images in (C) show optoinjection of fluorescein labeled dextrans of size 3 kDa to 2-cell and in (D) 70 kDa to 4-cell stage embryo. Scale bar corresponds to 10 μm [204].

poration event. Similar to previous investigations on cellular poration, the presence of a gas bubble is a good indication of membrane disruption, leading to rapid diffusion of the dye into the targeted blastomere [27, 14]. However, without the gas bubble, the dye infusion was localised and did not spread throughout the cell. Importantly, cells adjacent to the optoinjected blastomere did not acquire any fluorescence signal, even 30 min after optoinjection, which implied delivery was contained and the dextrans did not pass through any gap junctions at this stage of development.

6.5.3 Laser parameters for gas bubble poration

Pulsed fs laser poration effects *via* laser-material interaction are due to the expansion and collapse of short-lived cavitation bubbles produced within a couple of microseconds of irradiation [107]. At sufficiently high laser intensity, long lasting residual gas bubbles lasting from milliseconds to seconds are visible using brightfield imaging. Based on our observations and corroborated by previous independent reports [27, 14] the presence of a gas bubble is a good indication of successful optoinjection; therefore, the laser parameters using NIR pulsed fs mode of Ti:sapphire laser required to produce a gas bubble were determined as a function of embryo depth. At 5 μm from the surface of the embryo, only $\approx$ 0.8 nJ was required to obtain a gas bubble using

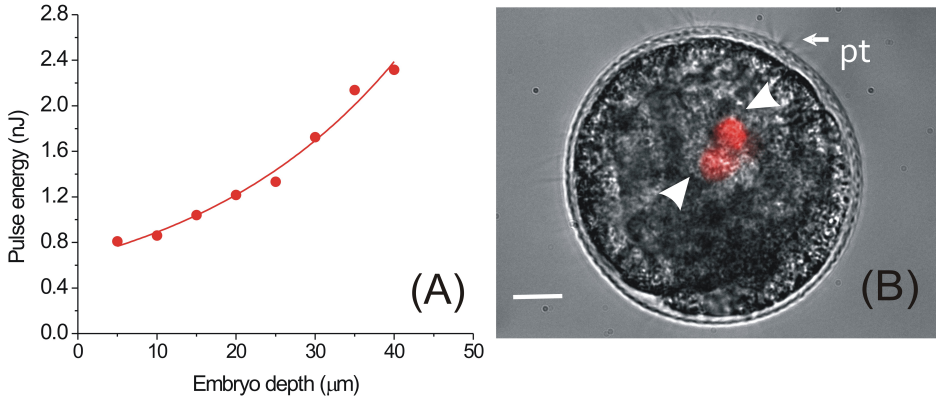

Figure 6.8: (A) Pulse energy required to generate a gas bubble as a function of depth of embryo. (B) An image of a well-developed embryo with 2 optoinjected cells. Pt are prototrochal cilia. Scale bar corresponds to 10 μm [204].

30 ms laser exposure. Thereafter, the required pulse energy increases as a function of depth within the embryo, as shown in Fig. 6.8(A). Probing deeper in the embryo necessitated an increase in the required pulse energy to create gas bubbles. This observation may be due to the combined effects of light scattering within the optically dense sample and increased spherical aberration of the beam with increasing embryo depth [205]. As shown in Fig. 6.8(A), at a depth of 40 μm into the embryo, the pulse energy required is 2.3 times more compared to 5 μm from the embryo surface.

To assess the success of optoinjection, *P. lamarckii* embryos of mixed cleavage stages were bathed in a solution of PI mixed in seawater to a final concentration of 10 μM. PI was chosen as it allowed the visualisation of fluorescence from blastomeres without the need to wash the embryos. Using this method, the fs pulse was focused tightly within the embryo, avoiding collateral damage to the surrounding cells. For example, a larva at the gastrula/early trochophore stage (manifested by the presence of visible prototrochal (pt) cilia) was optoinjected and is shown in Fig. 6.8(B). Two cells at a depth of 30 μm were selectively targeted and optoinjected with PI. Notably, cells above the targeted cells were not damaged and did not take up any dye during the process. This 3-D localised optoinjection capability, using fs pulses, could be utilised to follow internal cell lineages in later stage embryos and larvae. This specific delivery of material to internal cells is a unique feature of this optoinjection technique, as delivery by traditional microinjection would lead to piercing and damaging of cells in the capillary needle injection path.

Table 6.1: Optoinjection efficiency at varying embryo stage using the NIR fs pulsed Ti:sapphire laser with parameters P= 65 mW and T= 30 ms [204].

Embryo stage	1-cell	1-2 cells	2-16 cells	Late stage
Number of optoinjected (total number irradiated)	10(23)	19(42)	23(43)	26(47)
Percent optoinjected	43.5%	45.2%	53.5%	55.3%

Each blastomere was targeted at three different locations on its surface, forming an equilateral triangle of targeted dosage points (1 μm apart) by dynamically reconfiguring the phase pattern on the SLM. Individual gas bubbles were present at each of the delivered shot sites on the blastomere surface. Successful optoinjection was visualized 5 min after irradiation by detecting increased in fluorescence due to the intake of PI and subsequent intercalation of PI with DNA or mRNA. The optoinjection efficiency ranged from nearly 44% for single cell zygotes to 55% for late stage (greater than 16 cells) embryos using P= 65 mW and T= 30 ms. For early stage blastomeres, where the surface area is large compared to the later stages, the creation of multiple small to medium sized bubbles on the plasma membrane was required to induce successful optoinjection whilst maintaining the viability of the embryos.

Although the presence of a gas bubble is a precursor to successful optoinjection, their size and number correlates with embryo viability and the likelihood of normal development. Large bubbles often led to the leakage of blastomere contents, leading to compromised embryo development. Yolk granules and intracellular materials were found to diffuse out of individual blastomeres with large and long lasting gas bubbles.

Hence, the gas bubble size was investigated as a function of varying both P and T. Each embryo was exposed to the laser only once to avoid any cumulative effect during irradiation. The laser was focused on the layer where cortical granules are visible on a single blastomere within the embryo. The size of gas bubbles was grouped according to: small (<1 μm), medium (2–5 μm) and large (>5 μm). Visually, the gas bubble size can also indicate successful and viable optoinjection of embryos. Both small and medium size gas bubbles led to a high percentage of embryo viability but with varying success of optoinjection. Small size gas bubbles led to only 10–20% successful optoinjection while medium sized gas bubbles resulted in 40–50% successful intake of extracellular material into the blastomeres. Importantly, although the intake is 100% successful with large gas bubbles, it is at the expense of a very low percentage of embryo viability. The probability of obtaining a specific gas bubble size irrespective

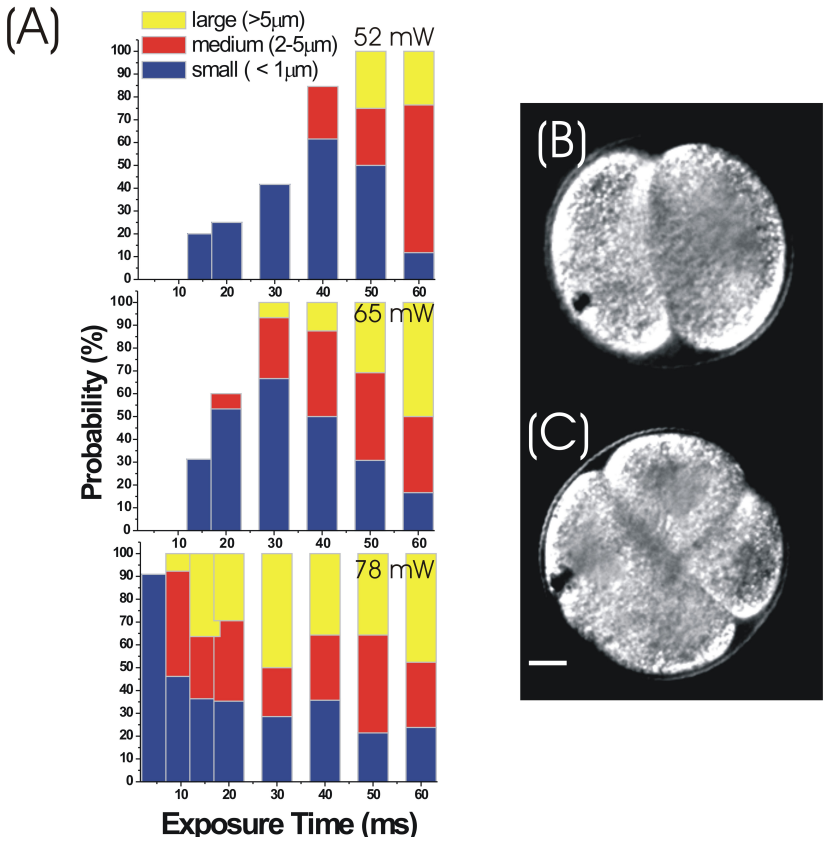

Figure 6.9: (A) The probability to form gas bubble on the surface of the blastomere as a function of exposure time at different laser power, P= 52 mW, 65 mW and 78 mW. For each P and T setting, n> 10 embryos were targeted. Image in (B) shows a medium size bubble ($\approx$ 4 μm) on a 2-cell stage embryo while (C) shows a large size bubble ($\approx$ 6 μm) in a 4-cell-stage embryo. Embryo in (C) immediately showed leakage of intracellular contents after irradiation. Scale bar corresponds to 10 μm [204].

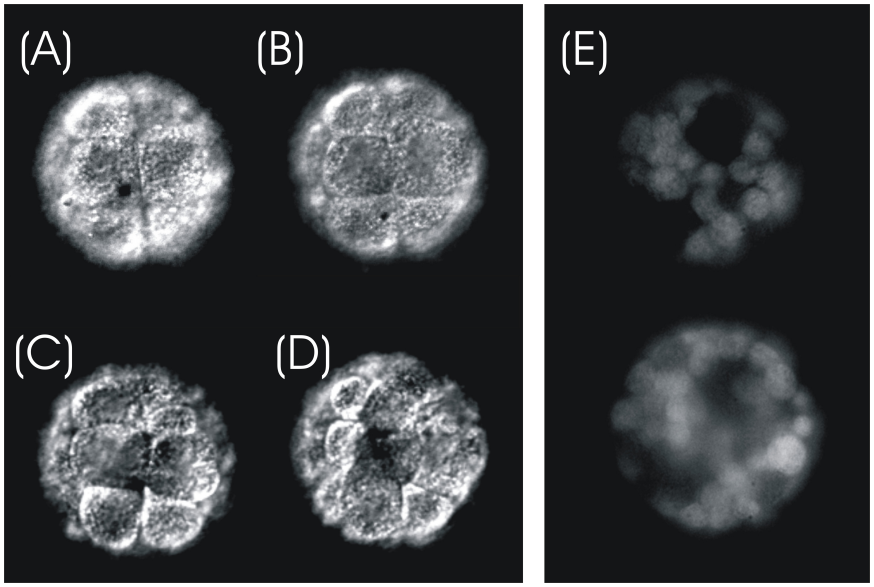

Figure 6.10: Image in (A) and (B) show gas bubbles created on the blastomeres of an embryo upon irradiation with fs laser (Media 1). Time lapse imaging of the same embryo (Media 2) with still images in (C) showing the blastomeres irradiated have retained morphological features without leakage and in (D) showing the blastomeres have carried on dividing. (E) Fluorescence images of an embryo at different imaging planes optoinjected with 3 kDa dextran at the early stage, which has carried on dividing and passed the dye to its daughter cells [204].

of embryo stage is shown in Fig. 6.9(A). Fig. 6.9(B) and 6.9(C) are representative images of medium sized and large sized gas bubble formed at the blastomere surface respectively.

It was observed that gas bubbles vary in size as a function of laser power and exposure time (Fig. 6.9). For P = 52 mW at T < 40 ms, the bubbles were predominantly transient and very small (<1 μm in size). With increasing T, medium sized bubbles with diameters of 2–5 μm were formed. Increasing P to 65 mW shifted the onset of generating medium to large sized bubbles to a shorter exposure time, from T= 40 ms to T= 20 ms. Medium to large gas bubbles which were more consistently formed at P= 78 mW and with T greater than 10 ms, tended to be long lasting and collapsed only after several seconds.

6.5.4 Viability of fs irradiated embryos

Of particular importance was the observation that individual blastomeres could carry on dividing following the induction of a gas bubble (Media 1, Fig. 6.10(A,B)),

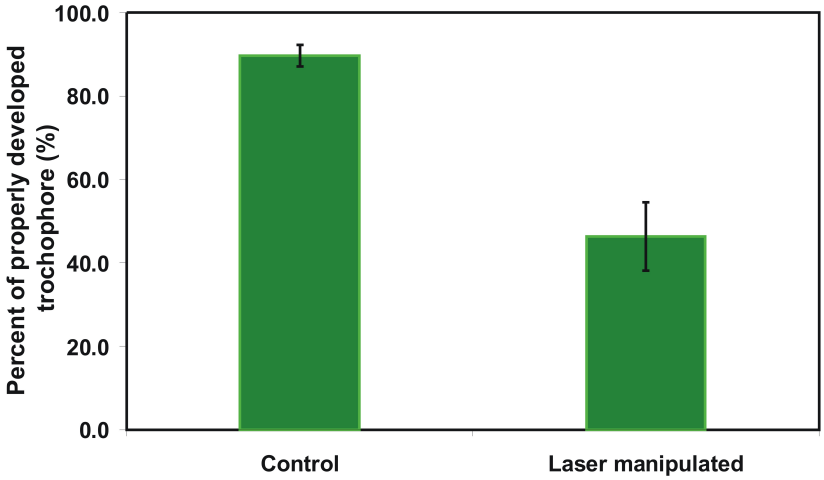

Figure 6.11: Plot of percentage of properly developed larvae for irradiated embryos (P= 60 mW, T= 40 ms) and non-irradiated embryos. Each data point consist of n= 3 samples, each with an average of 50 embryos. Error bar represents ± standard deviation.

as observed by time-lapse recording (Media 2, Fig. 6.10(C,D)). Time lapse imaging was performed on irradiated embryos over an hour following optoinjection. Two targeted blastomeres subsequently divided after irradiation with the fs laser. A percentage of the irradiated embryo carried on dividing and became a normal and viable trochophore larva, 24-48 h post fertilization. 46±8% of the embryos irradiated at 1-4 cell stage developed into proper trochophore larvae compared to 90±3% of the control (non-irradiated) embryos in the absence of dextrans or PI for n=3 experiments with an average of 50 embryos (Fig. 6.11). Properly developed trochophore larvae were determined by fixing the samples in 4% paraformaldehyde solution and then checking each irradiated larva based on a normal body plan as described in literature [180]. Furthermore, an individual blastomere optoinjected at 2-cell stage with a 3 kDa dextran dye could survive the procedure and carried on dividing into smaller cells which carried the optoinjected dye (see Fig. 6.10(E)). A mosaic pattern of tagged cells was typically observed demonstrating that the optoinjected blastomere remained viable and the injected dye had been passed on to daughter cells. This shows that the proposed technique may be used for cell-lineage mapping both at early and late stages of embryo development.

6.6 Optical trapping and orientation of P. lamarckii embryos

Holding and orientation of embryos are useful for the purposes of sorting prior fertilization. Embryos are complex biological systems. As they developed, there are interesting features which would be important to observe using high-resolution microscopy which often requires the sample to sit close to a high NA objective. In practice, holding and orientation of embryos are performed using large microcapillary pippettes which disturb the environment of the sample. Hence, an optical approach to orient an embryo would bring an advantage as this would permit simultaneous manipulation and observation in a close, aseptic system. Thus, the same holographic system can be used to optically orient and move a developing embryo.

For this experiment the Ti:sapphire laser was switched to CW operation at 800 nm. Previously, clonal growth studies of trapped CHO-K1 cells showed that optical trapping with laser wavelength of 800 nm is significantly less toxic for mammalian cells than the conventionally used trapping lasers with wavelength of 1064 nm [170]. Hence, optical orientation and trapping at this wavelength would be more suitable to avoid loss of viability of the embryos. For the optical trapping experiments, the objective was switched to $\times 20$, 0.5 NA objective (Nikon). Using a low NA objective offers flexible orientation with a wider field of view and longer working distance compared to high NA objectives often used in optical tweezers. This wider range of space is especially important in optical manipulation of large macroscopic samples. The holographic system developed was used to dynamically translate the focal spot and laterally position the individual embryos. The system permits fast and accurate positioning and orienting of a single embryo in three dimensions.

With the weakly focused beam used for this experiment, the axial scattering force would be expected to be dominant over the axial gradient force on the embryos. The scattering force will push the embryo along its propagation axis. For the optical trapping experiments, single-cell zygotes of *P. lamarckii* were utilised which is more uniform in structure and shape compared to later developed embryos. Indeed, the weakly focused single beam at a P= 130 mW could levitate the embryos above the bottom of the dish. Furthermore, by slight adjustment of the focusing of the beam performed by wavefront modulation using the SLM, a stable position of the optically trapped embryo can be found, in which the summative scattering force and the buoyant force can balance gravity at a given height (Fig. 6.12(A)). Changing the degree of focusing of the beam, modulates the collimation of the beam incident to the objective and the position of the focus, allowing the confinement of the embryo in the axial direction. At the same time, the embryos were confined in the lateral

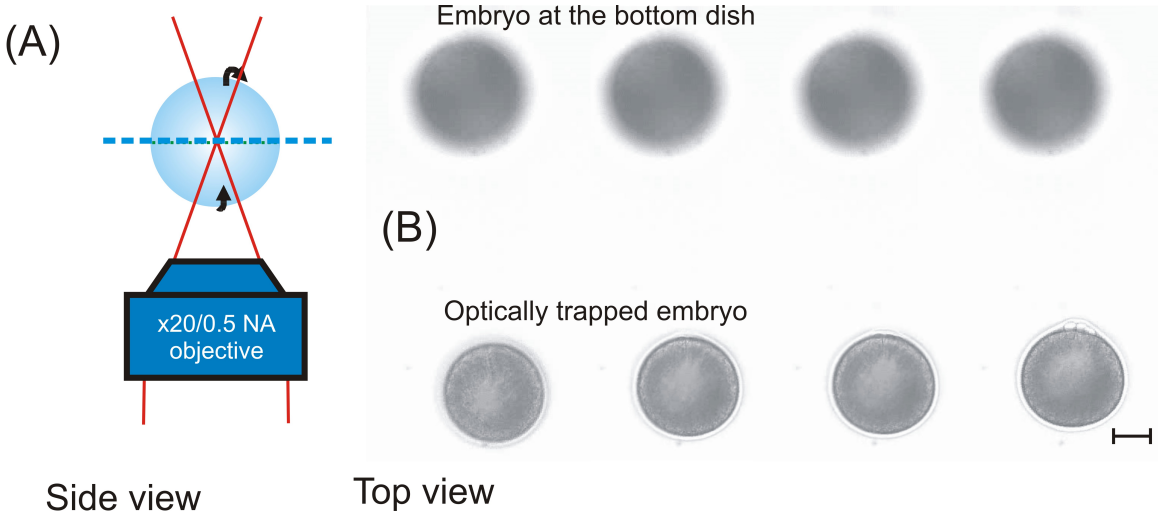

Figure 6.12: Single beam optical trap of a *P. lamarckii* embryo. (A) Schematic layout of the optical trap and arrows indicating direction of rotation. (B) Movie stills of optical trapping of embryo using a single beam optical trap (Media 3). Scale bar corresponds to 20 μm [204].

plane resulting in a full three dimensional trapping. A gradual change of the phase modulation on the SLM could translate the trap in three dimensions resulting in a controlled movement of the embryo.

Interestingly, in this single beam configuration, the beam can also induced an optical torque on the embryo causing it to rotate perpendicular to the propagation axis of the beam (Fig. 6.12(B), Media 3). The rotation can be attributed to the embryo's inhomogeneity and the mismatch between the position of the beam focus and the centre of mass of the embryo. Optical rotation of single cells has been also demonstrated in a dual beam fibre trap [206]. However, there is still an advantage on using single beam configuration over dual beam fibre trap, as the former removes the necessity of the difficult alignment of the fibres in the sample chamber. The rotation effect of the single beam configuration on optically trapped embryos may be useful for future experiments involving simultaneous manipulation and long-term imaging studies of embryos. which requires it to be oriented either at its animal or vegetal pole position. Furthermore, optical orientation allows immediate access and subsequent optoinjection of molecules into specific features in a developed embryo, for example the blastopore lip which forms the mouth and anus.

In situations, when an ideal orientation is already found, the rotation of the optically trapped embryo must be stopped in order to fix its position. In order to perform this, a more advanced approach was employed, in which a reconfigurable

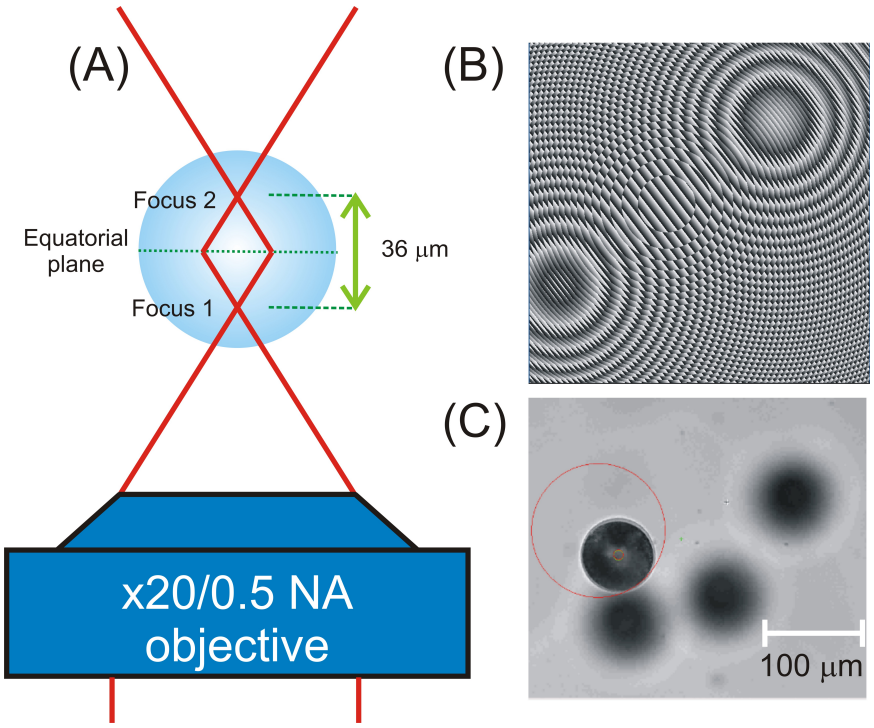

Figure 6.13: (A) Schematic illustration of the dual beam trap on a 1-cell *P. lamarckii* embryo. The dual focus trap was created by encoding a CGH on the SLM shown on (B). Stable trapping without rotation was achieved at a height of 190 μm when the two foci were separated 36 μm apart. In this configuration, an embryo can be optically trapped 190 μm above the glass bottom dish (Media 4). (C) An image of a single embryo stably trapped above the dish and the defocused image of embryos at the bottom of the petri dish [204].

dual focus trap was symmetrically positioned along the z-axis of the embryo. In this approach, stable trapping can be achieved at a height of up to 200 μm above the bottom of the dish, without rotation. Fig. 6.13(A) shows the schematic illustration of the dual beam trap configuration. At 190 μm above the bottom of the dish, the most stable configuration was found when two overlapping foci were axially separated by 36 μm. The holographic system enabled dynamic adjustment of the hologram, allowing optimisation of the locations of the two foci within the embryo and consequently providing the most stable trapping. An example of the phase profile displayed in the SLM for stable optical trapping of the embryo is shown in Fig. 6.13(B). Using a total laser power of about 175 mW with power equally divided into the two foci, a single embryo can be optically trapped 190 μm above the glass bottom dish as shown in Fig. 6.13(C). With these parameters, the measured escape

speed, defined as the speed at which the embryo drops out of the optical trap is 20±2 μm/s. A similar configuration was recently demonstrated to trap large motile specimens [164]. In their approach, the dual focus was spaced 100 μm apart and a counter-propagating trap was formed by introducing a reflecting mirror. In this configuration, the specimens were trapped in between the two foci, where the scattering force of the two counter-propagating beam cancels.

However, an important aspect in this optical approach is maintaining the viability of the trapped embryo. Previous work on optical trapping performed at 1064 nm conducted in water showed that a temperature increase of 1^oC is expected per 100 mW trapping power [171]. As the parameters presented in this work are within this range and water has substantially lower absorption at 800 nm than at 1064 nm, the local temperature increase should not be detrimental to the optically trapped embryos survival. Indeed, optical trapping of single-cell *P. lamarckii* embryos for 10 min did not induce visible morphological changes and the embryos carried on to subsequent division.

6.7 Conclusion and Future Work

In summary, a combined optical approach for the manipulation of living and developing embryos was presented. The proposed holographic optoinjection and trapping system facilitates a computer-controlled optical handling and time-sequenced laser dosage of embryos paving the way towards automated high-throughput processing. With the newly developed fs holographic system for cell transfection and optical injection (see Chapter 5), a computer-controlled time-sequenced laser dosage of an embryo is possible with a potential for automated high-throughput manipulation. The system enabled selective optoinjection into the blastomere of an embryo. In addition, the same system can be utilised for the optical trapping, moving and orientation of embryos. In this chapter, experiments were performed on *P. lamarckii* embryos, a newly emerging developmental biology species.

Prior optoinjection experiments, the optimal temperature were obtained at which the embryos will develop properly. It was found that 85% of the embryos properly developed into trochophore larvae when the environmental temperature was maintained at 14-18^{o}C. After optimising the temperature conditions to obtain a high percentage of viable embryos, optoinjection was performed on 2-cell and 4-cell stage embryos. Successful optoinjection of dextran molecules of a variety of sizes from 3–500 kDa was achieved in this chapter. Furthermore, using an NIR fs laser, optoinjection into the deep layers of the *P. lamarckii* embryos was demonstrated while maintaining the integrity of the cells in the beam path. This is unique to optoinjection technique, as the more conventional microinjection will lead to piercing and damaging of cells in the capillary injection path.

The efficiency of the technique was determined by optoinjecting the embryos in seawater with PI at different stages of its development using P= 60 mW and T= 30 ms delivered at three different dosage points on the blastomere. It was found that the efficiency of injection is between 44–55%. The creation of small to medium sized gas bubbles on the blastomere surface was found to be necessary in order to obtain a detectable fluorescence signal. With increasing depth from the surface of the embryo, the energy required to generate a gas bubble increases which was attributed to increase spherical aberration as well as scattering from the embryo tissue.

The size of the gas bubble was found to be correlated to leakage of intracellular contents of individual blastomeres. As the leakage resulted to improperly developed embryos, parameters were studied at which different sizes of gas bubbles, grouped according to small (<1 μm), medium (2–5 μm) and large (>5 μm) can be obtained. With the combination of laser parameters, P$\geq$ 78 mW and T$\geq$ 10 ms, mostly medium to large gas bubbles were obtained. This combination of power and exposure

time should be avoided and lower P and T setting should be used in order to obtain viably optoinjected embryos that will develop into proper larvae. In the absence of PI or dextran, using laser parameters P= 60 mW and T= 30 ms, 46% of irradiated embryos developed into proper larvae. Furthermore, irradiated blastomeres with a gas bubble of less than 5 μm in size created on its surface will carry on dividing as confirmed by time-lapse imaging over an hour after irradiation.

Furthermore, the same system can be utilised for optical orientation and trapping of individual *P. lamarckii* embryos. The Ti:sapphire laser was switched to its continuous mode and the 800 nm CW laser beam was coupled into a $\times$20, 0.5 NA objective. With this approach, a single beam can levitate an embryo and with the holographic system, the wavefront of the beam can be modulated in order to perform stable trapping in three dimensions. In this configuration, the beam induces a torque on the embryo which leads to its rotation. Using an overlapping but axially separated foci, the rotation of the embryo can be stopped and a stable trapping can be achieved.

With this technology, future work involves optical transfection of this species of embryos with other genetic materials such as double stranded DNA, messenger RNA and iRNA. Preliminary experiments were performed on optically transfecting these embryos with DNA plasmid encoding for GFP. However, treated embryos have arrested development and transfection was found to be unsuccessful. The parameters used for transfection were found not to be detrimental to the embryos and their improper development maybe due to the incompatible cytomegalovirus promoter used in the GFP plasmid. At present, the injection of exogenous gene constructs for this species has not been well established and suitable promoter to drive protein expression are unknown. Recently, protein expression using *in vitro* synthesized capped mRNA using commercially available plasmid constructs was shown in *L.stagnalis via* microinjection [207]. It would be interesting to determine if *in vivo* expression is possible using these reported constructs and perform genetic modification to produce *P.lamarckii* transgenic animals. Similarly, optoinjection of fluorescently labelled dyes into single blastomeres of these developing embryos would enable one to investigate fate mapping and the lineage of individual embryonic cells.

Such development of optical techniques for the delivery and orientation of the developing embryo of this species would benefit the field of developmental biology. This optoinjection approach is particularly suited to perform delivery of molecules into species with small embryos that are hard to handle with more conventional microinjection techniques. Furthermore, optical trapping of an embryo would aid in orientation for long term imaging and observation to follow its development. The field of developmental biology may benefit greatly from the development of robust

all-optical techniques for injection, gene transfection and manipulation of embryos, such as these presented above.

In the following chapter, instead of targeting single cells using CW and fs laser sources for optical injection and transfection, I will demonstrate a controllable laser induced breakdown process by the breakdown of optically trapped microspheres using pulsed ns lasers. The advantage of this technique is its limited region of cell death and high post-treatment viability over other ns laser based optoporation techniques, discussed in Chapter 3.

Part of this work was published in Biomedical Optics Express, **2**, 2011 [204].

7

Cell transfection by laser induced breakdown (LIB) of an optically confined microsphere

In contrast to previous chapters, in which the tightly focused laser directly irradiates the cell, in this chapter, a different methodology will be presented for cell transfection. Optoporation techniques described previously in Chapter 3 focused a ns laser beam onto the buffer medium or the glass cover slip where the cells are attached. The mechanical effects associated with the breakdown of medium and glass interacts with the cell monolayer leading to membrane permeabilisation. However, due to the large energy deposited on the sample, a large zone of cell death is created. Hence, by using an optically trapped microsphere as a seed for the breakdown, an optimised membrane permeabilisation and controllable mechanical effects of the breakdown with minimum cell death will be demonstrated.

7.1 Introduction

In previous chapters, targeted single cell optical injection and transfection techniques was described using tightly focused CW violet diode and NIR fs lasers. In contrast, multiple cells are targeted using pulsed ns lasers techniques as described in Chapter

3. Due to the associated mechanical side effects of the interaction of long pulsed ns laser sources with the sample, treatment of cells is often non-localised, treating large population of cells at a time.

The mechanical effects scale with the amount of energy deposited to achieve the LIB threshold. The breakdown of material induced by ns laser pulses can be violent with the generation of plasma followed by shock wave propagation as well as formation of fast gas filled bubbles called cavitation bubbles. The expansion of cavitation bubbles is responsible for the loss of viability of the surrounding cells leading to cell detachment, late apoptosis and necrosis. Cavitation bubble expansion causes cellular lysis and detachment due to the impact of shear stress by the expanding cavitation bubble wall [32].

Although the energetic pulses are favourable for large scale effects for some biological applications, their application to targeted optical transfection is limited due to the amount of energy it deposits to the sample. It has been shown that the LIB in the presence of confluent cells induces a large zone of cell lysis due to the high breakdown threshold of absorptive medium such as buffer medium [32, 30] and glass silica coverslip [28]. This results in a large cavitation bubble of hundreds of microns in size, which reduces the overall cellular viability. This is a drawback to transfection of cells which requires small and transient disruptions on the cell membrane in order to maintain cell viability. Thus, a controllable cavitation of LIB and its mechanical effects is desirable as it would provide a more flexible ns laser based optical transfection device *i.e.* a single system could be utilised for both targeted single cell transfection and large scale treatment of multiple cells.

Hence, in this chapter, instead of inducing breakdown on a glass coverslip or in buffer medium, the breakdown of a single micron-sized microsphere was implemented in the presence of a cell monolayer. Optical tweezers allow the confinement and positioning of micro- and nano-particles at a desired location within the buffer medium. A single microsphere can be confined and positioned spatially and axially over a monolayer of cells. The axial positioning can control the extent of mechanical effects. Furthermore, the breakdown threshold can be manipulated by changing the microsphere material. Changing the size of the microsphere will influence the size of the cavitation bubble and the subsequent hydrodynamic flow of fluid over the cell monolayer. Therefore, employing optical tweezers with LIB would provide additional degrees of freedom such as the microsphere material, its size, and the LIB position relative to the cell monolayer. In this chapter, these additional parameters were demonstrated to offer a method to minimise the energy required for controllable cavitation, leading to the permeabilisation and transfection of Mito-DsRed plasmid to mammalian cells in a targeted area, while reducing cell lysis.

This work was performed in collaboration Dr.Yoshihiko Arita (Postdoctoral researcher, University of St. Andrews). The optical tweezers system described here was built and characterised by Dr. Woei Ming Lee (former Research Associate, Optical Trapping Group) as an independent PhD project. The author performed all the transfection experiments and analysis presented in this chapter.

7.2 Events during LIB of a microsphere in an optical trap

For the fundamental concepts of LIB, the reader is referred to Chapter 3. With pulsed ns laser sources, the LIB is accompanied by plasma formation, breakdown of material, followed by a series of events that may affect the surrounding cells or tissue material. It is assumed that a single cavitation bubble, centred on the site of the LIB of a microsphere, is initiated in the same manner as LIB of a liquid. In this section, I will discuss the events during the LIB of a microsphere based on previous investigations of LIB in water. An excellent review article on the concepts of LIB in aqueous media was written by Kennedy *et al.* [101].

Fig. 7.1 shows a schematic diagram of the events occurring during LIB of an optically trapped microsphere. The concept of optical tweezers was discussed in Chapter 6. A single optically trapped microsphere is exposed to a tightly focused ns laser. The critical breakdown threshold intensity is achieved at the focus of the laser leading to the breakdown of the particle. Among the commercially available microsphere materials, polymer has relatively low breakdown threshold of 0.7 GW/mm^2 [208]. The breakdown of a particle is accompanied by the formation, ultrafast growth and decay of a plasma which occurs in the order of ns time-scale [209, 116]. Its expansion would generate a pressure wave which propagates radially away from the breakdown site [210]. The pressure wave initially travels at hypersonic speed but as it expands and loses energy, its speed would approach the speed of sound.

In the vicinity of the plasma, the vaporised material will have a very high temperature and pressure. However, the thermal and pressure effects of the plasma are localised within its volume and most of the energy is converted to the mechanical effects of the breakdown [101]. Apart from the plasma, the subsidiary mechanical effects such as cavitation bubble expansion generate the most damage to the surrounding medium after the breakdown [32, 30]. The cavitation bubble expands, pushing material away until it reaches its maximum bubble size. Cells encountering the expanding cavitation bubble wall experience shear stress. When the pressure inside the bubble reaches the saturation pressure of the liquid, it will rapidly collapse, occuring $\approx$10 μs after the breakdown. Aside from cavitation bubble expansion,

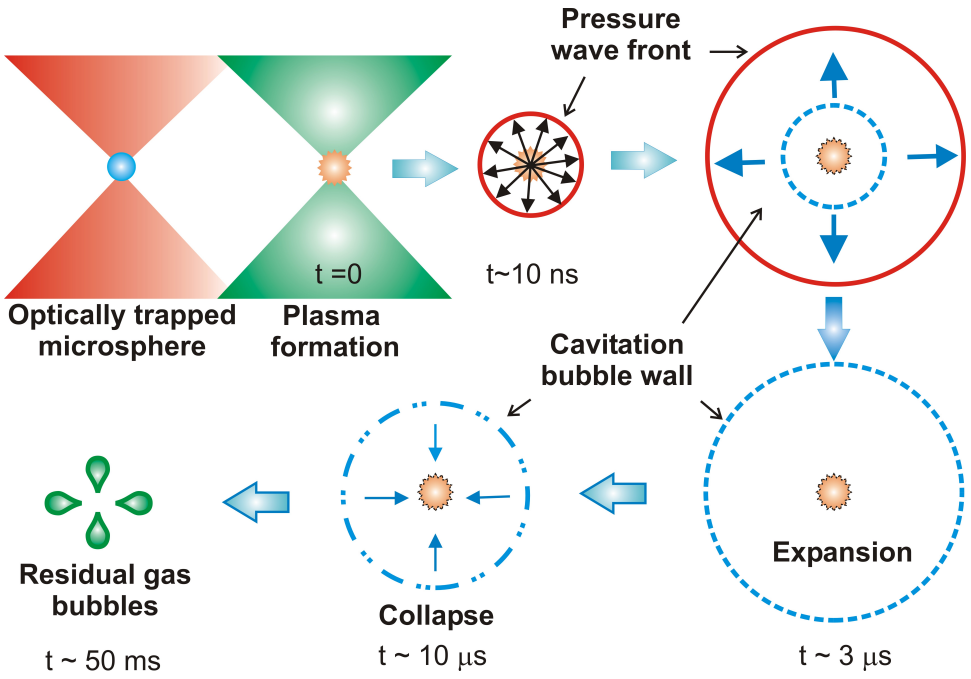

Figure 7.1: A schematic diagram of the time-series evolution of laser induced breakdown of optically trapped microsphere. An optically trapped microsphere is irradiated with a laser leading to its breakdown and vaporisation. A plasma is formed accompanied by pressure wave and cavitation bubble expansion. Several ms after the breakdown event, residual gas bubbles are formed. Approximate time for each event after breakdown are specified based on values given in reference [32].

its subsequent collapse may also affect the integrity of surrounding cells and tissue around the breakdown site [211]. Depending on its distance from a solid boundary, the cavitation bubble may interact with the substrate leading to formation of liquid jets, counterjets and secondary gas bubbles. Its growth and jet formation is dictated by two parameters, the distance, D, between the center of the bubble to the substrate and its maximum bubble radius, R_B giving an expression for the standoff distance, γ,

$$\gamma = \frac{D}{R_B} \tag{7.1}$$

At $\gamma < 1$, or $R_B > D$, the cavitation bubble wall is in contact with the bottom substrate and the bubble is inhibited to form a spherical shape. During its collapse, the bubble will become elongated and a jet formed within it will be directed towards the surface boundary. Meanwhile, for $\gamma > 1$, in addition to jet formation, a counterjet is also generated which rebounds away from the boundary. The jet impact to the

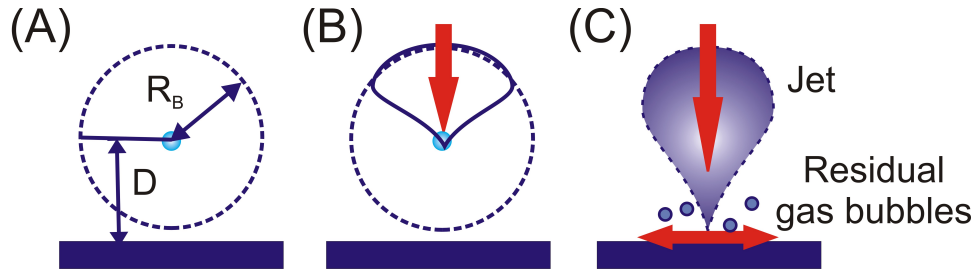

Figure 7.2: Schematic illustration of possible events during the collapse of a cavitation bubble generated during microsphere LIB. (A) Concept for cavitation bubble formation after microsphere LIB. (B) Subsequent asymmetric collapse with jet involution. (C) Toroidal bubble formation once jet moves along bubble volume. This is generated with a radial flow along substrate plane followed by the formation of secondary bubbles which are presumed to interact with the substrate by themselves jetting towards the surface [211].

substrate gives rise to a high pressure which may damage the surface [212].

A schematic illustration of the collapse of a cavitation bubble generated during microsphere LIB is shown in Fig. 7.2 (A). The experiments that will be presented in this chapter have the position of the LIB in close proximity to the cell substrate (0–25 μm), hence, we may assume that $\gamma < 1$. In such a case, an asymmetric collapse accompanied by jet involution occurs (Fig. 7.2(B)). This is followed by a toroidal bubble formation accompanied by radial flow along the substrate and collapse of many tiny bubbles or secondary bubbles (Fig. 7.2(C)). The collapse of these tiny bubbles have been implicated in formation of damage pits in solid substrates [211].

7.3 Experimental Design

Fig. 7.3 shows a schematic diagram of the experimental setup. The optical tweezers system was built on an inverted microscope system (Nikon TE2000). A CW fibre laser (IPG Laser GmbH, YLM-5-1070-LP) operating at 1070 nm was utilised for the optical tweezers. The output laser beam was directed to a polarising beam splitter and half wave plate to control the laser power. A laser power of 200 mW was utilised to optically trapped individual microspheres for all the breakdown experiments. Lenses L1 and L2 expand the laser beam 3×. L2 was attached to a stepper motor (SM, LS series, Zaber technology) to change its position and consequently the divergence of the beam, thereby changing the axial position of the laser trap within the sample. M1 and M2 form a periscope system to elevate the height of the beam and direct it on the upper fluorescence port of the microscope system. L3 and L4 (f_3 and f_4= 100 mm) form a beam steering system that ensures the beam will not

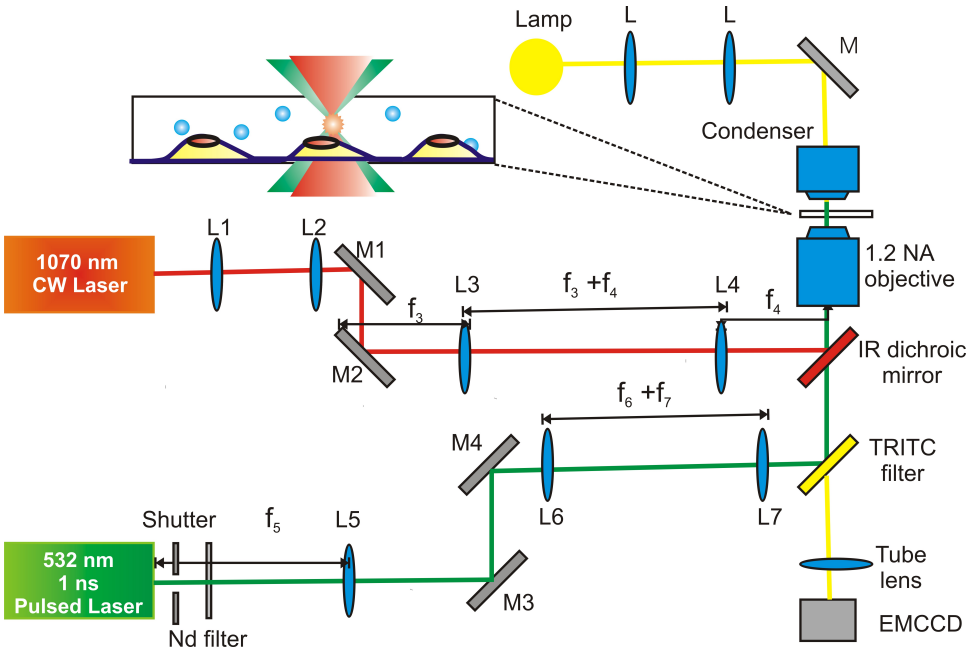

Figure 7.3: Setup of an optical tweezers combined with pulsed ns laser for laser induced breakdown. L-lenses, M-mirrors. Periscope pairs, M1 and M2, M3 and M4 spatially aligned the 1070 nm beam and the 532 nm. L2 is attached to a stepper motor to adjust the axial positioning of the optical tweezers and axially align it with the 532 nm beam. Lenses have focal lengths, f_3 and f_4= 100 mm, f_5= 350 mm, f_6 and f_7= 50 mm.

walk off from the back aperture of the oil immersion objective (Nikon, Eplan,100×, NA:1.25). A NIR dichroic mirror (DM, Chroma, z900dcp) reflects the tweezing laser beam into the backaperture of the objective.

LIB was induced using a pulsed Q-switched Nd:YAG laser (Elforlight, SPOT). It has a fundamental wavelength of 1064 nm with 1 ns pulse width running at 1 kHz repetition rate and with pulse energy of 1 μJ. A potassium dideuterium phosphate (KD*P) crystal is used to double the frequency of the laser output thereby producing a laser beam with a wavelength centred at 532 nm. The diverging beam from the ns laser was collimated using a single lens, L5 (f_5= 350 mm) positioned 350 mm from the KD*P crystal. A mechanical shutter (Newport, UK model 845 HP-02) controlled the exposure of the laser to 40 ms (40 pulses). A neutral density filter (Nd filter) was incorporated in the beam path to control the laser power. M3 and M4 formed a second periscope to direct the ns laser to the lower fluorescence port. Lenses L6 and L7 (f_6 and f_7= 50 mm) formed a beam steering lens system. A tetramethylrhodamine isothiocyanate filter (TRITC, Nikon, excitation filter: 530-560 nm) was used to deflect the ns laser beam to the backaperture of the microscope

objective.

The lasers used for optical tweezers and LIB were co-aligned axially within the sample by adjusting L2 position to control the divergence of the tweezing laser. Meanwhile, the lateral beam alignment was performed by moving either mirror M2 and M4 to position the optical tweezers or the ns laser beam. The optical tweezers and the breakdown of the microsphere was imaged and recorded using an EMCCD camera (Andor, iXonEM+885, frame rate= 31.23 Hz). LIB of a single polymer microsphere with sizes of 0.4–2.0 μm was performed when the tweezing and the ns laser were perfectly co-aligned.

The axial position of the trapped microsphere was evaluated by trapping a single microsphere and axially moving the trap towards the bottom of the dish. When the sphere was in contact with the dish bottom and subsequently released from the trap, this axial position was set as z= 0. Based on this calibration, the trap was positioned at specific axial locations. Polymer microsphere size as small as 0.2 μm can be optically trapped using the system, however, it was difficult to obtain single microspheres at this size as they often formed aggregates. A single microsphere was optically trapped and exposed to the pulsed ns laser for 40 ms to induce its breakdown.

7.4 Materials and Methodology

7.4.1 Sample preparation

CHO-K1 and HEK293 cells were utilised for the experiments in this Chapter. Cell culture methods are discussed in Appendix 9.1. The polymer microsphere suspension (Thermo Scientific) of sizes 0.4, 0.5, 0.7, 1.0 and 2.0 μm were diluted in OptiMEM (Invitrogen) to yield concentrations of 1:1000 (0.4, 0.5, 0.7, 1.0 μm) and 1:50 (2.0 μm). Prior to experiments, microspheres were spun at low speed to prevent aggregation of particles. Diluted microspheres with a volume of 100 μL were aliquoted ino microcentrifuge tubes containing 0.55 μL of 1.88 μg/mL stock Mito-DsRed plasmid to obtain a final DNA concentration of 10 μg/mL. Cells were washed twice with OptiMEM to remove residual fetal calf serum on the CHO-K1 monolayer. 60 μL of mixed microspheres and Mito-dsRed plasmid DNA solution were added to the cells. A Type 0 coverslip was floated on top of the solution to maintain sterility.

7.4.2 Cell transfection protocol

For each prepared sample, 10 individual microspheres with the same size (0.4 μm–2.0 μm in diameter) were targeted at different lateral positions at specific axial

location (5–25 μm) above the bottom of the dish. A single microsphere was optically trapped and axially positioned up to 25 μm above the glass dish. The pulsed ns laser with a power of 1 mW (measured at the back aperture of the objective) was introduced to the system with the opening of the mechanical shutter. The microsphere was exposed to the pulsed ns laser for 40 ms, during which time subsequent breakdown and formation of gas bubbles were observed. To obtain reliable statistics, a minimum of 3 samples (n= 3) were treated for each axial position and microsphere size. In a similar manner, a control sample were exposed to both the optical tweezers and the pulsed ns laser with 0.5 μm microspheres in the buffer medium but without trapping any microsphere and inducing LIB. After treatment, the cell monolayer was washed twice with OptiMEM to remove residual DNA plasmids and microspheres. Fresh culture medium was added to the cells and dishes were incubated at 37^{o}C and 5% CO_2. After 48 h of incubation, cells expressing mitochondrial targeted Mito-DsRed protein were counted under fluorescence microscope.

7.5 Results and Discussions

In this section, the results of LIB of a microsphere in water will be presented and a description of the vaporisation of the microsphere and the presence of residual bubbles after the breakdown. Then, the events following the LIB of a microsphere on top of a cell monolayer is described and subsequently the effect of changing the microsphere size on the number of cells affected after the breakdown. Finally, successful cell transfection will be demonstrated using this technique.

7.5.1 LIB of an optically trapped microsphere

Videos of LIB of various sized microsphere both in water and in the presence of CHO-K1 monolayer were acquired. From the videos, individual frames were obtained, depicting events during and after the breakdown. A video processing software called *Virtualdub* was utilised to acquire the frames saved as *tiff* files. The pixel size of each image was calibrated using a microscope graticule. Measurements within each image were performed using *ImageJ*.

LIB of an optically trapped microsphere was observed in deionised water. Fig. 7.4 shows the consecutive frames of a video with a single 0.5 μm sphere and its subsequent breakdown after irradiation with a 1 mW pulsed ns laser. The fastest acquisition of the camera is limited by its frame rate which is set at 30 frames per second; hence, the temporal resolution of the system is $\approx$ 30 ms. Fig. 7.4(A) shows an optically trapped microsphere, axially positioned at 10 μm from the surface.

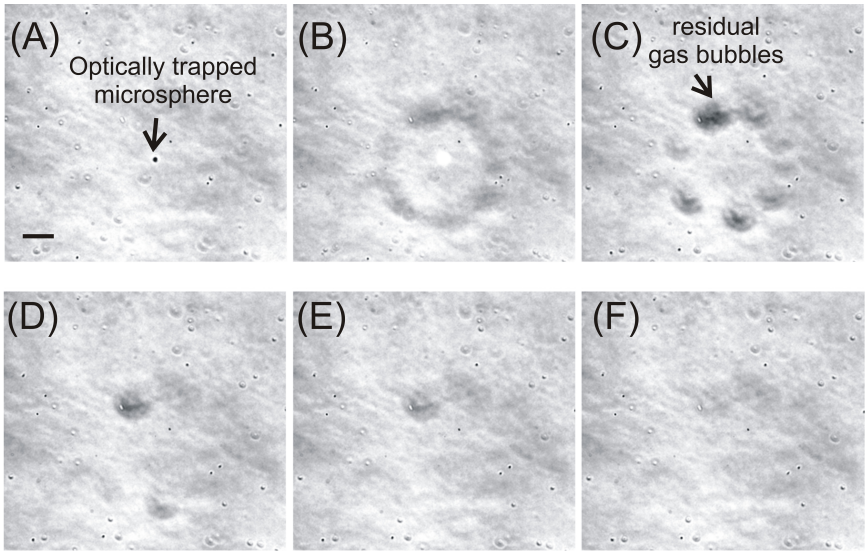

Figure 7.4: Individual frames showing laser-induced breakdown of optically trapped microsphere in water. (A)-(F) are consecutive snapshots of a video showing: (A) an optically confined 0.5 μm sphere, 10μm above the glass bottom; (B) the introduction of the pulsed ns laser with a 35 μm diameter shadow surrounding the sphere; (C) absence of the sphere and formation of gas bubbles; (D)–(F) and one by one collapse of the gas bubbles. Scale bar corresponds to 10 μm.

When the pulsed ns laser was introduced to the system, a bright flash of light was observed where the sphere was originally located (Fig. 7.4(B)). The microsphere was immediately vaporised with the introduction of the pulsed ns laser as depicted by its absence in the succeeding frames of the video. A ring-shaped shadow can be observed in Fig. 7.4(B) which has a radius, r= 17.5 μm. Fig. 7.4(C) shows the collapse of this shadow into discrete structures, which can be referred to as residual gas bubbles. These gas bubbles collapsed independently as shown in Fig. 7.4(E-F). Similar experiments were also performed with larger microsphere sizes, 1.0 and 2.0 μm. The diameter of the ring of residual gas bubble was found to increase with increasing microsphere size.

The full extent of the LIB event can only be temporally resolved by stroboscopic illumination or high-speed imaging using a fast camera with frame rates of kHz or more. Therefore, ultra-fast events such as shock wave formation and cavitation bubble expansion and collapse after the breakdown cannot be fully resolved using our current system. However, the acquired frames in the videos confirm the breakdown of microsphere as a result of LIB.

In the presence of a confluent cell monolayer, the breakdown of a microsphere

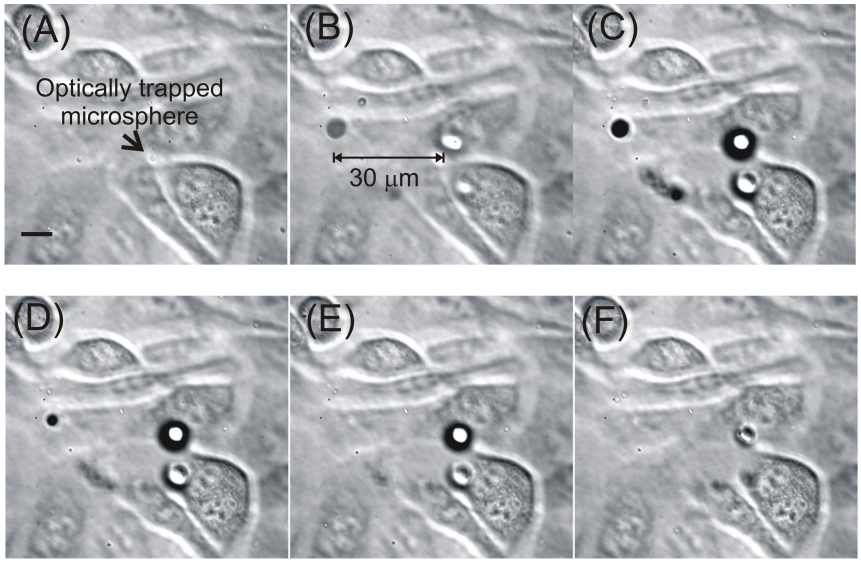

Figure 7.5: Individual frames of laser-induced breakdown of an optically confined 0.5 μm microspheres on top of a CHO-K1 cell monolayer. (A)–(F) are consecutive snapshots of a video showing: (A) optically trapped microsphere situated 10 μm from the cell substrate; (B) shows the introduction of the pulsed ns laser and a single bubble formed; (C) shows the formation of more gas bubbles; ((D)–(F)) depicts their independent collapse. Scale bar corresponds to 10 μm.

using a pulsed ns laser resulted in a region of cell necrosis. Fig. 7.5 shows consecutive frames of the breakdown of a 0.5 μm microsphere on top of a CHO-K1 cell monolayer. After the breakdown, gas bubbles were seen to be initiated from the site of irradiation and travelled radially outwards with a maximum distance of 30 μm. Cells were displaced and pushed away from the breakdown site resulting in deformation of some of the cells (Fig. 7.5(C)). Notably, a clearance zone is repeatedly observed surrounding the breakdown site. It can be assumed that the clearance zone occurs due to the shear stress imposed by cavitation bubble expansion.

Next, the size of the clearance zone created surrounding the breakdown site as a function of the microsphere size was investigated. The clearance zone could be indicative of the amount of shear stress on the cell due to the cavitation bubble expansion. Hence, individual microspheres of sizes 0.5, 1.0 and 2.0 μm were targeted with the pulsed ns laser in the presence of cells. Fig. 7.6 shows the clearance zone for sphere sizes, 0.5 μm and 2.0 μm. The clearance zone increases with microsphere size. Beside the clearance zone, several cells surrounding the breakdown site exhibit necrotic signatures such as granulated cytoplasm and pronounced nuclei. Other cells

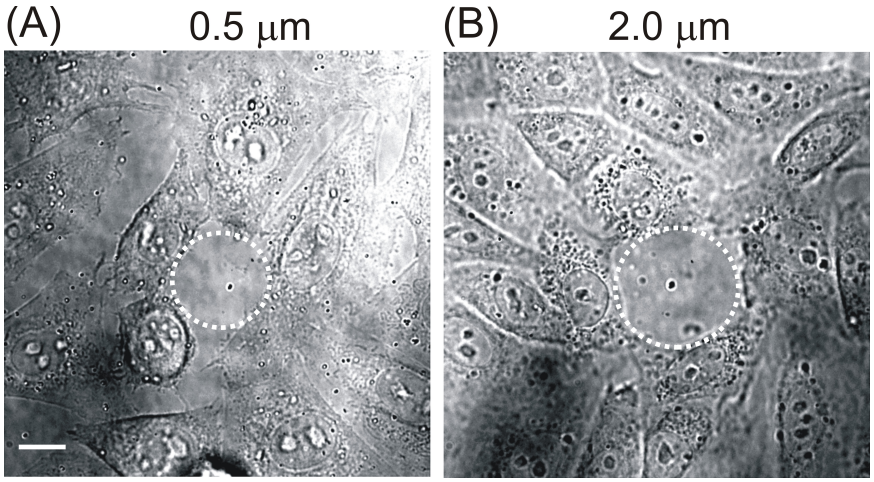

Figure 7.6: Clearance zone due to breakdown of microsphere of sizes (A) 0.5 μm (B) 2.0 μm. Scale bar corresponds to 10 μm.

Table 7.1: Summary of clearance zone at breakdown of different microsphere sizes

Microsphere size (μm)	Diameter of clearance zone (μm)	Affected cells
0.5	21.3±1.0	4±2
1.0	27.6±1.5	4±1
2.0	31.3±2.5	6±0

were compressed with the fluid flow during breakdown and were displaced away from the breakdown site but did not exhibit drastic morphological changes.

It was observed that the breakdown of a 0.5 μm microsphere size provided the smallest clearance area with diameter of 21 μm. Furthermore, the shear stress accompanying LIB of 0.5 μm microsphere did not result in major morphological changes of the surrounding cells (Fig. 7.6(A)). However, the breakdown of larger microspheres, 1.0 μm and 2.0 μm, resulted in a larger clearance zone and irreversible drastic morphological changes on the surrounding cells (Fig. 7.6(B)). A summary of the clearance zone diameter measured for n= 3 samples and the number of affected cells is shown in Table 7.1. The LIB of 1.0 μm and 2.0 μm microspheres resulted in a clearance zone diameter of 28 μm and 31 μm, respectively. For all the microsphere sizes used in this study, the region of affected area is confined to the cells right beside the clearance zone.

Previous independent studies on the LIB of buffer medium in the presence of cell monolayer have shown that the size of cavitation bubble is proportional to the radius of lysed cells [30]. Hence, it can be assumed that increasing the microsphere size

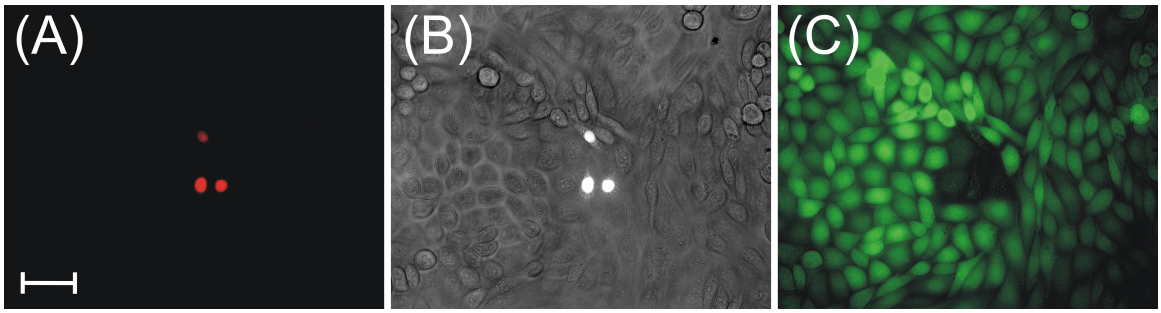

Figure 7.7: (A) Fluorescence image of LIB of cells with Propidium iodide (B) Brightfield image showing cells that have been affected during LIB (C) Fluorescence image of cells with Calcein AM, showing cells which are not viable. Scale bar corresponds to 50 μm.

constitutes to a larger vapour material and plasma leading to increased cavitation bubble size produced during the breakdown. Since a larger cavitation bubble would imply a higher maximum shear stress [32], the breakdown of 1.0 and 2.0 μm microspheres resulted in larger magnitude of shear stress compared to smaller 0.5 μm microsphere.

In order to determine the state of viability of the surrounding cells around the breakdown site, cells were incubated in 3 μM CAM for 15 min before LIB. After which, cells were washed twice with fresh OptiMEM and then bathed in 3 μM PI during the LIB of 0.5 μm microsphere. In this experiment, PI and CAM were used to determine the number of necrotic cells within the vicinity of the breakdown. Fig. 7.7(A) shows a typical fluorescence image of cells after LIB of 0.5 μm microsphere. Three cells at the centre of the site of breakdown are brightly stained with PI at the nucleus. These cells are necrotic as confirmed by the absence of CAM signal (Fig. 7.7(C)). Meanwhile, surrounding cells away from the irradiated region, at a distance greater than 40 μm away from the breakdown were visibly not affected and remained viable during the breakdown as shown in Fig. 7.7(B) and confirmed by both PI and CAM fluorescence images. This can be explained by the radially decreasing impact of shear stress induced by the cavitation bubble. Similar results were obtained by [28] and [30] wherein beyond a certain radial distance from the breakdown, cells were unaffected and were not compromised by LIB. From these observations, by using an optically trapped polymer microsphere for LIB, the region of cell lysis was demonstrated to be limited and controlled, localising the affected region. Furthermore, the size of microsphere is an important parameter in the level of shear stress experienced by the cell during LIB.

7.5.2 Cell transfection by LIB of an optically trapped microsphere

Cell transfection of Mito-DsRed encoding plasmid into HEK293 and CHO-K1 cells was performed by LIB of optically trapped microspheres. Fig. 7.8(a) shows a bright-field image of HEK293 cells using ×20 objective. LIB was induced in 4 different spatial regions marked by x. Its corresponding fluorescence image shown in Fig. 7.8(b) depicts the cells transfected for each breakdown site. Two to four cells were found to be expressing the Mito-DsRed protein for each breakdown site, 48 h after transfection. A closer view on these transfected cells is shown in Fig. 7.8(c) and (d). Fluorescence image of transfected CHO-K1 cells is shown in Fig. 7.8(e). It can be seen that cells transfected form small colonies surrounding the blasted region. Notably, similar to transfection using CW and fs laser, both HEK293 and CHO-K1 cell lines can be transfected and the technique seem to have no bias on the cell lines to be transfected.

The number of CHO-K1 cells transfected was evaluated as a function of the polymer sphere size, and its axial location from 5 to 25 μm measured from the bottom of the dish, whilst using a fixed laser power of 1 mW at 1 kHz. In each dish, 10 individual microspheres with the same size (0.4–2.0 μm in diameter) were targeted and at a fixed axial position at 10 μm. LIB of individual microspheres was situated $\approx$ 100 μm apart from each of the LIB site. Fig. 7.9 (A) shows the number of transfected cells with LIB as a function of microsphere size. 0.5 μm microsphere was found to be the optimal size for LIB at 10 μm axial position providing a level of shear stress that will induce successful transient permeabilisation on surrounding cells. The maximum number of transfected cells in a dish was $\approx$ 30 with an average of 3 transfected cells at each breakdown site. With increasing microsphere size, the number of transfected cells decreases. The control dishes which were exposed to just tweezing laser and the pulsed ns laser without microsphere breakdown showed negligible number of transfected cells compared to dishes with microsphere breakdown.

The number of transfected cells as a function of axial position from the bottom of the cell dish was also investigated using 0.5 μm polymer microsphere size shown in Fig. 7.9 (B). It was found that the optimal axial position is at 10 μm from the dish bottom. Further above 10 μm, the number of transfected cells decreases which maybe due to the radially decreasing impact of the fluid shear stress from the point of breakdown. Also with increasing distance, D, from the substrate, the γ factor increases decreasing the energy of the cavitation bubble due to formation of jetting and counterjets. At 25 μm, cells were observed to be unaffected by the breakdown despite the formation of residual bubbles. This shows that LIB from a range of

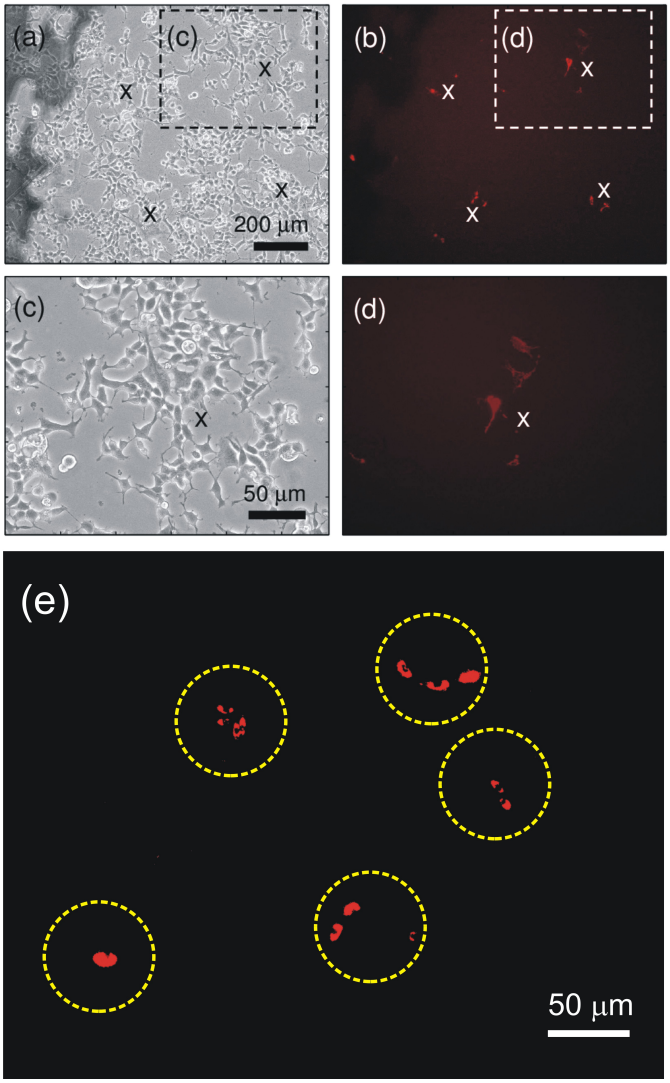

Figure 7.8: Transfection of Mito-DsRed encoding plasmids into multiples of HEK 293 cells at four LIB sites indicated as '*x*'. (a) Bright field image of cells 48 h after LIB. (b) Fluorescence images of image (a) showing transfected cells at the four LIB sites. (c) A section of image (a) showing cells around one of the LIB sites. (d) A section of (b) and a corresponding fluorescence image of (c) showing four or more cells transfected around the LIB site. (e) Fluorescence image of transfected CHO-K1 cells. The encircled regions referred to affected area surrounding a breakdown site.

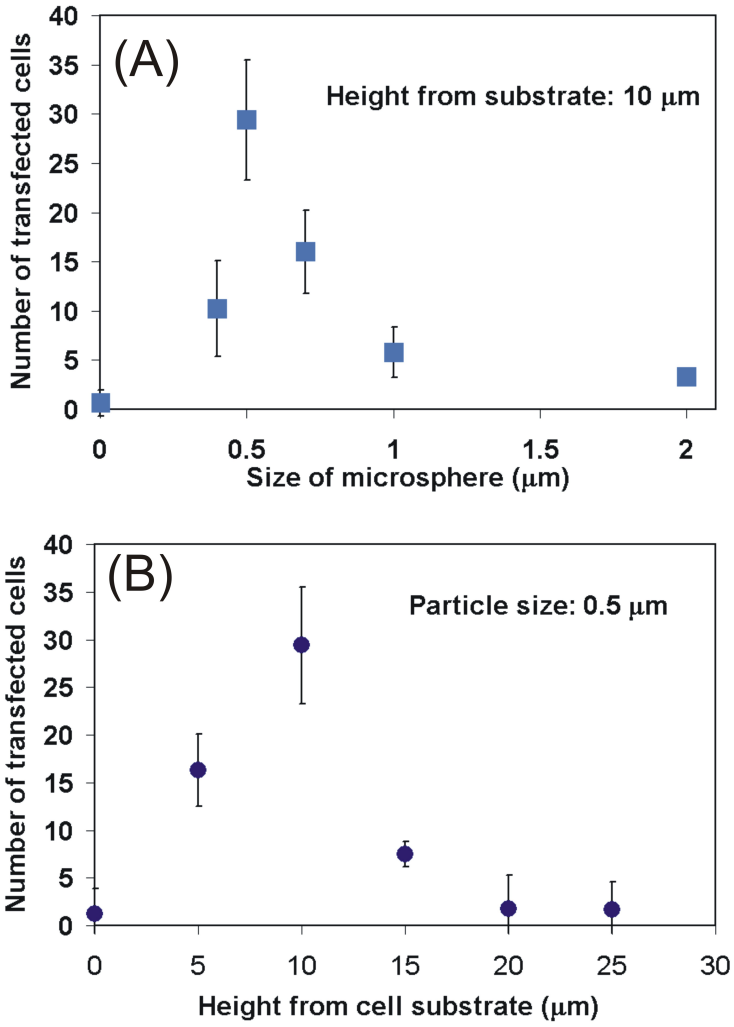

Figure 7.9: Optimisation of transfection of Mito-DsRed encoding plasmids into multiples of CHO-K1 cells by LIB parameters for P= 1 mW and T= 40 ms. (A) Number of cells transfected with different microsphere sizes at the fixed axial location of 10 μm. (B) Number of cells transfected at different axial locations with the fixed particle size of 0.5 μm. The error bars indicate ± standard deviation.

heights above the cell monolayer also provided a means of optimising molecular delivery since the shear stress to cells from the microsphere LIB is dependent on the stand-off parameter given by Eq. 7.1. It was important to note that with increasing distance from the bottom, spherical aberration may come into play, influencing both the tweezing and pulsed ns laser beam.

7.6 Discussion and Conclusion

In this chapter, LIB of an optically trapped microsphere was demonstrated inducing cell permeabilisation and transfection of CHO-K1 and HEK293 cells. The size of the microsphere affected the the clearance zone radius as well as the number of cells lysed during the process. The region of affected area was characterised for microsphere sizes 0.5, 1.0 and 2.0 μm. Both 1.0 and 2.0 μm microsphere sizes resulted in a larger clearance and affected zone compared to 0.5 μm. This was attributed to a larger cavitation bubble generated owing to a larger volume of ablated material and resulting plasma. This is in agreement with previous investigations that have shown that the size of cavitation bubble scales with the zone of cell lysis [32, 30].

The magnitude of shear stress produced during the breakdown is also proportional to the cavitation bubble size and decays as a function of distance from the breakdown site [30]. In this study, a small region of clearance (r= 10–15 μm) and limited number of necrotic cells corresponding to 3–6 cells at a distance of r= 35 μm from the breakdown site can be obtained which corresponds to the region of largest shear stress during the bubble wall expansion with no cellular detachment. In comparison, the smallest affected area reported for LIB in water with cell monolayer has an affected radius, $r\geq$ 60 μm with both cellular detachment and necrosis [30]. This corresponds to 60 necrotic or lysed cells since their cell monolayer confluency was 1000 cells/mm. Hence, the LIB of optical trapped microsphere provided a more localised approach to targeting cells compared to LIB in water, limiting the number of necrotic cells.

In this work, the required threshold was minimised by simply changing the optically trapped particle material. The laser pulse energy used in this experiment was only 1 μJ to ablate the polymer microsphere corresponding to only 12.5% of the threshold pulse energy of water reported by Rau and co-workers [32]. Similarly, other types of particles can be utilised for this experiment to control the mechanical stress induced on the sample. An example is silica which has a slightly higher breakdown threshold of 0.9 GW/mm^2 [208]. With more advanced nanotechnology, many particles of a variety of properties are being synthesised which can further optimise the level of control on the cavitation during LIB. Gold nanoparticles are

becoming a popular tool for precise nanosurgery due to its plasmonic properties when irradiated close to its resonance which could increase the surrounding media temperature leading to the formation of cavitation bubbles [213]. Recently, delivery of molecules into cells by irradiating carbon nanoparticles with fs laser pulses has also been demonstrated [214].

Using this technique, successful transfection of both HEK293 and CHO-K1 cells with a plasmid encoding for the protein, Mito-DsRed was facilitated. By changing the microsphere size and the position of the breakdown by moving the optically trapped particle along the z, an optimal transfection can be achieved using polymer microsphere size of 0.5 μm and an axial position of 10 μm from the substrate. Increasing the microsphere size from 0.5 μm to 1.0 μm resulted in a decrease in the number of transfected cells. Furthermore, increasing axial position beyond 10 μm may have decreased the impact of the shear stress due to the expanding cavitation bubble which resulted in less number of treated cells.

In summary, a technique that uses LIB of a single optically trapped microsphere was described to facilitate the optimisation of the energy required for controllable cavitation. This was achieved by varying the microsphere size and its height above the cell monolayer at which LIB was performed and led to the successful permeabilisation or transfection of cells in a targeted area with the retention of cell viability.

Part of this work was published in Applied Physics Letters, **98**, 2011 [215].

8

Summary and Future work

Cell transfection is an important and ubiquitous biological methodology that brings about an understanding of protein functionalities and corresponding cellular response by injecting genetic materials such as naked plasmid DNA, single-stranded mRNA and siRNA into living cells. The targeted delivery of macromolecules into single cells, subcellular regions within a cell and individual blastomeres would permit further advancement in molecular biology. Optical injection and transfection is a new technology utilising a laser in order to inject biological substances into the cell's cytoplasm thereby allowing the subsequent expression of the protein of interest. With increasing innovations in the design of laser systems, a variety of laser sources have been utilised for the purposes of cellular transfection. This thesis demonstrates optical injection and transfection using a variety of laser sources in either continuous or pulsed mode. Furthermore, it provides significant improvement in this field, offering new methodologies for increase in viable transfection of mammalian cells using a reactive oxygen scavenger in continuous wave violet diode systems; better targeting in fs laser systems and confined mechanical effects of optical breakdown in ns laser systems using optically tweezed microspheres.

Using a violet diode CW laser system, I demonstrated that an inexpensive, portable and compact laser system can be employed for single cell optical transfection. This is the first time that a 405 nm laser diode source was utilised for transient cell transfection of mammalian cells. The mechanism of transfection was elucidated by calculating the temperature change due to the irradiation of the laser. It was found

that the temperature change using the current parameters was not enough to induce permeability change on the cellular membrane. Hence, I proposed a photochemical effect as a dominant mechanism in transfection using this laser source. Transient transfection using a violet diode laser can be enhanced with the use of phenol red as a reactive oxygen scavenger. Demonstrating transient transfection using this laser source is a significant step towards commercialisation and wider usage of this technology.

The use of NIR fs laser sources have been previously employed for optical transfection. However, using such laser sources for this technique requires stringent focusing and is a rate-limiting step for high-throughput transfection. Hence, a system was developed that is capable of fast and accurate axial and lateral beam positioning by incorporating a spatial light modulator in the system. By designing a targeting method wherein a cell was irradiated three times, once in each axial position, it was shown that accurate targeting of the membrane is crucial for successful and viable optical injection of dyes into the cytoplasm of mammalian cells. In optical transfection, increasing the number of doses on the membrane increases the efficiency of the technique. Sixteen shots on the membrane with relatively lower power to current methodologies provided the best transfection efficiency of Mito-DsRed plasmid into mammalian cells. To design a wider-field targeting device, a piezo-driven scanning mirror was incorporated in the system increasing the targeting field of view to 140 μm by 140 μm using a $\times$60 objective.

Using a NIR fs laser coupled with a spatial light modulator, targeting and optoinjection exogenous materials into a living and developing embryo of *Pomatoceros lamarckii* was demonstrated. The NIR fs laser is capable of injecting fluorescently labeled dextran molecules into individual blastomeres of early stage embryos of this animal. Smaller embryonic cells deep within an embryo in its late stage of development can be optoinjected without affecting the surrounding tissue. It was found that embryos optoinjected at an early stage (1-cell and 2-cell) carried on dividing and passed on the dye to its daughter cells. This capability of the system would open up applications for overexpression of proteins by injecting DNA and mRNA or knockdown of protein expression into this species. Furthermore, by switching to the CW mode of laser, the same system was able to optically trap and orient an embryo. This could be an alternative to intrusive glass capillaries for holding and orienting embryos. Hence, in this chapter, an all optical approach for embryo manipulation was demonstrated by optical trapping of single-cell zygotes and optoinjection of macromolecules into the individual cells of an embryo.

Finally, a novel methodology using a pulsed ns laser source was developed in order to achieve the optical breakdown of a polymer microsphere producing cavitation

bubbles that induced membrane permeability to surrounding cells. Although, pulsed ns lasers have been ubiquitous sources for biomedical applications, the required high energy to achieve the breakdown threshold of water or coverslip induces damage to surrounding cells and tissues causing cellular lysis to a large affected area. Hence, I demonstrated that instead of breaking down water or glass coverslips in the presence of adherent cells, alternatively an optically trapped microsphere can be utilised to considerably lower the applied laser energy into the sample, thus decreasing the overall level of cellular lysis. Using this technique, a localised region of permeabilised cells was identified with their membrane integrity intact. By varying the position of the breakdown and the size of the microsphere, the transfection efficiency was optimised. This enhances the application of ns laser systems for optical transfection whilst limiting cellular lysis.

Future work on using a CW violet diode laser for cell transfection will be to determine if the addition of other ROS scavengers such as Vitamin C and antioxidants, would enhance the efficiency of the technique. Further understanding of the biochemical processes occuring during laser irradiation with the focused violet diode laser could also provide better methodologies in order to make the system a more robust and reliable device for cell transfection. For example, there is a need to investigate the optimum buffer medium to be used for CW violet diode laser transfection due to the interplay of photochemistry in the medium which affects the efficiency of transfection. CW violet diode lasers could rival against the more mature NIR fs lasers for cell transfection due to their portability allowing more biologists to access the technique. The work presented in this thesis using this laser provides an advancement towards compact and inexpensive optical transfection device.

With the enhanced targeting using the fs holographic system, the next step is to incorporate multiphoton imaging into the device allowing nonlinear imaging (*i.e.* second harmonic and third harmonic generation), which would be useful for imaging thick samples. Although, utilising a fs laser system has been a robust technique for transfection, its application to *in vivo* samples has been limited. Among the various laser sources for transfection, only fs laser can achieve deep penetration as well as precise targeting which is suitable for targeting animal models and accessing turbid areas such as the vasculature. Recently, an NIR fs laser was employed to create vasculature disruptions within a rat brain to study stroke in animal models [216]. Similarly, optical transfection of significant biomolecules in a living animal model could be the next step inorder to assess how genetic modification could enable therapeutic treatment of certain brain diseases such as Alzheimer's and Dementia.

Having demonstrated successful optoinjection of macromolecules into *P. lamarckii* embryos, future work involves finding the appropriate DNA constructs that

can be successfully be transfected in these embryos. This work also opens up the possibility to determine if the technique is suitable for other species with more sophisticated molecular biology, but still requires an efficient delivery technique to inject biomolecules into its embryo. Collaborations have been started with other developmental biologists in order to use the technique to other species.

Future work on the LIB of optically trapped microsphere technique is to perform time-resolved imaging to fully understand the events during the breakdown. Furthermore, with this technique, controllable cavitation can be achieved which may be useful for pulsed ns laser applications specifically for *in vitro* samples. Pulsed ns laser systems have been recently used to perform nanoaxotonomy in microfluidic devices for neuronal regeneration studies [217]. Currently, as pulsed ns laser systems are less expensive than fs lasers, optimising and controlling the parameters using this laser source for precise nanosurgery is still desirable.

The variety of optical transfection and injection methodologies demonstrated in this thesis extends the possible applications of the technology depending on the available laser source in a laboratory. Each laser source despite of its own advantages and disadvantages could still be optimised in order to increase the efficiency of the technique. This thesis provides a fundamental step towards commercialisation and increased throughput of optical transfection and injection for wider biological applications.

Bibliography

[1] M.W. Berns. A history of laser scissors (microbeams). *Methods in cell biology*, 82:1–3, 2007.

[2] RL Amy and R. Storb. Selective mitochondrial damage by a ruby laser microbeam: an electron microscopic study. *Science (New York, NY)*, 150(697):756, 1965.

[3] M.W. Berns. Directed chromosome loss by laser microirradiation. *Science*, 186(4165):700, 1974.

[4] M. Stiess, N. Maghelli, L.C. Kapitein, S. Gomis-Rüth, M. Wilsch-Bräuninger, C.C. Hoogenraad, I.M. Tolić-Nørrelykke, and F. Bradke. Axon extension occurs independently of centrosomal microtubule nucleation. *Science*, 327(5966):704, 2010.

[5] N.M. Wakida, E.L. Botvinick, J. Lin, M.W. Berns, and M.G. Castro. An intact centrosome is required for the maintenance of polarization during directional cell migration. *PloS one*, 5(12):e15462, 2010.

[6] L. Paterson, E. Papagiakoumou, G. Milne, V. Garcés-Chávez, SA Tatarkova, W. Sibbett, FJ Gunn-Moore, PE Bryant, AC Riches, and K. Dholakia. Light-induced cell separation in a tailored optical landscape. *Applied Physics Letters*, 87:123901, 2005.

[7] M. Zhou, EL Zhao, HF Yang, AH Gong, JK Di, and ZJ Zhang. Generation of calcium waves in living cells induced by 1 kHz femtosecond laser protuberance microsurgery. *Laser physics*, 19(7):1470–1474, 2009.

[8] H. Li, C.E. Sims, H.Y. Wu, and N.L. Allbritton. Spatial control of cellular measurements with the laser micropipet. *Analytical chemistry*, 73(19):4625–4631, 2001.

[9] J. Lippincott-Schwartz and G.H. Patterson. Photoactivatable fluorescent proteins for diffraction-limited and super-resolution imaging. *Trends in cell biology*, 19(11):555–565, 2009.

[10] M. Vesaluoma, J. Pérez-Santonja, W.M. Petroll, T. Linna, J. Alió, and T. Tervo. Corneal stromal changes induced by myopic LASIK. *Investigative ophthalmology & visual science*, 41(2):369, 2000.

[11] D.E. Dolmans and R.K.J. Dai Fukumura. Photodynamic therapy for cancer. *Nature Reviews Cancer*, 3(5):380–387, 2003.

[12] M. Sofer, J.D. Watterson, T.A. Wollin, L. Nott, H. Razvi, and J.D. Denstedt. Holmium:YAG laser lithotripsy for upper urinary tract calculi in 598 patients. *The Journal of urology*, 167(1):31–34, 2002.

[13] T.D. Myers and W.D. Myers. The use of a laser for debridement of incipient caries. *The Journal of Prosthetic Dentistry*, 53(6):776–779, 1985.

[14] M. Antkowiak, M.L. Torres-Mapa, F. Gunn-Moore, and K. Dholakia. Application of dynamic diffractive optics for enhanced femtosecond laser based cell transfection. *Journal of Biophotonics*, 3:696–705, October 2010.

[15] Robert F. Marchington, Yoshihiko Arita, Xanthi Tsampoula, Frank J. Gunn-Moore, and Kishan Dholakia. Optical injection of mammalian cells using a microfluidic platform. *Biomed. Opt. Express*, 1(2):527–536, 2010.

[16] D.J. Stevenson, F.J. Gunn-Moore, P. Campbell, and K. Dholakia. Single cell optical transfection. *Journal of the Royal Society Interface*, 2010.

[17] L.E. Barrett, J.Y. Sul, H. Takano, E.J. Van Bockstaele, P.G. Haydon, and J.H. Eberwine. Region-directed phototransfection reveals the functional significance of a dendritically synthesized transcription factor. *Nature Methods*, 3(6):455, 2006.

[18] P. Mthunzi, K. Dholakia, and F. Gunn-Moore. Phototransfection of mammalian cells using femtosecond laser pulses: optimization and applicability to stem cell differentiation. *Journal of Biomedical Optics*, 15:041507, 2010.

[19] M. Tsukakoshi, S. Kurata, Y. Nomiya, Y. Ikawa, and T. Kasuya. A novel method of DNA transfection by laser microbeam cell surgery. *Applied Physics B: Lasers and Optics*, 35(3):135–140, 1984.

[20] W. Tao, J. Wilkinson, EJ Stanbridge, and MW Berns. Direct gene transfer into human cultured cells facilitated by laser micropuncture of the cell membrane. *Proceedings of the National Academy of Sciences*, 84(12):4180, 1987.

[21] C.T.A. Brown, D.J. Stevenson, X. Tsampoula, C. McDougall, A.A. Lagatsky, W. Sibbett, F.J. Gunn-Moore, and K. Dholakia. Enhanced operation of femtosecond lasers and applications in cell transfection. *J Biophotonics*, 1(3):183–199, 2008.

[22] Herbert Schneckenburger, Anita Hendinger, Reinhard Sailer, Wolfgang S. L. Strauss, and Michael Schmitt. Laser-assisted optoporation of single cells. *Journal of Biomedical Optics*, 7(3):410–416, 2002.

[23] G. Palumbo, M. Caruso, E. Crescenzi, M.F. Tecce, G. Roberti, and A. Colasanti. Targeted gene transfer in eucaryotic cells by dye-assisted laser optoporation. *Journal of Photochemistry & Photobiology, B: Biology*, 36(1):41–46, 1996.

[24] A.V. Nikolskaya, V.P. Nikolski, and I.R. Efimov. Gene printer: Laser-scanning targeted transfection of cultured cardiac neonatal rat cells. *Cell Communication and Adhesion*, 13(4):217–222, 2006.

[25] U.K. Tirlapur and K. Konig. Targeted transfection by femtosecond laser. *Nature*, 418:290–291, 2002.

[26] D. Stevenson, B. Agate, X. Tsampoula, P. Fischer, C. T. A. Brown, W. Sibbett, A. Riches, F. Gunn-Moore, and K. Dholakia. Femtosecond optical transfection of cells:viability and efficiency. *Opt. Express*, 14(16):7125–7133, 2006.

[27] J. Baumgart, W. Bintig, A. Ngezahayo, S. Willenbrock, H. Murua Escobar, W. Ertmer, H. Lubatschowski, and A. Heisterkamp. Quantified femtosecond laser based opto-perforation of living GFSHR-17 and MTH53 cells. *Opt. Express*, 16(5):3021–3031, 2008.

[28] J.S. Soughayer, T. Krasieva, S.C. Jacobson, J.M. Ramsey, B.J. Tromberg, and N.L. Allbritton. Characterization of cellular optoporation with distance. *Anal. Chem*, 72(6):1342–1347, 2000.

[29] I.B. Clark, E.G. Hanania, J. Stevens, M. Gallina, A. Fieck, R. Brandes, B.O. Palsson, and M.R. Koller. Optoinjection for efficient targeted delivery of a broad range of compounds and macromolecules into diverse cell types. *Journal of Biomedical Optics*, 11:014034, 2006.

[30] A.N. Hellman, K.R. Rau, H.H. Yoon, and V. Venugopalan. Biophysical response to pulsed laser microbeam-induced cell lysis and molecular delivery. *Journal of Biophotonics*, 1(1):24–35, 2008.

[31] L. Paterson, B. Agate, M. Comrie, R. Ferguson, T. Lake, J. Morris, A. Carruthers, C. T. Brown, W. Sibbett, P. Bryant, F. Gunn-Moore, A. Riches, and Kishan Dholakia. Photoporation and cell transfection using a violet diode laser. *Opt. Express*, 13(2):595–600, 2005.

[32] K.R. Rau, P.A. Quinto-Su, A.N. Hellman, and V. Venugopalan. Pulsed laser microbeam-induced cell lysis: time-resolved imaging and analysis of hydrodynamic effects. *Biophysical journal*, 91(1):317–329, 2006.

[33] N.A. Campbell and J.B. Reece. Biology 7th ed, international edition. 2005.

[34] P.L. Felgner, T.R. Gadek, M. Holm, R. Roman, H.W. Chan, M. Wenz, J.P. Northrop, G.M. Ringold, and M. Danielsen. Lipofection: a highly efficient, lipid-mediated DNA-transfection procedure. *Proceedings of the National Academy of Sciences of the United States of America*, 84(21):7413, 1987.

[35] C. Lappe-Siefke, C. Maas, and M. Kneussel. Microinjection into cultured hippocampal neurons: A straightforward approach for controlled cellular delivery of nucleic acids, peptides and antibodies. *Journal of neuroscience methods*, 175(1):88–95, 2008.

[36] M.R. Capecchi. High efficiency transformation by direct microinjection of DNA into cultured mammalian cells. *Cell*, 22(2 Pt 2):479–488, 1980.

[37] S. Mehier-Humbert, T. Bettinger, F. Yan, and R.H. Guy. Plasma membrane poration induced by ultrasound exposure: implication for drug delivery. *Journal of controlled release*, 104(1):213–222, 2005.

[38] J.W. Gordon, G.A. Scangos, D.J. Plotkin, J.A. Barbosa, and F.H. Ruddle. Genetic transformation of mouse embryos by microinjection of purified DNA. *Proceedings of the National Academy of Sciences of the United States of America*, 77(12):7380, 1980.

[39] JW Gordon and FH Ruddle. Gene transfer into mouse embryos: production of transgenic mice by pronuclear injection. *Methods in enzymology*, 101:411, 1983.

[40] E. Cornell, WW Fisher, R. Nordmeyer, D. Yegian, M. Dong, MD Biggin, SE Celniker, and J. Jin. Automating fruit fly Drosophila embryo injection

for high throughput transgenic studies. *Review of Scientific Instruments*, 79:013705, 2008.

[41] W. Wang, Y. Sun, M. Zhang, R. Anderson, L. Langille, and W. Chan. A system for high-speed microinjection of adherent cells. *Review of Scientific Instruments*, 79:104302, 2008.

[42] S. Zappe, M. Fish, M.P. Scott, and O. Solgaard. Automated MEMS-based Drosophila embryo injection system for high-throughput RNAi screens. *Lab on a Chip*, 6(8):1012–1019, 2006.

[43] T.M. Klein, ED Wolf, R. Wu, and JC Sanford. High-velocity microprojectiles for delivering nucleic acids into living cells. *Nature*, 327(6117):70–73, 1987.

[44] W.N. Lian, C.H. Chang, Y.J. Chen, R.L. Dao, Y.C. Luo, J.Y. Chien, S.L. Hsieh, and C.H. Lin. Intracellular delivery can be achieved by bombarding cells or tissues with accelerated molecules or bacteria without the need for carrier particles. *Experimental cell research*, 313(1):53–64, 2007.

[45] D. Rinberg, C. Simonnet, and A. Groisman. Pneumatic capillary gun for ballistic delivery of microparticles. *Applied Physics Letters*, 87:014103, 2005.

[46] O. Shefi, C. Simonnet, M.W. Baker, J.R. Glass, E.R. Macagno, and A. Groisman. Microtargeted gene silencing and ectopic expression in live embryos using biolistic delivery with a pneumatic capillary gun. *Journal of Neuroscience*, 26(23):6119, 2006.

[47] E. Neumann, M. Schaefer-Ridder, Y. Wang, and PH Hofschneider. Gene transfer into mouse lyoma cells by electroporation in high electric fields. *The EMBO journal*, 1(7):841, 1982.

[48] M.E. Fromm, L.P. Taylor, and V. Walbot. Stable transformation of maize after gene transfer by electroporation. *Nature*, 319(6056):791–793, 1986.

[49] M. Fromm, L.P. Taylor, and V. Walbot. Expression of genes transferred into monocot and dicot plant cells by electroporation. *Proceedings of the National Academy of Sciences of the United States of America*, 82(17):5824, 1985.

[50] P.G. Leclere, A. Panjwani, R. Docherty, M. Berry, J. Pizzey, and D.A. Tonge. Effective gene delivery to adult neurons by a modified form of electroporation. *Journal of neuroscience methods*, 142(1):137–143, 2005.

[51] D.A. Powers, L. Hereford, T. Cole, TT Chen, CM Lin, K. Kight, K. Creech, and R. Dunham. Electroporation: a method for transferring genes into the gametes of zebrafish (brachydanio rerio), channel catfish (ictalurus punctatus), and common carp (cyprinus carpio). *Molecular marine biology and biotechnology*, 1(4-5):301, 1992.

[52] F. Calegari, A.M. Marzesco, R. Kittler, F. Buchholz, and W.B. Huttner. Tissue-specific RNA interference in post-implantation mouse embryos using directional electroporation and whole embryo culture. *Differentiation*, 72(2-3):92–102, 2004.

[53] N. Itasaki, S. Bel-Vialar, and R. Krumlauf. Shocking'developments in chick embryology: electroporation and in ovo gene expression. *Nature Cell Biology*, 1:203–208, 1999.

[54] H. Aihara and J. Miyazaki. Gene transfer into muscle by electroporation in vivo. *Nature biotechnology*, 16(9):867–870, 1998.

[55] K. Haas, WC Sin, A. Javaherian, Z. Li, and HT Cline. Single-cell electroporation for in vivo neuronal gene expression. *Neuron*, 29(3):583–591, 2001.

[56] T.E. Tjelle, R. Salte, I. Mathiesen, and R. Kjeken. A novel electroporation device for gene delivery in large animals and humans. *Vaccine*, 24(21):4667–4670, 2006.

[57] J. Wang, Y. Zhan, V.M. Ugaz, and C. Lu. Vortex-assisted DNA delivery. *Lab on a Chip*, 10(16):2057–2061, 2010.

[58] T. Xie. Study of mechanisms of electric field-induced DNA transfection. v. effects of DNA topology on surface binding, cell uptake, expression, and integration into host chromosomes of DNA in the mammalian cell. *Biophysical Journal*, 65:1684–1689, 1993.

[59] DC Chang and T.S. Reese. Changes in membrane structure induced by electroporation as revealed by rapid-freezing electron microscopy. *Biophysical journal*, 58(1):1–12, 1990.

[60] M. Golzio, J. Teissié, and M.P. Rols. Direct visualization at the single-cell level of electrically mediated gene delivery. *Proceedings of the National Academy of Sciences of the United States of America*, 99(3):1292, 2002.

[61] T.D. Xie and T.Y. Tsong. Study of mechanisms of electric field-induced DNA transfection. ii. transfection by low-amplitude, low-frequency alternating electric fields. *Biophysical journal*, 58(4):897–903, 1990.

[62] VA Klenchin, SI Sukharev, SM Serov, and LV Chernomordik. Electrically induced DNA uptake by cells is a fast process involving DNA electrophoresis. *Biophysical journal*, 60(4):804–811, 1991.

[63] SI Sukharev, VA Klenchin, SM Serov, and LV Chernomordik. Electroporation and electrophoretic DNA transfer into cells. the effect of DNA interaction with electropores. *Biophysical journal*, 63(5):1320–1327, 1992.

[64] M. Fechheimer, J.F. Boylan, S. Parker, J.E. Sisken, G.L. Patel, and S.G. Zimmer. Transfection of mammalian cells with plasmid DNA by scrape loading and sonication loading. *Proceedings of the National Academy of Sciences of the United States of America*, 84(23):8463, 1987.

[65] DM Skyba, RJ Price, AZ Linka, TC Skalak, and S. Kaul. Direct in vivo visualization of intravascular destruction of microbubbles by ultrasound and its local effects on tissue. *Circulation*, 98(4):290, 1998.

[66] R. Bekeredjian, P.A. Grayburn, and R.V. Shohet. Use of ultrasound contrast agents for gene or drug delivery in cardiovascular medicine. *Journal of the American College of Cardiology*, 45(3):329–335, 2005.

[67] EA Brujan. The role of cavitation microjets in the therapeutic applications of ultrasound. *Ultrasound in medicine & biology*, 30(3):381–387, 2004.

[68] P. Prentice, A. Cuschieri, K. Dholakia, M. Prausnitz, and P. Campbell. Membrane disruption by optically controlled microbubble cavitation. *Nature Physics*, 1(2):107–110, 2005.

[69] S. Bao, B.D. Thrall, and D.L. Miller. Transfection of a reporter plasmid into cultured cells by sonoporation in vitro. *Ultrasound in medicine & biology*, 23(6):953–959, 1997.

[70] J. Wu. Theoretical study on shear stress generated by microstreaming surrounding contrast agents attached to living cells. *Ultrasound in Medicine & Biology*, 28(1):125–129, 2002.

[71] S. Zhu and P. Zhong. Shock wave–inertial microbubble interaction: A theoretical study based on the Gilmore formulation for bubble dynamics. *The Journal of the Acoustical Society of America*, 106:3024, 1999.

[72] M. Shimamura, N. Sato, Y. Taniyama, S. Yamamoto, M. Endoh, H. Kurinami, M. Aoki, T. Ogihara, Y. Kaneda, and R. Morishita. Development of efficient plasmid DNA transfer into adult rat central nervous system using microbubble-enhanced ultrasound. *Gene therapy*, 11(20):1532–1539, 2004.

[73] Y. Taniyama, K. Tachibana, K. Hiraoka, T. Namba, K. Yamasaki, N. Hashiya, M. Aoki, T. Ogihara, K. Yasufumi, and R. Morishita. Local delivery of plasmid DNA into rat carotid artery using ultrasound. *Circulation*, 105(10):1233, 2002.

[74] P.L. McNeil, S.S. Vogel, K. Miyake, and M. Terasaki. Patching plasma membrane disruptions with cytoplasmic membrane. *Journal of Cell Science*, 113:1891–1902, 2000.

[75] M. Terasaki, K. Miyake, and P.L. McNeil. Large plasma membrane disruptions are rapidly resealed by Ca^{2+}-dependent vesicle–vesicle fusion events. *The Journal of cell biology*, 139(1):63, 1997.

[76] LV Heilbrunn. The surface precipitation reaction of living cells. *Proceedings of the American Philosophical Society*, 69(1):295–301, 1930.

[77] R.A. Steinhardt, G. Bi, and J.M. Alderton. Cell membrane resealing by a vesicular mechanism similar to neurotransmitter release. *Science*, 263(5145):390, 1994.

[78] G.Q. Bi, J.M. Alderton, and R.A. Steinhardt. Calcium-regulated exocytosis is required for cell membrane resealing. *The Journal of cell biology*, 131(6):1747, 1995.

[79] K. Miyake and P.L. McNeil. Vesicle accumulation and exocytosis at sites of plasma membrane disruption. *The Journal of cell biology*, 131(6):1737, 1995.

[80] T. Togo, J.M. Alderton, G.Q. Bi, and R.A. Steinhardt. The mechanism of facilitated cell membrane resealing. *Journal of cell science*, 112:719–731, 1999.

[81] T. Togo, T.B. Krasieva, and R.A. Steinhardt. A decrease in membrane tension precedes successful cell-membrane repair. *Molecular biology of the cell*, 11(12):4339, 2000.

[82] Y. Zhou, J. Shi, J. Cui, and C.X. Deng. Effects of extracellular calcium on cell membrane resealing in sonoporation. *Journal of controlled release: official journal of the Controlled Release Society*, 126(1):34, 2008.

[83] O. Seksek, J. Biwersi, and AS Verkman. Translational diffusion of macromolecule-sized solutes in cytoplasm and nucleus. *The Journal of cell biology*, 138(1):131, 1997.

[84] G.L. Lukacs, P. Haggie, O. Seksek, D. Lechardeur, N. Freedman, and AS Verkman. Size-dependent DNA mobility in cytoplasm and nucleus. *Journal of Biological Chemistry*, 275(3):1625, 2000.

[85] D. Lechardeur, AS Verkman, and G.L. Lukacs. Intracellular routing of plasmid DNA during non-viral gene transfer. *Advanced drug delivery reviews*, 57(5):755–767, 2005.

[86] D. Lechardeur, KJ Sohn, M. Haardt, PB Joshi, M. Monck, RW Graham, B. Beatty, J. Squire, H. O'brodovich, and GL Lukacs. Metabolic instability of plasmid DNA in the cytosol: a potential barrier to gene transfer. *Gene therapy*, 6(4):482, 1999.

[87] M.A. Zanta, P. Belguise-Valladier, and J.P. Behr. Gene delivery: a single nuclear localization signal peptide is sufficient to carry DNA to the cell nucleus. *Proceedings of the National Academy of Sciences of the United States of America*, 96(1):91, 1999.

[88] S. Brunner, T. Sauer, S. Carotta, M. Cotten, M. Saltik, and E. Wagner. Cell cycle dependence of gene transfer by lipoplex, polyplex and recombinant adenovirus. *Gene therapy*, 7(5):401, 2000.

[89] I. Mortimer, P. Tam, I. MacLachlan, RW Graham, EG Saravolac, and PB Joshi. Cationic lipid-mediated transfection of cells in culture requires mitotic activity. *Gene therapy*, 6(3):403, 1999.

[90] P.N. Prasad. *Introduction to biophotonics*. John Wiley & Sons, 2003.

[91] M.H. Niemz. Laser-tissue interactions: fundamentals and applications. 2007.

[92] T.J. Dougherty, C.J. Gomer, G. Jori, D. Kessel, M. Korbelik, J. Moan, and Q. Peng. Photodynamic therapy. *Journal of the National Cancer Institute*, 90(12):889, 1998.

[93] J.C. Liao, J. Roider, and D.G. Jay. Chromophore-assisted laser inactivation of proteins is mediated by the photogeneration of free radicals. *Proceedings of the National Academy of Sciences*, 91(7):2659, 1994.

[94] K. Jacobson, Z. Rajfur, E. Vitriol, and K. Hahn. Chromophore-assisted laser inactivation in cell biology. *Trends in cell biology*, 18(9):443–450, 2008.

[95] M. Castrén-Persons, T. Schröder, OJ Rämö, P. Puolakkainen, and E. Lehtonen. Contact Nd:YAG laser potentiates the tumor cell killing effect of hyperthermia. *Lasers in surgery and medicine*, 11(6):595–600, 1991.

[96] J.R. Dynlacht and M.H. Fox. Heat-induced changes in the membrane fluidity of chinese hamster ovary cells measured by flow cytometry. *Radiation research*, pages 48–54, 1992.

[97] A. Vogel, J. Noack, G. Huttman, and G. Paltauf. Mechanisms of femtosecond laser nanosurgery of cells and tissues. *Applied Physics B: Lasers and Optics*, 81(8):1015–1047, 2005.

[98] U.K. Tirlapur, K. Konig, C. Peuckert, R. Krieg, and K.J. Halbhuber. Femtosecond near-infrared laser pulses elicit generation of reactive oxygen species in mammalian cells leading to apoptosis-like death. *Experimental Cell Research*, 263(1):88–97, 2001.

[99] F. Docchio, CA Sacchi, and J. Marshall. Experimental investigation of optical breakdown thresholds in ocular media under single pulse irradiation with different pulse durations. *Lasers Ophthalmol*, 1:83–93, 1986.

[100] CA Sacchi. Laser-induced electric breakdown in water. *JOSA B*, 8(2):337–345, 1991.

[101] P.K. Kennedy, D.X. Hammer, and B.A. Rockwell. Laser-induced breakdown in aqueous media. *Progress in quantum electronics*, 21(3):155–248, 1997.

[102] LV Keldysh. Ionization in the field of a strong electromagnetic wave. *Soviet Physics JETP*, 20(5):1307–1314, 1965.

[103] S. Eaton, H. Zhang, P. Herman, F. Yoshino, L. Shah, J. Bovatsek, and A. Arai. Heat accumulation effects in femtosecond laser-written waveguides with variable repetition rate. *Optics Express*, 13(12):4708–4716, 2005.

[104] H.S. Carslaw and J.C. Jaeger. Conduction of heat in solids. *Oxford: Clarendon Press, 1959, 2nd ed.*, 1, 1959.

[105] K. König, TW Becker, P. Fischer, I. Riemann, and KJ Halbhuber. Pulse-length dependence of cellular response to intense near-infrared laser pulses in multiphoton microscopes. *Optics letters*, 24(2):113–115, 1999.

[106] D. Träutlein, M. Deibler, A. Leitenstorfer, and E. Ferrando-May. Specific local induction of DNA strand breaks by infrared multi-photon absorption. *Nucleic acids research*, 38(3):e14, 2010.

[107] A. Vogel, N. Linz, S. Freidank, and G. Paltauf. Femtosecond-laser-induced nanocavitation in water: implications for optical breakdown threshold and cell surgery. *Physical review letters*, 100(3):38102, 2008.

[108] I. Maxwell, S. Chung, and E. Mazur. Nanoprocessing of subcellular targets using femtosecond laser pulses. *Medical Laser Application*, 20(3):193–200, 2005.

[109] K. Kuetemeyer, J. Baumgart, H. Lubatschowski, and A. Heisterkamp. Repetition rate dependency of low-density plasma effects during femtosecond-laser-based surgery of biological tissue. *Applied Physics B: Lasers and Optics*, 97(3):695–699, 2009.

[110] M.F. Yanik, H. Cinar, H.N. Cinar, A. Gibby, A.D. Chisholm, Y. Jin, and A. Ben-Yakar. Nerve regeneration in caenorhabditis elegans after femtosecond laser axotomy. *Selected Topics in Quantum Electronics, IEEE Journal of*, 12(6):1283–1291, 2006.

[111] A. Vogel. Nonlinear absorption: intraocular microsurgery and laser lithotripsy. *Physics in Medicine and Biology*, 42:895, 1997.

[112] K.R. Rau, A. Guerra III, A. Vogel, and V. Venugopalan. Investigation of laser-induced cell lysis using time-resolved imaging. *Applied physics letters*, 84:2940, 2004.

[113] A. Vogel, S. Busch, K. Jungnickel, and R. Birngruber. Mechanisms of intraocular photodisruption with picosecond and nanosecond laser pulses. *Lasers in surgery and medicine*, 15(1):32–43, 1994.

[114] M. Arora, L. Junge, and CD Ohl. Cavitation cluster dynamics in shock-wave lithotripsy: Part 1. free field. *Ultrasound in medicine & biology*, 31(6):827–839, 2005.

[115] A. Philipp and W. Lauterborn. Cavitation erosion by single laser-produced bubbles. *Journal of Fluid Mechanics*, 361:75–116, 1998.

[116] A. Vogel, S. Busch, and U. Parlitz. Shock wave emission and cavitation bubble generation by picosecond and nanosecond optical breakdown in water. *Journal of the Acoustical Society of America*, 100(1):148–165, 1996.

[117] C. Kielbassa, L. Roza, and B. Epe. Wavelength dependence of oxidative DNA damage induced by UV and visible light. *Carcinogenesis*, 18(4):811, 1997.

[118] S.C. Jones, P. Braunlich, R.T. Casper, X.A. Shen, and P. Kelly. Recent progress on laser-induced modifications and intrinsic bulk damage of wide-gap optical materials. *Optical Engineering*, 28:1039–1068, 1989.

[119] V. Sgambato, P. Vanhoutte, C. Pages, M. Rogard, R. Hipskind, M.J. Besson, and J. Caboche. In vivo expression and regulation of Elk-1, a target of the extracellular-regulated kinase signaling pathway, in the adult rat brain. *The Journal of neuroscience*, 18(1):214, 1998.

[120] V. Kohli, V. Robles, M.L. Cancela, J.P. Acker, A.J. Waskiewicz, and A.Y. Elezzabi. An alternative method for delivering exogenous material into developing zebrafish embryos. *Biotechnology and bioengineering*, 98(6):1230–1241, 2007.

[121] M. Terakawa, M. Ogura, S. Sato, H. Wakisaka, H. Ashida, M. Uenoyama, Y. Masaki, and M. Obara. Gene transfer into mammalian cells by use of a nanosecond pulsed laser-induced stress wave. *Optics letters*, 29(11):1227–1229, 2004.

[122] M. Terakawa, S. Sato, H. Ashida, K. Aizawa, M. Uenoyama, Y. Masaki, and M. Obara. In vitro gene transfer to mammalian cells by the use of laser-induced stress waves: effects of stress wave parameters, ambient temperature, and cell type. *Journal of Biomedical Optics*, 11:014026, 2006.

[123] K. Rhodes, I. Clark, M. Zatcoff, T. Eustaquio, K.L. Hoyte, and M.R. Koller. *Cellular laserfection*, volume 82. Elsevier, 2007.

[124] T. Lake, A. Carruthers, M. Taylor, L. Paterson, F. Gunn-Moore, J. Allen, W. Sibbett, and K. Dholakia. Optical trapping and fluorescence excitation with violet diode lasers and extended cavity surface emitting lasers. *Optics Express*, 12(4):670–678, 2004.

[125] C. Lutz, T.S. Otis, V. DeSars, S. Charpak, D.A. DiGregorio, and V. Emiliani. Holographic photolysis of caged neurotransmitters. *Nature methods*, 5(9):821–827, 2008.

[126] S.B. Brown, E.A. Brown, and I. Walker. The present and future role of photodynamic therapy in cancer treatment. *The lancet oncology*, 5(8):497–508, 2004.

[127] J.R. Lloyd and M. Mirkov. Selective photothermolysis of the sebaceous glands for acne treatment. *Lasers in surgery and medicine*, 31(2):115–120, 2002.

[128] J. Girkin, A. Ferguson, D. Wokosin, and A. Gurney. Confocal microscopy using an InGaN violet laser diode at 406nm. *Optics Express*, 7(10):336–341, 2000.

[129] F.J. Gunn-Moore, G.I. Welsh, L.R. Herron, F. Brannigan, K. Venkateswarlu, S. Gillespie, M. Brandwein-Gensler, R. Madan, J.M. Tavaré, P.J. Brophy, et al. A novel 4.1 ezrin radixin moesin (ferm)-containing protein,willin. *FEBS letters*, 579(22):5089–5094, 2005.

[130] M.L. Torres-Mapa, L. Angus, M. Ploschner, K. Dholakia, and F.J. Gunn-Moore. Transient transfection of mammalian cells using a violet diode laser. *Journal of Biomedical Optics*, 15:041506, 2010.

[131] J. Dai and M.P. Sheetz. Membrane tether formation from blebbing cells. *Biophysical journal*, 77(6):3363–3370, 1999.

[132] E.B. Podgorsak. Review of radiation oncology physics: a handbook for teachers and students. *Review of radiation oncology physics: a handbook for teachers and students*, 2003.

[133] J.B. Lewis, J.C. Wataha, R.L.W. Messer, G.B. Caughman, T. Yamamoto, and S.D. Hsu. Blue light differentially alters cellular redox properties. *Journal of Biomedical Materials Research Part B Applied Biomaterials*, 72(2):223–229, 2005.

[134] M. Eichler, R. Lavi, A. Shainberg, and R. Lubart. Flavins are source of visible-light-induced free radical formation in cells. *Lasers in Surgery and Medicine*, 37(4):314–319, 2005.

[135] P.E. Hockberger, T.A. Skimina, V.E. Centonze, C. Lavin, S. Chu, S. Dadras, J.K. Reddy, and J.G. White. Activation of flavin-containing oxidases underlies light-induced production of H_2O_2 in mammalian cells. *Proceedings of the National Academy of Sciences*, 96(11):6255, 1999.

[136] A. Fire, S. Xu, M.K. Montgomery, S.A. Kostas, S.E. Driver, C.C. Mello, et al. Potent and specific genetic interference by double-stranded RNA in Caenorhabditis elegans. *Nature-London*, pages 806–810, 1998.

[137] M.T. McManus and P.A. Sharp. Gene silencing in mammals by small interfering RNAs. *Nature Reviews Genetics*, 3(10):737–747, 2002.

[138] K. Ribbeck and D. Görlich. Kinetic analysis of translocation through nuclear pore complexes. *The EMBO Journal*, 20(6):1320, 2001.

[139] DMF Prazeres. Prediction of diffusion coefficients of plasmids. *Biotechnology and Bioengineering*, 99(4):1040, 2008.

[140] G. Baffou, R. Quidant, and C. Girard. Heat generation in plasmonic nanostructures: Influence of morphology. *Applied Physics Letters*, 94:153109, 2009.

[141] P. Morlière, A. Moysan, R. Santus, G. Huppe, J.C. Mazière, and L. Dubertret. UVA-induced lipid peroxidation in cultured human fibroblasts. *Biochimica et Biophysica Acta (BBA)-Lipids and Lipid Metabolism*, 1084(3):261–268, 1991.

[142] A. Grzelak, B. Rychlik, and G. Bartosz. Light-dependent generation of reactive oxygen species in cell culture media. *Free Radical Biology and Medicine*, 30(12):1418–1425, 2001.

[143] E. Zeira, A. Manevitch, A. Khatchatouriants, O. Pappo, E. Hyam, M. Darash-Yahana, E. Tavor, A. Honigman, A. Lewis, and E. Galun. Femtosecond infrared laseran efficient and safe in vivo gene delivery system for prolonged expression. *Molecular therapy*, 8(2):342–350, 2003.

[144] X. Tsampoula, V. Garcés-Chávez, M. Comrie, DJ Stevenson, B. Agate, CTA Brown, F. Gunn-Moore, and K. Dholakia. Femtosecond cellular transfection using a nondiffracting light beam. *Applied Physics Letters*, 91:053902, 2007.

[145] X. Tsampoula, K. Taguchi, T. Cižmár, V. Garces-Chavez, N. Ma, S. Mohanty, K. Mohanty, F. Gunn-Moore, and K. Dholakia. Fibre based cellular transfection. *Opt. Express*, 16(21):17007–17013, 2008.

[146] N. Ma, PC Ashok, DJ Stevenson, FJ Gunn-Moore, and K. Dholakia. Integrated optical transfection system using a microlens fiber combined with microfluidic gene delivery. *Biomedical Optics Express*, 1(2):694–705, 2010.

[147] G.D. Reddy, K. Kelleher, R. Fink, and P. Saggau. Three-dimensional random access multiphoton microscopy for functional imaging of neuronal activity. *Nature neuroscience*, 11(6):713–720, 2008.

[148] J.W. Goodman. *Introduction to Fourier optics*. Roberts & Company Publishers, 2005.

[149] G.C. Spalding, J. Courtial, and R. Di Leonardo. Holographic optical tweezers. *Structured Light and Its Applications: An Introduction to Phase-Structured Beams and Nanoscale Optical Forces*, page 139, 2008.

[150] B.E.A. Saleh. *Fundamentals of Photonics*. 2007.

[151] J. Liesener, M. Reicherter, T. Haist, and HJ Tiziani. Multi-functional optical tweezers using computer-generated holograms. *Optics Communications*, 185(1-3):77–82, 2000.

[152] D.G. Grier and Y. Roichman. Holographic optical trapping. *Applied optics*, 45(5):880–887, 2006.

[153] Andor Technology plc. What is EMCCD?, 2005. `http://www.emccd.com/`.

[154] Tomas Cižmár, V. Kollárová, X. Tsampoula, F. Gunn-Moore, W. Sibbett, Z. Bouchal, and K. Dholakia. Generation of multiple Bessel beams for a biophotonics workstation. *Opt. Express*, 16(18):14024–14035, 2008.

[155] J.Y. Sul, C.K. Wu, F. Zeng, J. Jochems, M.T. Lee, T.K. Kim, T. Peritz, P. Buckley, D.J. Cappelleri, M. Maronski, et al. Transcriptome transfer produces a predictable cellular phenotype. *Proceedings of the National Academy of Sciences*, 106(18):7624, 2009.

[156] M.W. Klymkowsky. Plakophilin, armadillo repeats, and nuclear localization. *Microscopy research and technique*, 45(1):43–54, 1999.

[157] C.L. Celso, H.E. Fleming, J.W. Wu, C.X. Zhao, S. Miake-Lye, J. Fujisaki, D. Côté, D.W. Rowe, C.P. Lin, and D.T. Scadden. Live-animal tracking of individual haematopoietic stem/progenitor cells in their niche. *Nature*, 457(7225):92–96, 2008.

[158] X. Tsampoula. *Femtosecond cellular transfection using novel laser beam geometries*. PhD thesis, 2009.

[159] P. Mthunzi. *Optical sorting and photo-transfection of mammalian cells*. PhD thesis, University of St Andrews, 2010.

[160] DR Meldrum, CH Fisher, MP Moore, M. Saini, MR Holl, WH Pence, SE Moody, DL Cunningham, and PJ Wiktor. Acapella-5k, a high-throughput automated genome and chemical analysis system. 3:2321–2328, 2004.

[161] M. Arrasate and S. Finkbeiner. Automated microscope system for determining factors that predict neuronal fate. *Proceedings of the National Academy of Sciences of the United States of America*, 102(10):3840, 2005.

[162] B. Neumann, M. Held, U. Liebel, H. Erfle, P. Rogers, R. Pepperkok, and J. Ellenberg. High-throughput RNAi screening by time-lapse imaging of live human cells. *Nature methods*, 3(5):385–390, 2006.

[163] W. Supatto, S.E. Fraser, and J. Vermot. An all-optical approach for probing microscopic flows in living embryos. *Biophysical journal*, 95(4):L29–L31, 2008.

[164] G. Thalhammer, R. Steiger, S. Bernet, and M. Ritsch-Marte. Optical macrotweezers: trapping of highly motile micro-organisms. *Journal of Optics*, 13:044024, 2011.

[165] D.J. Stevenson, F. Gunn-Moore, and K. Dholakia. Light forces the pace: optical manipulation for biophotonics. *Journal of Biomedical Optics*, 15:041503, 2010.

[166] D.L. Wokosin, J.M. Squirrell, K.W. Eliceiri, and J.G. White. Optical workstation with concurrent, independent multiphoton imaging and experimental laser microbeam capabilities. *Review of scientific instruments*, 74:193, 2003.

[167] C. Xie, M.A. Dinno, and Y. Li. Near-infrared Raman spectroscopy of single optically trapped biological cells. *Optics letters*, 27(4):249–251, 2002.

[168] J. Guck, R. Ananthakrishnan, H. Mahmood, T.J. Moon, C.C. Cunningham, and J. Kás. The optical stretcher: a novel laser tool to micromanipulate cells. *Biophysical Journal*, 81(2):767–784, 2001.

[169] I.M. Tolić-Nørrelykke, E.L. Munteanu, G. Thon, L. Oddershede, and K. Berg-Sørensen. Anomalous diffusion in living yeast cells. *Physical review letters*, 93(7):78102, 2004.

[170] H. Liang, K.T. Vu, P. Krishnan, T.C. Trang, D. Shin, S. Kimel, and M.W. Berns. Wavelength dependence of cell cloning efficiency after optical trapping. *Biophysical journal*, 70(3):1529–1533, 1996.

[171] Y. Liu, DK Cheng, GJ Sonek, MW Berns, CF Chapman, and BJ Tromberg. Evidence for localized cell heating induced by infrared optical tweezers. *Biophysical journal*, 68(5):2137–2144, 1995.

[172] GM Akselrod, W. Timp, U. Mirsaidov, Q. Zhao, C. Li, R. Timp, K. Timp, P. Matsudaira, and G. Timp. Laser-guided assembly of heterotypic three-dimensional living cell microarrays. *Biophysical journal*, 91(9):3465–3473, 2006.

[173] K.C. Neuman, E.H. Chadd, G.F. Liou, K. Bergman, and S.M. Block. Characterization of photodamage to Escherichia coli in optical traps. *Biophysical journal*, 77(5):2856–2863, 1999.

[174] W. Choi, S.W. Nam, H. Hwang, S. Park, and J.K. Park. Programmable manipulation of motile cells in optoelectronic tweezers using a grayscale image. *Applied Physics Letters*, 93:143901, 2008.

[175] J.K. Valley, P. Swinton, W.J. Boscardin, T.F. Lue, P.F. Rinaudo, M.C. Wu, M.M. Garcia, and M.H. Sham. Preimplantation mouse embryo selection guided by light-induced dielectrophoresis. *PloS one*, 5(4):e10160, 2010.

[176] J. Umanzor-Alvarez, E.C. Wade, A. Gifford, K. Nontapot, A. Cruz-Reese, T. Gotoh, J.C. Sible, and G.A. Khodaparast. Near-infrared laser delivery of nanoparticles to developing embryos: A study of efficacy and viability. *Biotechnology Journal*, 2011.

[177] E. Cotter, R.M. O'Riordan, and A.A. Myers. Recruitment patterns of serpulids (annelida: Polychaeta) in Bantry Bay, Ireland. *Journal of the Marine Biological Association of the UK*, 83(01):41–48, 2003.

[178] DR Dixon, JT Wilson, PL Pascoe, and JM Parry. Anaphase aberrations in the embryos of the marine tubeworm Pomatoceros lamarckii (Polychaeta: Serpulidae): a new in vivo test assay for detecting aneugens and clastogens in the marine environment. *Mutagenesis*, 14(4):375, 1999.

[179] T. Takahashi, C. McDougall, J. Troscianko, W.C. Chen, A. Jayaraman-Nagarajan, S.M. Shimeld, and D.E.K. Ferrier. An EST screen from the annelid Pomatoceros lamarckii reveals patterns of gene loss and gain in animals. *BMC Evolutionary Biology*, 9(1):240, 2009.

[180] C. McDougall, W.C. Chen, S.M. Shimeld, and D.E.K. Ferrier. The development of the larval nervous system, musculature and ciliary bands of Pomatoceros lamarckii (Annelida): heterochrony in polychaetes. *Front Zool*, 3(16):1742–9994, 2006.

[181] DR Dixon, PL Pascoe, and LRJ Dixon. Karyotypic differences between two species of Pomatoceros, P. triqueter and P. lamarckii (Polychaeta: Serpulidae). *Journal of the Marine Biological Association of the UK*, 78(04):1113–1126, 1998.

[182] H. Zibrowius. Étude morphologique, systématique et écologique des Serpulidae (Annelida Polychaeta) de la région de Marseille. *Recueil des travaux de la Station marine dEndoume*, 59(43):83–252, 1968.

[183] JG Thomas. Pomatoceros, sabella and amphitrite (liverpool marine biol. comm. memoir no. 33). In *Proc. Trans. Liverpool Biol. Soc*, volume 43, pages 1–88, 1940.

[184] RH Hedley. Tube formation by Pomatoceros triqueter (Polychaeta). *Journal of the Marine Biological Association of the UK*, 37(02):315–322, 1958.

[185] F. Raible, K. Tessmar-Raible, K. Osoegawa, P. Wincker, C. Jubin, G. Balavoine, D. Ferrier, V. Benes, P. De Jong, J. Weissenbach, et al. Vertebrate-type intron-rich genes in the marine annelid Platynereis dumerilii. *Science*, 310(5752):1325, 2005.

[186] J.H.L. Hui, F. Raible, N. Korchagina, N. Dray, S. Samain, G. Magdelenat, C. Jubin, B. Segurens, G. Balavoine, D. Arendt, et al. Features of the ancestral bilaterian inferred from Platynereis dumerilii ParaHox genes. *BMC biology*, 7(1):43, 2009.

[187] R.C. Brusca, G.J. Brusca, and NJ Haver. *Invertebrates. Sunderland, Massachusetts*. Sinauer Associates, Inc, 2003.

[188] K. Tessmar-Raible and D. Arendt. Emerging systems: between vertebrates and arthropods, the lophotrochozoa. *Current opinion in genetics & development*, 13(4):331–340, 2003.

[189] A. Ashkin. Acceleration and trapping of particles by radiation pressure. *Physical Review Letters*, 24(4):156–159, 1970.

[190] K.C. Neuman and S.M. Block. Optical trapping. *Review of Scientific Instruments*, 75:2787, 2004.

[191] A. Ashkin. Forces of a single-beam gradient laser trap on a dielectric sphere in the ray optics regime. *Biophys. J*, 61(2):569–582, 1992.

[192] P. Prentice, M. MacDonald, T. Frank, A. Cuschier, G. Spalding, W. Sibbett, P. Campbell, and K. Dholakia. Manipulation and filtration of low index particles with holographic laguerre-gaussian optical trap arrays. *Optics Express*, 12(4):593–600, 2004.

[193] KT Gahagan and GA Swartzlander, Jr. Simultaneous trapping of low-index and high-index microparticles observed with an optical-vortex trap. *Journal of the Optical Society of America B*, 16(4):533–537, 1999.

[194] PC Chaumet and M. Nieto-Vesperinas. Time-averaged total force on a dipolar sphere in an electromagnetic field. *Optics Letters*, 25(15):1065–1067, 2000.

[195] M. Dienerowitz. *Plasmonic effects upon optical trapping of metal nanoparticles*. PhD thesis, University of St Andrews, 2010.

[196] S. Chu, JE Bjorkholm, A. Ashkin, and A. Cable. Experimental observation of optically trapped atoms. *Physical Review Letters*, 57(3):314–317, 1986.

[197] A. Ashkin and JM Dziedzic. Optical levitation by radiation pressure. *Applied Physics Letters*, 19(8):283–285, 1971.

[198] A. Ashkin and JM Dziedzic. Stability of optical levitation by radiation pressure. *Applied Physics Letters*, 24(12):586–588, 1974.

[199] PRT Jess, V. Garcés-Chávez, D. Smith, M. Mazilu, L. Paterson, A. Riches, CS Herrington, W. Sibbett, and K. Dholakia. Dual beam fibre trap for raman micro-spectroscopy of single cells. *Opt. Express*, 14(12):5779–5791, 2006.

[200] E. Cotter, RM O'Riordan, and AA Myers. A histological study of reproduction in the serpulids Pomatoceros triqueter and Pomatoceros lamarckii (annelida: Polychaeta). *Marine Biology*, 142(5):905–914, 2003.

[201] M.D. Rand, A.L. Kearney, J. Dao, and T. Clason. Permeabilization of Drosophila embryos for introduction of small molecules. *Insect Biochemistry and Molecular Biology*, 2010.

[202] G.A. Cerda, J.E. Thomas, M.L. Allende, R.O. Karlstrom, and V. Palma. Electroporation of DNA, RNA, and morpholinos into zebrafish embryos. *Methods*, 39(3):207–211, 2006.

[203] I. Gwynn and PCT Jones. On the egg investments and fertilization reaction in Pomatoceros triqueter L. *Cell and Tissue Research*, 113(3):388–395, 1971.

[204] Maria Leilani Torres-Mapa, Maciej Antkowiak, Hana Cizmarova, David E. K. Ferrier, Kishan Dholakia, and Frank J. Gunn-Moore. Integrated holographic system for all-optical manipulation of developing embryos. *Biomed. Opt. Express*, 2(6):1564–1575, Jun 2011.

[205] C.J. de Grauw, J.M. Vroom, H. van der Voort, and H.C. Gerritsen. Imaging properties in two-photon excitation microscopy and effects of refractive-index mismatch in thick specimens. *Applied optics*, 38(28):5995–6003, 1999.

[206] M.K. Kreysing, T. Kießling, A. Fritsch, C. Dietrich, J.R. Guck, and J.A. Kás. The optical cell rotator. *Optics Express*, 16(21):16984–16992, 2008.

[207] M. Abe, M. Shimizu, and R. Kuroda. Expression of exogenous fluorescent proteins in early freshwater pond snail embryos. *Development Genes and Evolution*, 219(3):167–173, 2009.

[208] S. Izumida, K. Onishi, and M. Saito. Estimation of laser-induced breakdown threshold of microparticles in water. *Jpn. J. Appi. Phys. Vol*, 37:2039–2042, 1998.

[209] AG Doukas, AD Zweig, JK Frisoli, R. Birngruber, and TF Deutsch. Non-invasive determination of shock wave pressure generated by optical breakdown. *Applied Physics B: Lasers and Optics*, 53(4):237–245, 1991.

[210] JG Fujimoto, WZ Lin, EP Ippen, CA Puliafito, and RF Steinert. Time-resolved studies of Nd:YAG laser-induced breakdown. plasma formation, acoustic wave generation, and cavitation. *Investigative ophthalmology & visual science*, 26(12):1771, 1985.

[211] Y. Tomita and A. Shima. Mechanisms of impulsive pressure generation and damage pit formation by bubble collapse. *Journal of Fluid Mechanics*, 169:535–564, 1986.

[212] A. Vogel, W. Lauterborn, and R. Timm. Optical and acoustic investigations of the dynamics of laser-produced cavitation bubbles near a solid boundary. *Journal of Fluid Mechanics*, 206:299–338, 1989.

[213] A. Ben-Yakar, D. Eversole, and O. Ekici. Spherical and anisotropic gold nanomaterials in plasmonic laser phototherapy of cancer. 2009.

[214] P. Chakravarty, W. Qian, M.A. El-Sayed, and M.R. Prausnitz. Delivery of molecules into cells using carbon nanoparticles activated by femtosecond laser pulses. *Nature Nanotechnology*, 5(8):607–611, 2010.

[215] Y. Arita, M.L. Torres-Mapa, W.M. Lee, T. Čižmár, P. Campbell, F.J. Gunn-Moore, and K. Dholakia. Spatially optimized gene transfection by laser-induced breakdown of optically trapped nanoparticles. *Applied Physics Letters*, 98:093702, 2011.

[216] N. Nishimura, C.B. Schaffer, B. Friedman, P.S. Tsai, P.D. Lyden, and D. Kleinfeld. Targeted insult to subsurface cortical blood vessels using ultrashort laser pulses: three models of stroke. *Nature Methods*, 3(2):99–108, 2006.

[217] A.N. Hellman, B. Vahidi, H.J. Kim, W. Mismar, O. Steward, N.L. Jeon, and V. Venugopalan. Examination of axonal injury and regeneration in micropatterned neuronal culture using pulsed laser microbeam dissection. *Lab Chip*, 10(16):2083–2092, 2010.

9 Appendix

9.1 Cell culture

Chinese hamster ovary (CHO-K1) cells and Human embryonic kidney cells (HEK293) are cultured in T25 flasks at 37^{o}C and 5% CO_2 in Modified Eagles Medium (Sigma, UK) with 10% Fetal Calf Serum (GlobePharm, University of Surrey, UK), 20 μg/mL streptomycin (Sigma, UK) and 20 μg/mL penicillin (Sigma,UK). Cells were passaged three times a week and number of passages used for experiment was a maximum of 30 for CHO-K1 and 32 for HEK293.

9.2 Willin-GFP expressing stable colony

A stable tetracycline inducible system, TRex willin-GFP-HEK was created using a TRex inducible plasmid pcDNA4/TO/myc-his (Invitrogen, UK) modified to express willin-GFP, which was then transfected into stable HEK293 cells containing a plasmid expressing a tetracycline repressor, pcDNA6/TR. TRex willin-GFP-HEK cells are cultured in T25 flasks in the presence of Dulbeco Modified Eagles Medium (Sigma, UK) with 10% Fetal Calf Serum (GlobePharm, University of Surrey, UK), 2 mM L-glutamate, 100 units/mL penicillin and 100 units/mL streptomycin (Sigma, UK). Stable cells were selected by the addition with 5 μg/mL blasticidin and 250 μg/mL zeocin. Willin-GFP expression was induced with 1 μg/mL

tetracycline (Invitrogen, UK). Cells were routinely passaged three times a week.

9.3 siRNA chemical transfection

Willin knockdown was performed using siRNA, to a final concentration of 5nM, specifically targeting the protein (GACAGAGCAGCAAGAUACUAUUAUU, CACAGACUAUAUGUCGGAAACCAAA, GCCUCUAUAUGAAUCUGCAGCCUGU; Invitrogen) using Gene Eraser (Startagene); according to manufacture's instructions. Protein expression was analysed by Western blotting, using anti-GFP (Santa-Cruz) and anti-actin (Sigma) as a loading control. Fig. 9.1 shows the Western blot analysis of the chemically transfected cells with siRNA specific for willin.

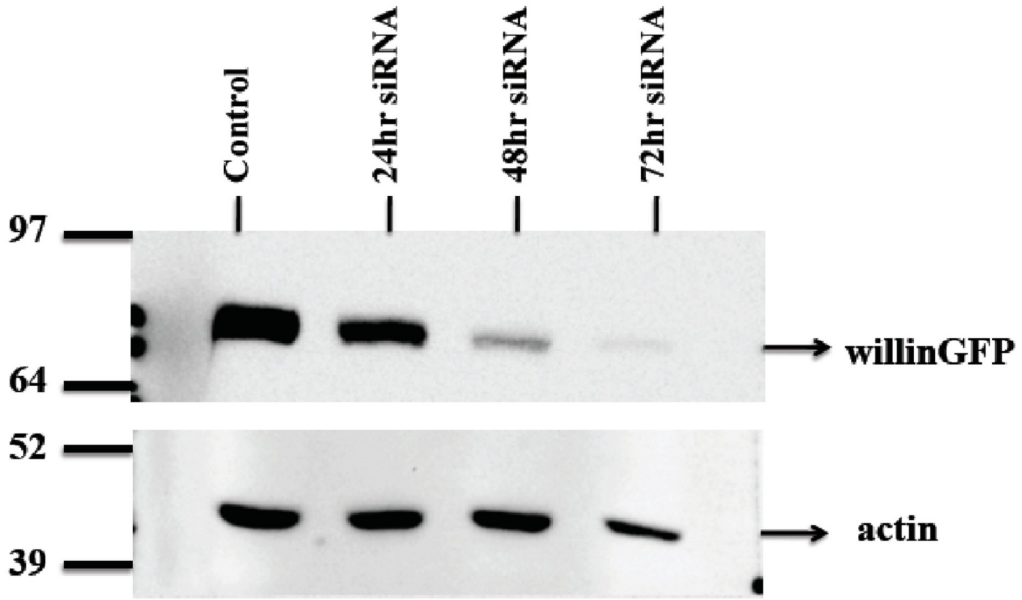

Figure 9.1: Western blot analysis depicting reduction of willin-GFP expression, 48 h after chemical transfection of 5 nm siRNA into TRex-willin-GFP cells. TRex-willin-GFP cells were induced with 1 μg/mL tetracycline to express willin-GFP 24 h prior to siRNA treatment. Western blots were probed with anti-GFP and anti-actin, with the latter used as a loading control [130].

9.4 Human willin sequence

9.4.1 DNA sequence

atgaacaaattgaattttcataacaacagagtcatgcaagaccgccgcagtgtgtgcattttccttcccaacgatgaatctctgaac
atcatcataaatgttaagattctgtgtcaccagttgctggtccaggtttgtgacctgctcaggctaaaggactgccacctctttggact
cagtgttatacaaaataatgaacatgtgtatatggagttgtcacaaaagctttacaaatattgtccaaaagaatggaagaaagaggc
cagcaagggtatcgaccaatttgggcctcctatgatcatccacttccgtgtgcagtactatgtggaaaatggcagattgatcagtg
acagagcagcaagatactattattactggcacctgagaaaacaagttcttcattctcagtgtgtgctccgagaggaggcctacttc
ctgctggcagcctttgccctgcaggctgatcttgggaacttcaaaaggaataagcactatggaaaatacttcgagccagaggctt
acttcccatcttgggttgtttccaagaggggaaggactacatcctgaagcacattccaaacatgcacaaagatcagtttgcacta
acagcttccgaagctcatcttaaatatatcaaagaggctgtccgactggatgacgtcgctgttcattactacagattgtataaggata
aaagggaaattgaagcatcgctgactcttggattgaccatgaggggaatacagatttttcagaatttagatgaagagaaacaatta
ctttatgatttcccctggacaaatgttggaaaattggtgtttgtgggtaagaaatttgagattttgccagatggcttgccttctgcccgg
aagctcatatactacacggggtgccccatgcgctccagacacctcctgcaacttctgagcaacagccaccgcctctatatgaatc
tgcagcctgtcctgcgccatatccggaagctggaggaaaacgaagagaagaagaagcagtaccgggaatcttacatcagtgacaac
ctggacctcgacatggaccagctggaaaaacggtcgcgggccagcgggagcagtgcgggcagcatgaaacacaagcgcct
gtcccgtcattccaccgccagccacagcagttcccacacctcgggcattgaggcagacaccaagccccgggacacggggcc
agaagacagctactccagcagtgccatccaccgcaagctgaaaacctgcagctcaatgaccagtcatggcagctcccacacct
caggggtggagagtggcggcaaagaccggctggaagaggacttacaggacgatgaaatagagatgttggttgatgaccccc
gggatctggagcagatgaatgaagagtctctggaagtcagcccagacatgtgcatctacatcacagaggacatgctcatgtcgc
ggaagctgaatggacactctgggttgattgtgaaagaaattgggtcttccacctcgagctcttcagaaacagttgttaagcttcgtg
gccagagtactgattctcttccacagactatatgtcggaaaccaaagacctccactgatcgacacagcttgagcctcgatgacatc
agactttaccagaaagacttcctgcgcattgcaggtctgtgtcaggacactgctcagagttacacctttggatgtggccatgaact
ggatgaggaaggcctctattgcaacagttgcttggcccagcagtgcatcaacatccaagatgcttttccagtcaaaagaaccagc
aaatacttttctctggatctcactcatgatgaagttccagagtttgttgtgtaa

9.4.2 Amino acid sequence

MNKLNFHNNRVMQDRRSVCIFLPNDESLNIIINVKILCHQLLVQVCDLLRLKDCH
LFGLSVIQNNEHVYMELSQKLYKYCPKEWKKEASKGIDQFGPPMIIHFRVQYYV
ENGRLISDRAARYYYYWHLRKQVLHSQCVLREEAYFLLAAFALQADLGNFKRN
KHYGKYFEPEAYFPSWVVSKRGKDYILKHIPNMHKDQFALTASEAHLKYIKEAV
RLDDVAVHYYRLYKDKREIEASLTLGLTMRGIQIFQNLDEEKQLLYDFPWTNVG
KLVFVGKKFEILPDGLPSARKLIYYTGCPMRSRHLLQLLSNSHRLYMNLQPVLRH
IRKLEENEEKKQYRESYISDNLDLDMDQLEKRSRASGSSAGSMKHKRLSRHSTAS
HSSSHTSGIEADTKPRDTGPEDSYSSSAIHRKLKTCSSMTSHGSSHTSGVESGGKD
RLEEDLQDDEIEMLVDDPRDLEQMNEESLEVSPDMCIYITEDMLMSRKLNGHSG
LIVKEIGSSTSSSSETVVKLRGQSTDSLPQTICRKPKTSTDRHSLSLDDIRLYQKDF
LRIAGLCQDTAQSYTFGCGHELDEEGLYCNSCLAQQCINIQDAFPVKRTSKYFSL
DLTHDEVPEFVVstop

List of publications

Peer-reviewed publications

- Transient transfection of mammalian cells using a violet diode laser, M.L. Torres-Mapa, L. Angus, M. Ploschner, K. Dholakia, F. Gunn-Moore. J. Biomed. Opt. 15(2), (2010).
- Application of dynamic diffractive optics for enhanced femtosecond based cell transfection, M.Antkowiak, M.L. Torres-Mapa, F. Gunn-Moore, K. Dholakia. J. Biophotonics, Vol. 3, (2010).
- Quantitative phase study of the dynamic cellular response in femtosecond laser photoporation, M. Antkowiak, M.L. Torres-Mapa, K. Dholakia, and F. Gunn-Moore. Biomed. Opt. Express, Vol. 1, Issue 2, pp. 414-424 (2010).
- Spatially optimized gene transfection by laser induced breakdown of optically trapped nanoparticles, Y. Arita, M.L. Torres-Mapa, W. Lee, T. Cizmar, F. Gunn-Moore and K. Dholakia. App. Phys. letters, 98, (2011).
- Integrated holographic system for all-optical manipulation of developing embryos, M.L. Torres-Mapa, M. Antkowiak, H. Cizmarova, D.Ferrier, K. Dholakia and F. Gunn-Moore. Biomed. Opt. Express, 2(6),pp. 1564–1575, (2011).

Conference and seminar contributions

Talks

- Femtosecond beam multiplexing system for enhanced optoinjection and phototransfection of mammalian cells, Optics Within Life Sciences, (Canada), 2010.
- Violet diode laser induced DNA phototransfection and gene knockdown in mammalian cells, Royal Society Meeting, (United Kingdom), 2010. invited

- Transient transfection of mammalian cells using a violet diode laser, Photonics 4 Life Scientific Meeting, (Spain), 2009.
- Transient transfection of mammalian cells using a violet diode laser,CLEO -Europe, (Germany), 2009.
- Transient transfection of mammalian cells using a violet diode laser,Institute of Physics, Annual meeting of Physics in Biology, (United Kingdom), 2008.

Posters

- Transient transfection of mammalian cells using a violet diode laser, International Biophotonics Summer School, (Sweden), 2009.

Acknowledgements

I would like to thank my supervisors, Prof. Kishan Dholakia and Prof. Frank Gunn-Moore for their guidance, encouragements and patience throughout my PhD. It has been a privilege working with the best in the field and I have learned so much while working with them. Kishan and Frank, your enthusiasm and your vision pushed me through the months when experiments won't work and things are not going according to plan.

Inside the laboratory, I am grateful for two mentors whom I worked quite closely for the past three years. Dr. David Stevenson has expanded my understanding of biology and biological protocols. I'm indebted to Dr. Maciej Antkowiak whom I worked closely during the SLM project, for his patience and understanding and for mentoring me about science and research. Thank you both for your wisdom and friendship.

My PhD thesis is interdisciplinary in nature and I would like to thank my collaborators, Dr. Liselotte Angus, whom I worked with the gene knockdown experiments. To Martin Ploschner, for working with me on the temperature calculations on the violet diode work. Thank you to Dr. David EK. Ferrier, who patiently discussed things with me through the Pomatoceros project. I would also like to thank Dr. Yoshihiko Arita, Dr. Steve Lee and Dr. Tomas Cizmar for working with me during the LIB experiments. I would like to thank Brian Powell for providing the countless DNA for the transfection experiments. As well as to, Dr. Hana Cizmarova for always helping out with the Pomatoceros project.

I would like to thank my friends who have kept me sane throughout the last three years. To Jacq and Rumelo Amor, for their friendship and encouragement through the tough times. To Maria and Frank Dienerowitz for all their advices and friendship. To AnnaChiara De Luca for always encouraging and believing in me. To Kirsty Muirhead for the lovely cakes and friendship when I most needed it. I am thankful to Heather Dalgarno for her help during my viva preparations. Thanks to Andrew Rudhall for all the critical discussions about life, science and anything in general. To Fiona Bain, Jorg Baumgartl, Lara Torralbo-Campo, Areti Mourka, Sebastian Kosmeir, Jill Morris, Xanthi Tsampoula, Rob Marchington, Bavishna Balagobal, Praveen Ashok, Janelle Shane for all the friendly advices, lunch, chats, coffee, parties, dinners and trips.

I am very grateful to the Hayhow family; Ate Jane, Simon and Matt for adopting me during my stay here in Scotland.

This thesis is dedicated to my family in the Philippines; Mama, Ate Cecille, Paolo and Johsua who have supported me and prayed for me through my journey.

And finally, I am thankful to my husband, Louise Mapa for his understanding

and ready hot meals during my late nights and thesis writing.

My PhD was funded by Scottish University Physics Alliance (SUPA) as a prize studentship.

- Maria Leilani Torres-Mapa